Vrije Universiteit Brussel
Interuniversity Institute for High Energies

Artificial neural network based position estimation in positron emission tomography

Author

Mateusz Wędrowski

Promotors
Prof. Peter Bruyndonckx
Prof. Stefaan Tavernier

16 December 2010

Doctoral examination commission:
Prof. Michel Defrise (AZ ULB) - chairman
Prof. Peter Bruyndonckx (ELEM VUB)
Dr Denis Schaart (TU Delft)
Prof. Stefaan Tavernier (ELEM VUB)
Prof. Gerd Vandersteen (ELEC VUB)
Prof. Karl Ziemons (FZ Jüelich/FH Aachen)

The right understanding of any matter
and a misunderstanding of the same matter
do not wholly exclude each other

Franz Kafka
The trial, 1920.

Contents

Summary

Gamma detection in nearly all commercial positron emission tomography (PET) scanners is based on the use of block detectors with a large number of small scintillator pixels. One of the important factors limiting the spatial resolution in PET scanners using this approach is the uncertainty of the exact depth of interaction of the gamma ray in the crystal. Using one large and undivided piece of scintillator where the position of the gamma interaction is extracted from the light distribution in the block, allows overcoming this limitation. At the same time, the sensitivity of the scanner can be increased by avoiding inter-crystal dead spaces. However this approach tends to produce poor results if simple minded methods, such as centre of gravity, are used to determine the position of the gamma interaction in the crystal block. On the other hand, if machine learning algorithms such as artificial neural networks are used, excellent performance is obtained. With the dramatic increase of computing power in recent years, this is now a realistic approach to real-time gamma detection in PET scanners.

Usage of avalanche photo diodes (APD) is an alternative to photomultiplier tubes (PMT). Generally a PMT is cheaper and has a higher output signal, so that in standard PET applications PMTs are still more common. Nevertheless, a PET scanner by itself, as a separate device, is getting less and less competitive with respect to integrated multi-modality solutions. In the case of PET coupled to magnetic resonance imaging (MRI) the detectors are exposed to intense magnetic fields. This excludes the usage of PMT and makes APD competitive. The recently developed silicon photo-multiplier (SiPM) detectors seem to have even more potential.

The goal of this thesis is to investigate the intrinsic detector spatial resolution behaviour of $20 \times 20 \times 10 \, \text{mm}^3$ monolithic Lutetium Orthosilicate (LSO) scintillator block PET detector based on Hamamatsu S8550 APD light sensor with the artificial neural network (ANN) applied as the estimating algorithm. The conditions of measurements and analysis are based on realistic scanner operation. The robustness of the neural network is studied on several parameters as the incidence beam angle, random fraction in data, APD high voltage and temperature fluctuations. Finally a comparison with alternative light sensors for a monolithic block detector design is done. The data from 64-multichannel PMT and 16-channel SiPM based detectors are studied individually to apply the same resolution reconstruction conditions.

The research is done in the framework of the Crystal Clear Collaboration in cooperation between CIEMAT Madrid/Spain, Forschungszentrum Jülich/Germany and Vrije Universiteit Brussels. The data from alternative detector designs are analysed by courtesy of the group from the University of Technology Delft and from The University of Science and Technology of China (UTSC).

In chapter 1 the basic physics processes and the main PET characteristics are explained. First the concept of tracers is explained. Then the PET principles as annihilation detection with other effects are described. In the later part of the chapter, the most important PET factors are looked into i.e. spatial resolution, sensitivity, noise and energy resolution.

In the first part of chapter 2 the scintillator material is described, its characteristic, mechanism of operation and most common types. The second part is devoted to a discussion of light sensors such as PMT and photo diodes. The biggest emphasis is put on APD detector, its principles and main parameters. Promising SiPM detector is described.

Chapter 3 is the introduction to the presentation of the result. The advantages of the monolithic scintillator blocks based on APD design and the details of the aim of the project are explained. The detector set-up structure and signal processing idea are described and the artificial neural network algorithm is referred to.

Chapter 4 summarises the investigation done for APD based detectors. The first part describes the data structure and data acquiring process. All calibrations and preparation for measurement are specified. Then the ANN structures applied for the spatial resolution estimation are explained. The last part shows the result of the ANN robustness studies.

The comparison between data obtained with different detectors is presented in chapter 5. In this chapter, the first three sections present an analysis of the data obtained with obtained with with two detectors using of PMT and one detector using of SiPM. The last section presents conclusion from a comparison between these detectors.

Introduction

Positron Emission Tomography (PET) is a nuclear imagining technique, used in clinical medicine and in research, that can measure metabolic and biochemical processes in a living organism non-invasively. Images are reconstructed from the spatial distribution of a short lifetime positron-emitting nuclei that are introduced in the body with tracer molecules. Radioactive compounds are accumulated in certain organs (depending on the kind of compound). At the same point the isotope emits a positron. Then a positron looses its energy for interactions with electrons from a tissue. Finally, when the positron has lost its kinetic energy and annihilates with an electron, it produces two 511 keV collinear photons. Annihilation photons are detected in coincidence. Thus the position of the annihilation point is estimated between the coincidence detectors. The tissues with an accumulated tracers are localised by collecting the coincidence information around the imaged object. The accuracy of positioning the radioactive molecule is described by spatial resolution.

PET is applied in cardiac surgery, cancer diagnosis and management, neurology and psychiatry. PET is used very common in oncology because it discovers tumor changes earlier then any other methods. As opposed to other diagnostic methods, PET does not provide structural information about the object. Therefore it requires external markers or other supporting technique. A common solution is the multi-modality approach. Well know is the PET/CT dual-modality.

Computed Tomography (CT) is based on the attenuation of the X-ray beam in a target. The CT uses composition of 2D X-ray images to construct volumetric 3D images. This method offers one of the highest spatial resolution limited mainly by a radioactive dose. Therefore movement of a body, like heart beats, breathing need to be taken under consideration during image reconstruction. CT works very well for the distinction bones and soft tissues, but has more problems with soft tissues placed close to each other. Also the informations hidden after solid tissues as bones is hardly recognised. A combination of PET/CT puts advantages of both methods in one device.

Another imaging method, the Single Photon Emission Computed Tomography (SPECT) is somewhat similar to PET. It also employs tracers as the radiation source. However, instead of measuring coincidences, this technique is based on single photon detection. Therefore it requires additively a collimator. That is not a trivial problem from sensitivity point of view. Nevertheless, the tracers of SPECT are not limited to positron emitters. Thus they are easier and cheaper to produce. As well there exist more tracers for SPECT. The single photon method can follow two different energies tracers simultaneously. On the other hand, it doubles the dose of the radioactivity into the body. PET tracers employ molecules that are originally present in the body and no problem with uptake appears. Whereas there is some risk that the SPECT tracer will not be accumulated uniformly, or

just rejected since here the compounds are rather strange for a living organism.

Another well known imaging technique is Magnetic Resonance Imaging (MRI). This technique uses magnetic fields to force nuclei. These nuclei are radio pulse excited, to emit similar frequencies waves, that are registered. Because no radioactive tracer is needed, MRI is less harmful than PET or SPECT. It gives structural information such as e.g. CT, without problems with soft tissues distinction. Moreover, fast functional changes can be observed because of fast imaging process. Although PET has the ability of functional imaging, it is to slow to register rapid functional changes. In addition, MRI provides a higher resolution than PET. The biggest disadvantage of MRI is the price of the modality and no "off" option for the magnets.

Apparently PET/MRI multi-modality seems to be the most universal approach. From the other side, it is also the most challenging and expensive. One of the most important problem is to find a compatible high resolution PET detector that is not sensitive for magnetic fields. A MRI compatible brain PET dedicated scanner is under development in CIEMAT. The BrainPET project is a joined effort of the CIEMAT (Madrid/Spain), Forschungzentrum Jülich Germany and the VUB team.

Also different PET designs have been or are being developed in both the academic community and nuclear medicine industry. The goal is to maximize the detection efficiency for annihilation photons and, at the same time, to push the spatial resolution towards the physical limits inherent to the annihilation process. PET imaging has been in use for several decades for human brain and whole body imaging, first only as a research tool. The demand for functional, metabolic, and molecular imaging of the brain has stimulated the development of dedicated high-resolution PET systems.

1

Physics basis and main features

To understand the design of PET scanners it is necessary to explain the basic physics processes and the main PET parameters. The tracers are briefly referred. The principle of PET, annihilation detection and other related effects are described. In the second part of this chapter the most important characteristics of a PET scanners are discussed. These are spatial resolution, sensitivity, noise and energy resolution.

1.1 The tracer

The success of PET depends on positron-emitting imaging agents that have the appropriate pharmacokinetic properties to enable characterization of specific biological processes. This agent is called *a tracer* or *radiopharmaceutical*. It is defined as a biochemical compound containing molecules that are labelled with radionuclides. The molecules used in tracers can be naturally occurring substances, analogues of natural substances or compounds that interact with specific physiologic or biochemical processes in the body. General requirements for an good tracer include the following [Cherry2003]:

– The behaviour of the tracer should be identical or related in a known and predictable manner to that of the natural substance.

– The amount of the tracer should not alter the underlying physiologic process being studied or should be small compared to the amount of endogenous compound being traced.

– The specific activity of the tracer should be sufficiently high to permit imaging without violating the first two requirements.

– Any isotope effect should be negligible or at least quantitatively predictable.

A more detailed list of PET radio-pharmaceuticals demands is described in publication of [Hutchins2008]. One of essential points that makes the PET a unique tool is that the good sensitivity is already obtained with a small radioactive dose. The low tracer concentration causes no pharmacological effect in the body thus are also perfect for preclinical studies. The complexity of the research required to identify candidate compounds, to develop synthetic labelling methods, and demonstrate that the candidate for imaging agent meets all specific radiopharmaceutical criteria, is a major impediment to the rapid implementation of PET methods for the study of specific biological processes. For medical applications of PET, the most important radionuclides are ^{15}O, ^{13}N, ^{11}C and ^{18}F (Table 1.1). For clinical applications, ^{18}F is currently of foremost importance in oncology, due to the most common use of ^{18}F-2-fluoro-2-deoxy-D-glucose (FDG). Imaging with FDG is based on the glucose accumulation in the body, especially in tumour tissues. However, many diseases can give rise to changes in glucose metabolism. This can be measured with help of FDG. Recent developments in tracers area can be found in [Wester2007, Lucignani2007].

Table 1.1: *Most commonly used positron emitting radioisotopes [Humm2003].*

Radionuclide	half-life	E_{max}	E_{average}
^{11}C	20.4 min	0.960 MeV	0.385 MeV
^{13}N	10.0 min	1.198 MeV	0.491 MeV
^{15}O	2.0 min	1.732 MeV	0.735 MeV
^{18}F	109.8 min	0.633 MeV	0.242 MeV

1.2 The positron emission and the annihilation

The aim of a PET scanner is to extract information about the location of radiopharmaceutical inside the body. This process consists of several complex stages. The first step occurs inside a patient. In the most common way, when the tracer is injected into the body, it accumulates in certain tissues. The excess of protons from a tracer radionuclide achieves stability either by electron capture *β^+ decay* or by emission of a positron (fundamental importance for PET technique). The underlying transformation is called β^+ *decay*:

$$p \xrightarrow{\beta^+} n + e^+ + \nu_e \ (+ \text{ Energy}) \tag{1.1}$$
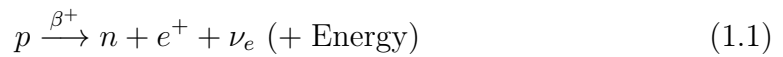
The proton p in the nucleus is transformed into a positive electron e^+ and a neutron n. The positron and the electron neutrino ν_e are ejected from the nucleus. The positron slows down by losing its energy in interactions with atoms. That creates excitations and ionizations in the medium. When most of positron energy is dissipated, the positron comes to rest and combines with an electron, momentarily forming a very short living "exotic atom" named *positronium* [Harpen2004]. After around 10^{-10} s, the positive and negative electrons combine together in a process of *annihilation* *annihilation*, in which their masses are converted into energy. The released energy E can be computed from the Einstein's equation

$$E = mc^2 = m_{e^-}c^2 + m_{e^+}c^2 = 1.022 \,\text{MeV} \tag{1.2}$$
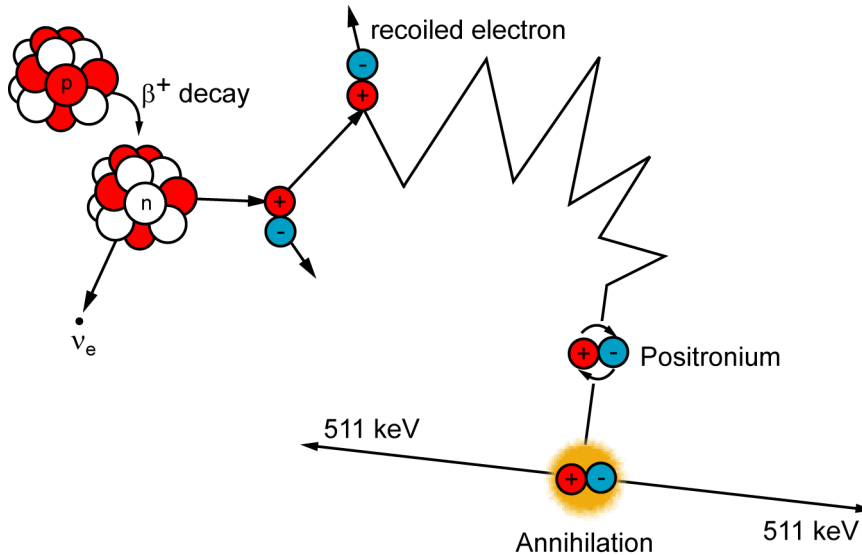
Figure 1.1: *Positron decay and annihilation scheme.*

where m_{e^-} is the electron mass, m_{e^+} the mass of the positron and c is the speed of light. This energy is emitted in the form of two 511 keV photons that are simultaneously sent in opposite, *back-to-back*, directions due to conservation of the energy and momentum law (Fig. 1.1). The annihilation process has several very important properties for the PET concept. First, the annihilation photons are very energetic. It means, its probability for escaping from the body for an external detection is significant. Second, the geometrical line joining two coincidence *LOR* detectors (called *Line of Response* - LOR), that register both 511 keV photons, passes almost exactly through the annihilation point (in reality it is rather a tube, because the detector is finite in size). Because it is close to the positron emitting nuclide, it tags the radiopharmaceutical molecule position in the body. This coincidence technique, referred to as "electronic collimation", eliminates the need for any physical collimation as in SPECT. The typical PET scanners are designed to register LORs around the imaged object or patient and then analyse them in order to find the radiation source. There are two main approaches for annihilation point estimation.

1.3 Annihilation point estimation

The aim of a PET detector is the most accurate estimation of annihilation points in the body that indicate the distribution of positron emitter. As described above, that information is coded in LORs. There are two concepts to determine the actual position of the radioactive atoms. The first is theoretically more straight- *time information* forward and considers the difference in arrival time t between two annihilation photons at the detectors $t = t_{\text{det1}} - t_{\text{det2}}$. This is called *time of flight* (TOF). In this approach each detected photon is tagged with a detector position and detection time. If t is smaller then a set coincidence time window (typically up to 10 ns), the two events are considered physically correlated to the same annihilation. The detected t is directly related to the actual photon time-of-flight difference. Thus

Figure 1.2: *TOF reconstruction. left) with conventional reconstruction, all pixels along the chord are incremented by the same amount; right) with TOF reconstruction, e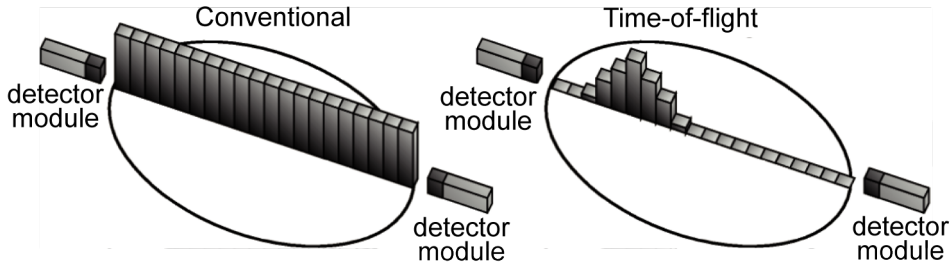ach pixel on the chord is incremented by the probability (as determined by the TOF measurement) that the source is located at that pixel [Moses2003].*

TOF method uses time-of-flight information to estimate the annihilation point on the LOR. The location of the annihilation event x, with respect to the midpoint between the coincidence detectors, is given by $x = t \cdot c/2$, where c is the speed of light. It is blurred by a measurement uncertainty of t called *time resolution* Δt

$$\Delta x = \frac{\Delta t \cdot c}{2} \tag{1.3}$$

If this time difference could be measured with sufficient accuracy, the position of the positron would be constrained to a point rather than a line. So 3D images could be obtained without a reconstruction algorithm. However, to get subcentimeter position resolution, timing resolution of less than 50 ps is necessary, which is impossible to obtain with today's technology.

non-TOF   Because of this, nearly all PET scanners in use today do not apply the time information in order to determine the position of the annihilation along the LORs. Cross-sectional images that reflect the concentration of the positron-emitting radionuclide in the body are acquired by measuring the total radioactivity along the LOR that pass at many different angles through the object. Conventional non-TOF PET reconstruction uses the time information only to identify the coincidences. It is unable to determine which voxel along the line is the source of the two photons. Therefore all the voxels along the line are given the same probability of emission (Fig. 1.2, 1.4). Analytical or iterative reconstruction algorithms are used to estimate the activity distribution most consistent with the measured projection data. The analytical, filtered back projection method is faster and doesn't require a large computing power. On the other hand the reconstructed images have a lower quality, because the compromise between amount of noise and image contrast must be set. There are several iterative algorithms, the most commonly used is maximum likelihood expectation maximization (MLEM). Due to huge number of iteration they require a strong computing unit. Reconstruction with iterative algorithm significantly improve image quality in comparison with analytical. Due to increasing computing power available on the market, iterative algorithms are more commonly used nowadays.

sinogram   The raw data generated in PET scanner are stored in specific 2-D arrays $f(s, \phi)$ called *sinograms*. Each row represents parallel line integrals or *a projection* p(s, ϕ) of the activity at a particular angle ϕ (Fig. 1.3b). The parallel projection can be one or two dimensional. A one dimensional parallel projection of the tracer distributions is obtained by grouping all the LORs at a given angle and sorting them as
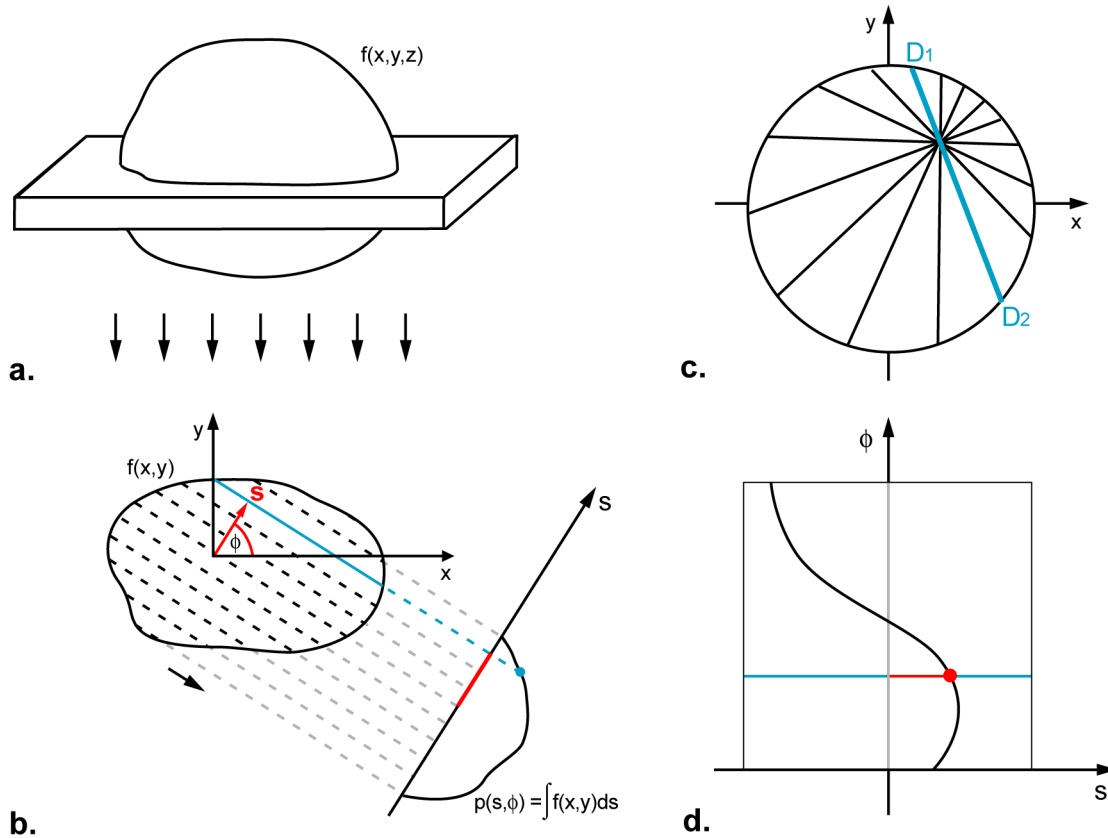
Figure 1.3: *Data representation in sinogram form a.) imaged object described by f(x,y,z), b.) 2D object projection f(x,y) transformed to p(s,ϕ), c.) single point indicated by eight LORs, d.) sinogram of a single point source.*

a function of their distances from the centre of the ring. To project 3D volume, one more dimensions is applied to obtain 2D parallel projection. The number of projections affect the faithfulness of the constructed image. Advanced description of image reconstruction algorithms can be found in [Defrise2008, Reader2007, Qi2006]. Improving image reconstruction algorithms is still an active research field in nuclear medicine modalities.

The TOF method is not forgot as many PET researcher thought several years ago. Some people claim that TOF is in rebirth. Although the idea of using TOF *TOF* was originally proposed in the 1960s, it was not popular until the early 1980s, when the first generation TOF PET systems were built using either CsF or BaF_2 scintillators. The first generations TOF PET best time resolutions are reported as 156 ps and 212 ps for 511 keV, for CsF and BaF_2 respectively. But on the system level the time resolutions between 470 and 750 ps were reached. However specific scintillators required in first TOF PET have pour characteristics, as for instance photofraction, light yield (see §.2.1). It results in poor spatial resolution and sensitivity, that are the most important PET parameters. The discovery of new, fast scintillators, with better overall characteristics, such as LSO and $LaBr_3$ opened the way to a modern TOF PET phase. Nowadays typical time resolution $\sim 400 - 500$ ps can be achieved and there are evidences that it can be brought down to ~ 300 ps [Schaart2010, Muehllehner2006]. Also technology progress allows to use faster and more stable electronics for TOF technique, thus making the method
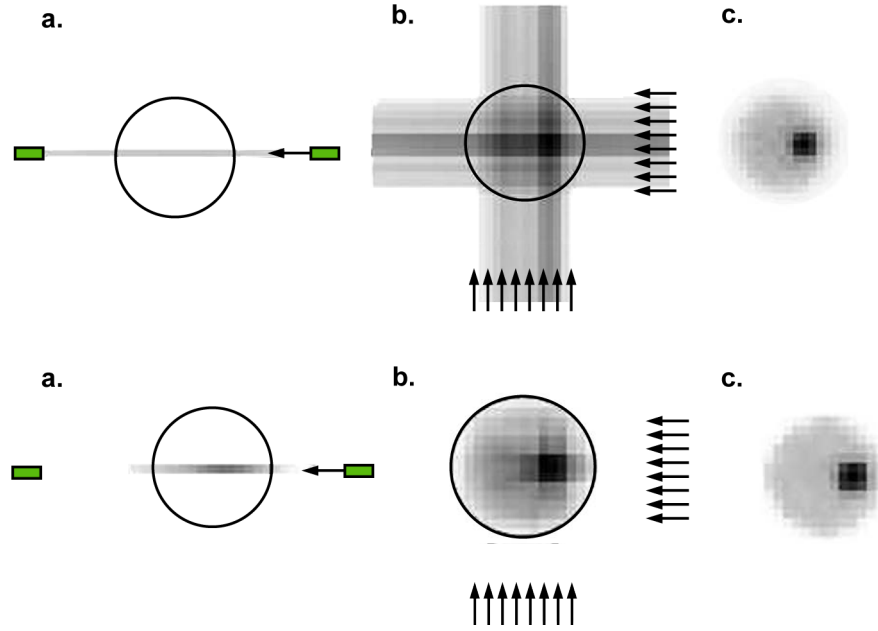
Figure 1.4: *TOF image reconstruction. Top row: a.) one event detected by the central detectors at a 90° angle is evenly back projected into all pixels crossed by the LOR, b.) all events detected at 0° and 90° are back projected, c.) The image obtained at the end of the first MLEM iteration, using all projection data; Bottom row: a.) one event detected by the central detectors at a 90° angle is back projected along the LOR according to a probability distribution with a width proportional to the time resolution, b.) all events detected at 0° and 90° are back projected, c.) the image obtained at the end of the first iteration of MLEM is shown [Conti2009].*

more significant.

The biggest advantage of TOF PET is better signal to noise ratio (SNR) (see §.1.4.2) in comparison with non-TOF method as on Fig. 1.4 [Conti2009, Strother1990]

$$\mathrm{SNR_{TOF}} = \sqrt{\frac{D}{\Delta x}} \cdot \mathrm{SNR_{non-TOF}}. \qquad (1.4)$$

where parameter D is the object diameter. Eq. 1.4 shows that TOF improves noise especially in case of larger diameters, so for heavy patient [Karp2008]. When looking to the clinical needs instead of physical scanner parameters, then the image quality of heavy patients and the total scanning time stand out as one of major challenges. While TOF scanners are just entering clinical use, it will be probably several years until they are widely available. It can be assumed that over the next few years the timing resolution will continue to improve and will lead to better image quality for heavy patients and shorter imaging times as well. On the other hand, while it is relatively easy to quantitatively measure the improvement in SNR in a simple phantom, it is much more difficult to quantitatively predict how the noise reduction affects diagnostic accuracy. It is especially difficult as the noise reduction will depend on the activity distribution in the patient, and so has considerable variation [Moses2007, Muehllehner2006].

1.4 Fundamental image quality factors and limitations

The scanner design details can be easier understood if they are linked to the most important PET scanner factors. Careful studies of PET parameters allow to increase the faithfulness with which an image represents the imaged object. The image quality is affected by several factors such as spatial resolution, sensitivity and energy resolution. These factors are related and improvement of one parameter is often only possible at the cost of degrading the others.

1.4.1 Spatial resolution

Generally, the spatial resolution refers to the sharpness or detail of the image. Its fundamental limits are determined by basic physics. The first effect, determined by the principles of positron decay, is caused by the fact that the positron travels some distance before annihilating with an electron. Then the location of the radionuclide doesn't exactly indicate the annihilation point, that is estimated by the LOR in PET. The LOR is slightly mispositioned and it leads to degradation of the spatial resolution (Fig. 1.5). The distance between the positron emission site and the annihilation point is called *positron range*. The real path travelled by a positron is in most of the cases tortuous with multiple deflections, that makes it longer then the positron range. Radionuclides are characterized by a maximum range for a positron travelling on a strait line without disruption. The positron range depends on the electron density in the medium and the positron energy [Levin1999, Derenzo1979]. Therefore, usually the positron range is expressed by the maximum energy that positron can receive in a positron decay. In denser tissues the positron loses energy faster, then in less dense. These positrons are emitted with a spectrum of energies, which ranges from $0.5\,\mathrm{keV} - 5\,\mathrm{MeV}$ [Cherry2003] depending on the radionuclide type. Only a small fraction of positrons have the full amount of energy available from a decay. The positron path is longer for higher energies. However the LOR misposition is determined by the *effective positron range*, that is given by the perpendicular distance from an annihilation photon trace to the positron emission site (Fig. 1.5). Only exceptionally the positron range is the same as effective positron range. The resulting image blurring fluctuates from
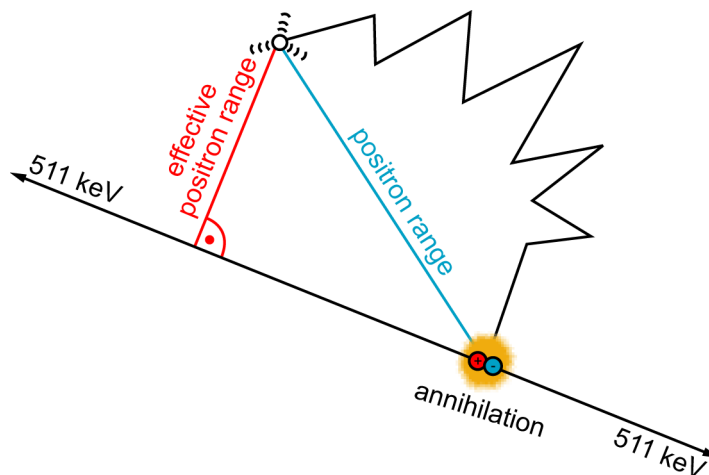
positron range

Figure 1.5: *Positron range effect.*
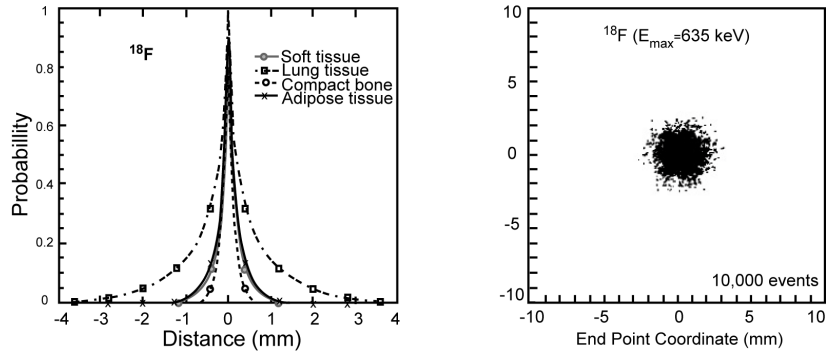
Figure 1.6: *Positron range distribution for ^{18}F [Levin1999].*

tenths of *mm* up to several *mm*. The shape of the positron range distribution is rather exponential instead of Gaussian (Fig. 1.6). There are possibilities to reduce the positron range, by using a strong magnetic field. That could be realised in the framework of PET/MRI dual-modality system. Anyway the method is not yet commonly used because of complexity difficulties. Nevertheless the positron range is not the major problem in PET spatial resolution. Its blurring influence is constant and depends on the radionuclide and the tissue type travelled.

non-colinearity   The second spatial resolution damaging effect is also implicated by the details of positron physics. According to the momentum conservation law, exact back-to-back photon emission occurs only when the positron and the electron are both in rest. That situation almost never happens and usually two photons are emitted with a small deviation from 180° angle. The distribution of emitted angles is rather Gaussian, with a 0.5° FWHM. It leads to the annihilation point shift out from the LOR (Fig. 1.7). This effect is called *non-colinearity*. The non-colinearity error Δ_{nonc} is also described by FWHM of Gaussian function, since it is caused by non-colinearity angle fluctuations. The Δ_{nonc} depends on the detector ring diameter D

$$\Delta_{\mathrm{nonc}} \approx 0.0022 \cdot D \tag{1.5}$$

The effect is more important in clinical tomographs, where ring diameters are bigger. Although the non-colinearity can affect spatial resolution more then positron range, it is still not the main damaging factor.

intrinsic detector spatial resolution   The most important source of spatial resolutions degradation is given by the
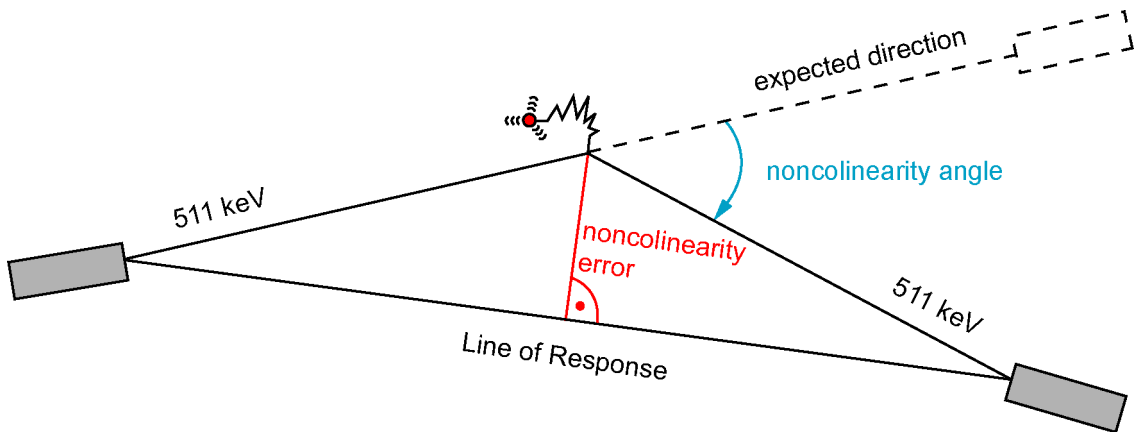
Figure 1.7: *The scheme of non-colinearity effect.*
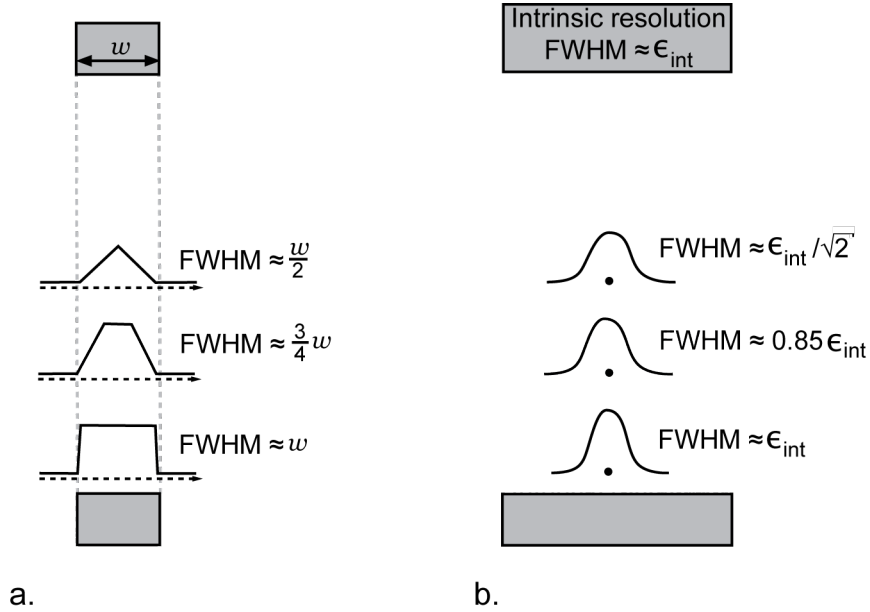
Figure 1.8: *Intrinsic spatial resolution for coincidence detection for: a.) discrete detectors, b.) continous detectors [Cherry2003].*

detector effects. Several effects contribute to this and collectively it is referred to as *the intrinsic detector spatial resolution*. It is usually determined by the detector size and by the parallax effect. For a pixelated design the intrinsic detector resolution can be described by the FWHM of *a coincidence response function* (CRF). The CRF is obtained by measuring coincidence count rates for a small source moving across two detectors. For different source positions between the detectors, the shape of the CRF changes from a triangular in the mid-point, to a trapezoidal or eventually square close to the detector surface (Fig. 1.8.a). Therefore the spatial resolution for a pixilated detector design is strongly dependent on the detector width w and changes from $w/2$ for triangular CRF shape, to w in case of square shape CRF (Fig. 1.8.a). In case of continuous detectors with intrinsic resolution ϵ_{int} described by the FWHM of a Gaussian, the CRF changes from $\epsilon_{int}/\sqrt{2}$ to ϵ_{int} depending on the source position between the coincidence detectors (Fig. 1.8.b).

In modern PET scanners the individual crystal detectors are cuboid measuring typically $4 \times 4 \times 30\,\text{mm}^3$. The small width of the pixel, as explained above, is required for good spatial resolution. On the other side, a small end causes less light output, then a bigger exit surface. This can degrade an energy resolution (see §.1.4.4) and sensitivity (see §.1.4.2). To ensure a reasonable detection efficiency, longer crystals are preferred. However longer crystal causes annihilation position estimation inaccuracy that affects the spatial resolution. The problem is that annihilation photons can interact in the whole volume. Considering a standard ring geometry of the scanner, all photons emitted from the center of the field of view (FOV) impinge perpendicular on the detector surface of scintillator. In this case the intrinsic resolution is determined by the CRF. When the radiation source is out of the scanner center, the annihilation photons may penetrate through the crystal, it impinge on, and be detected in the adjacent elements (Fig. 1.9). As a *paralax effect* consequence, the LOR is misplaced and the CRF becomes broader. This issue is
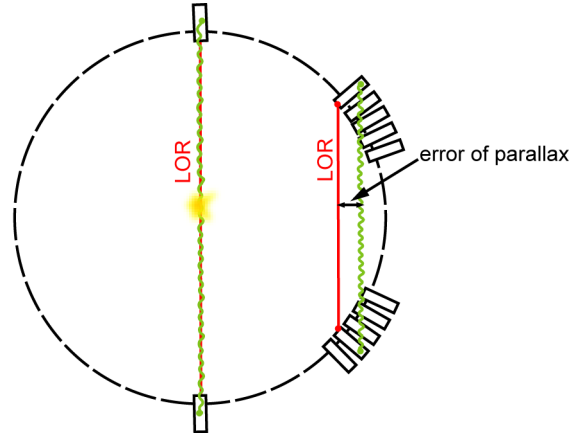
Figure 1.9: *The parallax effect.*

called *the parallax effect* and depends on the detector ring diameter and scintillation crystal parameters: the width, the length and the crystal material properties, like stopping power (see chapter 2). The parallax effect can be minimized by measuring the exact point of the annihilation photon interaction in the crystal. That method is known as Depth of Interaction (DOI) measurement. The approach presented in this work automatically avoids the error of parallax, by estimating the incidence point on the crystal surface, not the interaction point inside the crystal volume. The function fit to the histogram of differences between the real and estimated impinging point is called *line spread function* (LSF), when we look at only one coordinate, or *point spread function* (PSF), when we look at both coordinates. The FWHM of these functions characterise the spatial resolution.

system spatial resolution   The final system spatial resolution Γ (expressed in FWHM) near the center of the FOV, for a most common pixelated detector type, is described by the equation [Moses1997, Moses1993]

$$\Gamma \approx a\sqrt{\left(\frac{w}{2}\right)^2 + \Delta_{\mathrm{nonc}}{}^2 + r_{p.range}{}^2 + b^2} \tag{1.6}$$

where the first factor corresponds to the intrinsic detector resolution in the center of a ring of diameter D (w is the pixel width). The next two factors correspond to the influence of the annihilation non-colinearity Δ_{nonc} (Fig. 1.7) and positron range r_{positr} (Fig. 1.5). The factor b is an additive error caused by the not perfect decoding process. It is possible that the decoded fired pixel position somehow doesn't correspond to the pixel where annihilation photon interact. The factor a arises from tomographic reconstruction. For a typical image reconstruction algorithm, as filter back projection, it is $1.2 - 1.3$ [Lecomte2007b]. Theoretically for images obtained without reconstruction algorithm a would be 1. In practice such setup does not exist.

One practical factor that changes the image spatial resolution is *patient motion*. Controlled movements of the body are easier to avoid, but in case of involuntary motions, like blood flow or heart beat, extra mathematical algorithms need to be applied.

1.4.2 Sensitivity

The system sensitivity is also one of the most important PET design factors that determines the final image quality. The sensitivity is defined as the number of useful coincidences events obtained for a given activity in the object or patient being imaged. The number of collected events depends on the radioactivity accumulated in a tissue, the time of examination, and the sensitivity. Considering approximately constant number of useful coincidences for reasonable image reconstruction, a higher sensitivity allows to reduce the radioactive dose introduced into the body or the scanning time. The first two of the parameters are in practice limited by the patient safety reasons and the patient comfort. In case of small animals, too much tracer destroys the activity distribution by tracer uptake in whole body not only in imaged tissues. Observed process may be not visible. The lower radioactivity dose and the shorter the examination, the better. The sensitivity is the the only parameter that can be improved in practices. It refers to the efficiency with which the detector converts radiation emission from the source into a useful signal. The true coincidence rate registered by a PET scanner T is given by [Cherry2003] equation

$$T = A_o \cdot \varepsilon_{intr}{}^2 \cdot \varepsilon_{geom} \cdot e^{-\mu_o \cdot l_o} \tag{1.7}$$

where A_o is the source emission rate dependent of its activity, ε_{intr} the intrinsic detector efficiency, ε_{geom} the geometric efficiency. The scanned material properties are represented by μ_o and l_o, the linear attenuation coefficient and total thickness of the object. The source emission rate is indicated by the source activity, but may be reduced by absorption and scattering of radiation in the examined subject. Two of the most important sensitivity factors are the detector efficiency and the geometric efficiency.

The geometric efficiency is the probability that the annihilation photons are directed to the coincidence detectors. This is mainly determined by *the solid angle* coverage of detectors around the object. Theoretically, to ensure a maximum solid angle and to collect all annihilation photons, the PET detector should completely cover a sphere around the patient. This concept is unrealistic for several reasons. First, there would be a problem with placing a patient in such a scanner. Second, considering a heavy scintillation material, the overall device weight would be uncomfortably high. Such scanner would be also to expensive in comparison with its advantages. In a typical PET scanner a more useful architecture is applied. With respect to sensitivity, up to a few detector rings is enough to gather a sufficient amount of proper events, required for a good image quality. Common designs consider even part of the ring, with the ability of rotation around the object. *geometric efficiency* *solid angle*

From "better use of radiation" point of view, the big PET advantage is also the usage of an electronic coincidence approach instead of a collimator, like in SPECT. In single photon techniques, the use of collimator reduces the number of detected photons for a given amount of radioactivity in the body. Instead, PET takes the advantage of back-to-back annihilation photon emission and thus increase the sensitivity. *electronic coincidence*

On the other hand, a geometrical packing of the typical cuboid shape detector modules in the scanner gantry creates free volumes in between and finally reduces the detection efficiency. There are efforts to introduce more optimal detector shapes (for instance trapezoidal) to minimize them. For instance, to enhance the *dead spaces*

sensitivity the crystal length can be increased, but on the other hand it crates parallax error.

Insensitive regions, known as *dead spaces*, appear also if considering the packing of pixels of the light sensor or, in case of pixelated detector, in the array between the crystal elements. This kind of dead space refers more to the intrinsic detector efficiency, rather then to geometric. It is more dependent on a detector manufacturing process and it is often difficult to change. The inter pixel dead spaces problem can be described as *a packing fraction* and are defined by the ratio of the active detector element face (or volume) to the total detector surface (or volume), that includes the dead area (or volume).

The number of registered coincidences is also dependent on the radioactive source location between the detectors. Due to solid angle difference, it is bigger if the source is in the center of FOV of the detectors then at the edge. Generally the geometric efficiency is set by the compromise between several factors like the ring diameter, the detector shape, and practical factors as for example the cost of examination.

The intrinsic detector efficiency   *The intrinsic detector efficiency* means the fraction of photons impinging on detector that interact with the detector. This factor is mainly determined by the material properties of the detector. There are three effect when photon interact with the crystal matter in the detector [Leo1992]. The first, is *the photoelectric absorption*. In the photoelectric effect, the total energy of the gamma ray is transferred to an electron present in the scintillator. This electron subsequently loses energy by exiting atoms along its path and eventually part of this energy is emitted as visible light.

photon interaction with matter

The second process, known as *Compton scatter*, takes a place when the photon recoils from an atom and only a part of its energy is transferred to an electron excitation. Dependently on a remaining energy, the scattered photon continues travelling and may undergo next scatters, photoelectric absorption, or escapes from the detector. The best situation for annihilation point estimation is photoelectric absorption.

The third effect of photon interaction in matter is a pair production, but since it can only occur for incident photon with an energy above 1022 keV, it is not relevant for the present discussion.

photo fraction   A very important parameter of the scintillator materials is *the photo fraction*. It is defined as the ratio of cross section for the photoelectric effect (σ_{phe}) to the
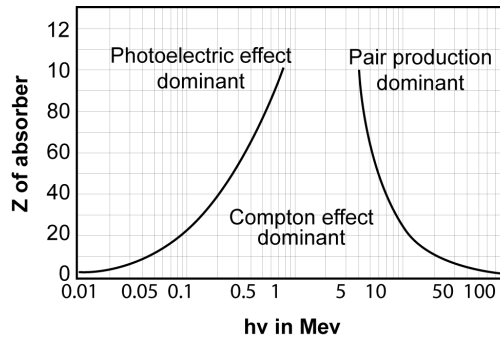

Figure 1.10: *Photon interaction in matter effects according to the photon energy and the atomic number of absorber Z [Evans1955].*

total cross section ($\sigma_{phe} + \sigma_{\text{Compton}}$). For a good PET detector, scintillators should provide high photo fraction. The photo fraction increases with the atomic number Z, because

$Z_{eff}, \; \rho, \; \mu, \; l$

$$\sigma_{phe} \approx \frac{\rho \cdot Z_{eff}^n}{E_\gamma^m} \tag{1.8}$$

$$\sigma_{Compton} \approx \frac{\rho \cdot Z_{eff}}{A} \tag{1.9}$$

where ρ is a density, whereas n and m are both function of the energy: n is about 4 at 100 keV and gradually rises to 4.6 at 3 MeV, whereas m decreases slowly from 3 at 100 keV to 1 at 5 MeV [Humm2003]. In case of cross-section for Compton scattering A is the mass number and the relation Z_{eff}/A is nearly constant. For a compound material, one should consider the effective atomic number Z_{eff}. For a $B_p C_q D_r$ compound Z_{eff} is defined by

$$Z_{eff}^x = \frac{\sum_i k_i A_i Z_i^x}{\sum_j k_j A_j} \tag{1.10}$$

where Z_i is the atomic number of respectively B, C or D. The atomic masses of B, C or D are denoted A_i and A_j. The indexes k_i, k_j correspond to p, q and r. For the photoelectric effect $x = 3 - 4$. The linear attenuation coefficient for the photoelectric effect μ

$$\mu \sim \frac{\rho Z_{eff}^{3-4}}{E_\gamma^{1-3}}. \tag{1.11}$$

Even for high Z materials, the photo fraction is limited to about 40% (Fig. 1.10). The intrinsic efficiency depends on both linear attenuation coefficient μ and the crystal element length l [Levin2007]

$$\varepsilon_{intr} \sim \left(1 - e^{-\mu l}\right). \tag{1.12}$$

Therefore, from sensitivity point of view, rather long crystals are preferred. The coincidence requires detection of both annihilation photons, thus the system efficiency is proportional to the square of the intrinsic detector efficiency.

The next parameter describing valid signals loss is *dead time*. It is the time that, after a single event, the detector is not ready for accepting a next event. To handle a high frequency of incoming photons, the detector should be fast. In case of scintillators, dead time is ultimately determined by the decay time (see §.2.1).

Some of the events can be also rejected by the energy selective window, but generally these event should not be interesting for good image reconstruction. The feature of PET technique is that all back-to-back emitted photons have an energy of $511 \, \text{keV}$ independently of the element involved or the energy of the emitted positrons. This can be seen as an advantage, since PET scanners are optimized for imaging at this single energy. On the other hand, it is not possible to perform dual-radionuclide studies, like in SPECT. Summarising, intrinsic detection efficiency depends on the effective Z, density, crystal thickness, dead time and dead space of the detector surface as well as on the energy window settings.

1.4.3 Types of coincidences

In a PET scanners, only *true coincidences T* originating from the same positron annihilation and where non of the gamma rays underwent Compton scattering, are useful for image reconstruction purpose (Fig. 1.11.a). However, not all of the detected coincidences are true coincidences.

scatter coincidences   *Scatter coincidences* S occur when both of the 511 keV photons come from the same annihilation but at least one undergoes Compton scatter inside the object (Fig. 1.11.b). They reach the detector simultaneously with respect to the $\Delta\tau$, that can be interpreted as a coincidence. Therefore the system is not able to distinguish scatters from a valid events. As a consequence the LOR is mismatched and doesn't go through the annihilation point. In this case the emitting source can even be placed out of FOV. The scatter-to-true ratio is independent of activity, because both the true and the scatter coincidences rates increase linear with this parameter. This ratio also doesn't depend on coincidence time window length, because it arises from the same positron annihilation and the two photons actually arrive almost simultaneously at the two detectors. Scatters are part of the background.

single events   The most numerous are *single events* N, when only one of two detector registers

a. True Coincidence   b. Scattered Coincidence

c. Random Coincidence   d. Multiple Coincidence
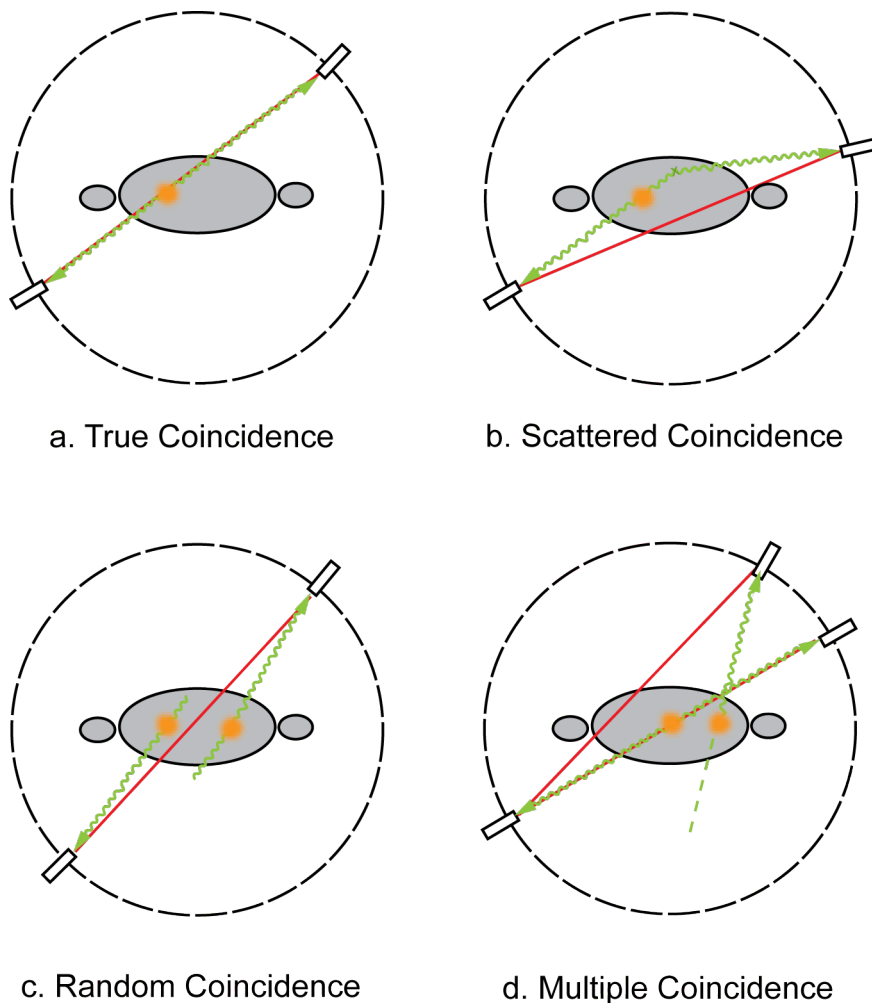
Figure 1.11: *Different types of coincidence events: a.) true coincidence event, b.) scatter event, c.)random coincidence event, d.) multiple coincidences. Red line is the LOR, green corresponds to the gamma path.*

a photon. The partner photon may be directed out of the detection surface, or may deposit not sufficient energy to be registered in the detector. A single event can also be caused by self radioactivity of the scintillator or from surrounding radiation. Although singles are not accepted by the PET, they are responsible for randoms and multiple coincidence events. In addition single events add extra dead time, because the system must to check for coincidence every time, when a single is detected.

The random coincidences R, also known as accidental coincidences, occur when two unrelated singles are detected within the same time window $\Delta\tau$ (Fig. 1.11.c). *random coincidences* This time window is a feature of the scanner and the random rate R is proportional to it. Therefore it is very important to make the time window not longer then necessary. Randoms send false information to the scanner and degrade the spatial resolution. If the single rates of both individual detectors are N_1 and N_2, then the random rate is given by

$$R = N_1 \cdot N_2 \cdot \Delta\tau \tag{1.13}$$

Because the N_1 and N_2 are directly proportional to the activity in the FOV of the scanner, the R is proportional to the square of the activity in the FOV.

If the rate of detector counting is high and if more detectors are involved in *multiple* the detection process, then because of finite length of the coincidence time window *coincidences* there is some possibility to register *multiple coincidences* (Fig. 1.11.d). Usually these events are rejected. Nevertheless these events are often composed of one true coincidence together with a single event. These type of events may carry valid information, however it is hidden and rather not possible to use.

The relation between the sensitivity and activity is quite complicated. The *NECR* better parameter of the image quality is the signal-to-noise ratio SNR. The SNR is related and usually expressed by the *Noise Equivalent Count Rates* (NECR). It is defined as the coincident count rate equivalent in terms of noise in a measurement that does not include scattered or random coincidences. The NECR is given by [Strother1990]
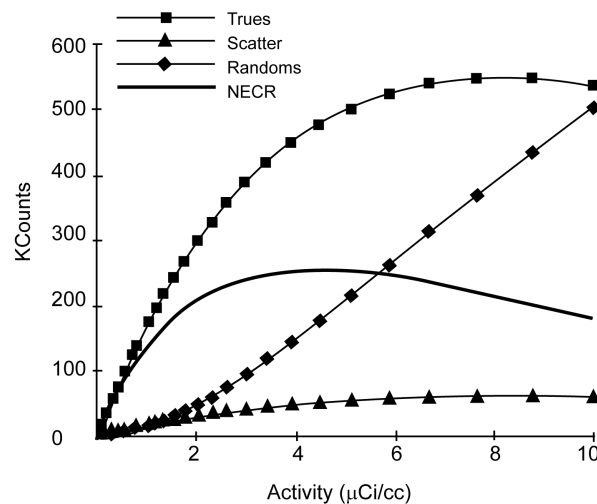
$$NECR = \frac{T^2}{T + S + fR} \tag{1.14}$$

Figure 1.12: *Example of the variation of each type of coincidence events and the NECR with respect to the activity [GE].*

where *f*, depends on the randoms correction procedure. It equals 1 for a noiseless random correction (when the randoms are measured according to Eq. 1.13) or for delayed coincidence window is 2 [Strother1990]. Since the single rate is proportional to the activity of the introduced tracer, the true coincidences for higher activities will not increase due to dead time of the detector, and the random fraction will be more significant. Thus the NECR will decrease with growing activity as shown on the Fig. 1.12.

1.4.4 Energy resolution

energy spectrum   The energy spectrum is the histogram showing the number of detected events, versus the amplitude of those events. The amplitude reflects the energy accumulated in the detector from the impinging photons. The energy deposited in the detector can be smaller then the full energy of the incidence photon. The spectrum is determined by the photon interaction processes in matter, explained in last section (see §.1.4.2). The ideal spectrum, for the source placed in the front of the detector, predicts a narrow line peak at the 511 keV, known as *the photopeak*, that comes from full photo electric absorption of annihilation photons. During Compton scattering, only a part of the photon energy is transferred to the detector. If the scattered photon is also absorbed, then this event produces a pulse in photopeak, but if it escapes the scintillation crystal, the deposited energy is lower then 511 keV. These events generate *the Compton region*, with the edge at the energy of the electron recoiled at 180°. The valley between the Compton edge and the photopeak corresponds to the multiple Compton scatters (Fig. 1.13.a). Due to errors on the measurement of the energy deposit, the photopeak line is broadened and the Compton edge is however smoother (Fig. 1.13.b).

Fluctuations in the pulse height distribution for a scintillator based APD detector can be written:

$$\sigma_{tot}^2 = \sigma_{intr}^2 + \sigma_{stat}^2 + \sigma_{noise}^2 \tag{1.15}$$

where σ_{intr}^2 intrinsic energy resolution, σ_{stat}^2 represent statistical fluctuations and σ_{noise}^2 the electronic noise contribution. The statistical variations come from statistical fluctuation in number of scintilation photons per uniform deposited energy in scintillator. Moreover in case of APD the the gain fluctuations, given by excess noise factor F (see §.2.2.2), have also contribution. Even if there were no statistical fluctuations, the photopeak would still be broadened by the intrinsic energy reso-
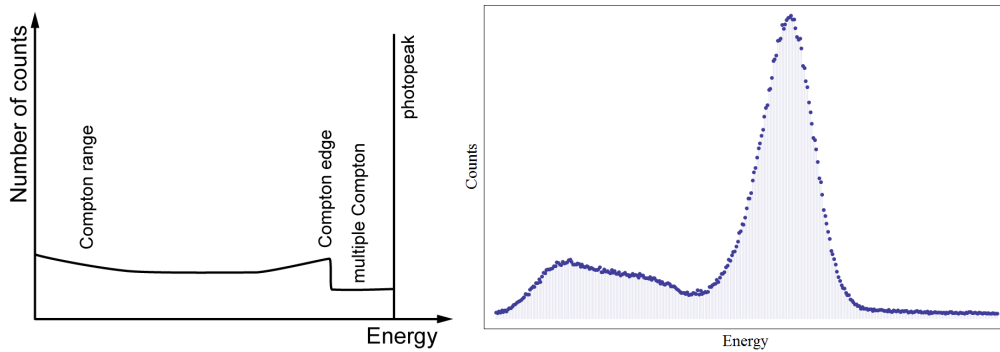
Figure 1.13: *Energy spectrum: a) ideal, when only the photpeak represent deposition of the full energy of the gamma ray, b) actual pulse high spectrum recorded with ^{22}Na.*

lution. It is given by non-proportional scintillator signal response (the light yield (LY) depends of the energy of the incidence photon energy, see §.2.1), inhomogeneity of the scintillator resulting in local light output variations. The intrinsic energy resolution is also contributed by the not ideal covering of the crystal causing nonuniform reflectivity on the edges. The last element of the Eq. 1.15 consist of all kind of electronic noise (e.g. amplifier noise, pick-up and dark current). The detailed discussion of the noise in monolithic block type detectors can be found in [Maas2008a].

Usually the spectrum is limited to the energy window thresholds that accept only events close to the photopeak energy. *The energy resolution* is given by the FWHM of the photopeak divided by its energy E_{ph}, i.e. FWHM percentage of the photopeak at 511 keV:

$$\frac{FWHM}{E_{\mathrm{ph}}} \cdot 100\% = \frac{2.35 \cdot \sigma_{ph}}{E_{\mathrm{ph}}} \cdot 100\% \tag{1.16}$$

where σ_{ph} comes from the Gaussian fit to the photopeak. A good scanner should provide a narrow energy resolution. Narrow energy resolution allows to use smaller energy window to reject more scatter events effectively, that are numerous in the realistic PET scanner. The energy resolution depends on the detector type. Considering LSO scintillator (see §.2.1) based detector, the it can be pushed to $\approx 10\%$, only if the electronic noise contribution can be omitted. However in a good realistic scanner it usually varies around $\sim 20\%$ of the 511 keV.

There are practical efforts that can help to slightly improve the photopeak width. For a larger scintillation crystal (see §.2.1) it is more likely that the whole Compton scattered photon will be absorbed. Thus the photofraction increases due to a growing number of events in photopeak and decreasing in the Compton range. Some influence for a photon transfer from the scintillator to the light converter has the coupling material. If it is not uniform then it can change the output signal amplitude.

<div style="text-align: right">

2

PET detectors

</div>

In the first part of this chapter, the scintillator material is described, its characteristics, mechanism of operation and most common types. The second part is concentrated on light sensors such as PMTs and photodiodes. The biggest emphasis is put on APD detectors, its working principle and main parameters. The promising SiPM detectors are also mentioned.

The aim of a PET detector is to stop as many of the 511 keV gamma rays as possible and to produce output signals that can be detected, saved, and analysed. A good PET detector should have the following properties [Lewellen2008, Humm2003]: *main PET detector requirements*

- high efficiency, high probability that 511 keV photon is detected,

- high spatial resolution (typically less then 4 mm FWHM),

- good energy resolution (typically less then 20%), to reject scattered events,

- good timing resolution (typically less then 5 ns FWHM for conventional PET) as well as a low dead time (less then 4 μs)

- low costs

Nearly all PET detectors are based on the use of *inorganic scintillators*. When radiation passes through matter, it deposits energy by interactions with atoms and molecules. It is done in two ways: by ionization or excitation. When ionized or excited atoms undergo recombination or de-excitation, energy is released. Most of the energy is dissipated as a thermal energy, like molecular or lattice vibration (dependent on material). However, in some materials part of the energy is released as a visible or UV light. When coupled to a photodetector, the light from the scintillator can be converted into electrical pulses that can be electronically counted and further analysed. This signal gives information about the energy deposited in the detector, the location of the event in the detector and the time of occurrence of the interaction.

2.1 Scintillators

2.1.1 Characteristics of the ideal scintillator

When ionising radiation interacts with matter, it will excite or ionise a large number of atoms. When these atoms return to the ground state, this will sometimes give rise to the emission of photons in the visible or near to the visible energy range. This phenomenon has as scientific name *radioluminescence*. If the light emission decays fast, i.e. of order of ns − μs, the effect is called *scintillation* and emitting materials *scintillators*. Whereas if the light emission continues for a long time after the excitation, i.e. much longer than 1 ms, this phenomenon is called *phosphorescence* and the corresponding material is called *a phosphor* [Tavernier2010].

A different but related phenomenon is *photoluminescence*. This is the emission of visible or near to visible light under stimulation by the light of a shorter wavelength. Again if the emission decays fast $(10^{-8}\,\mathrm{s})$ after excitation the effect is called *fluorescence*. In the case of a material that does not immediately re-emit the radiation it absorbs, the phenomenon is called *phosphorescence*, the same as in radioluminescence. The phosphorescence light can remain even a few hours after taking away the exciting source.

The PET detection technique employs only the scintillation effect because it is fast. Although many scintillators exist, not all are suitable as a detector. Most transparent materials will produce some small amount of scintillation light when hit by a high-energy particle or a high-energy photon, but usually this light signal is very weak. Only in a few scintillation materials the conversion of the excitation energy into light is efficient. In general, a good scintillator for PET should satisfy the following requirements [Humm2003, Melcher2000]:

main scintillator requirements

- High intrinsic detector efficiency is ensured by both **high effective atomic number** Z_{eff} and **a high density**. It results in a large photoelectric cross section, and therefore in a large photo fraction (see §.1.4.2).

- For good coincidence timing and a high counting-rate capability determined by a short dead time, **a short decay constant** is required. There should be no delay in light emission as well.

- **A high light yield (LY)** means a high number of photons emitted per MeV radiation energy deposited in the material. A high LY implies a better energy resolution and more accurate spatial resolution and better time resolution. It describes how often energy is spent to create a photon, rather then being lost for other effects (for instance crystal lattice vibration). LY is the parameter describing the light efficiency of the scintillator. The amount of emitted light should be proportional to the energy deposited in scintillator.

- **Emitted wavelength** should be compatible with the light converter. Moreover, the scintillator should be **transparent** for the light in that wavelength range. Also, its **attenuation length** should be much longer then the crystal thickness, to minimize self-absorption of the fluorescence light. The transmission of the fluorescence light pulses into the photodetector is best when **the refractive index** of the scintillator material is similar to that of the

entrance window and coupling material, usually near 1.5. These parameters allow for good communication between the scintillator and the light detector, and provide good detection efficiency. From an experimental point of view, a good light collection is provided by enclosing the crystal in a reflective light tight case at all surfaces except at the entrance window of the photodetector.

- **Low cost** and **availability on the market** is also not a negligible factor. Apart from marketing reasons, it is determined by **the scintillator production process** (in case of crystals, the crystal growth), that should be reasonable economic.

- At least in some materials, ionizing radiation may easily produces color centres, thus destroys light transparency and impeding its transmission of the scintillation itself. Therefore, a resistance for this effect, known as **radiation hardness**, is desirable.

- Considering convenience application, **non-hygroscopic** scintillators are preferred. Hygroscopic materials readily absorb water from the atmosphere and therefore require a special packaging to hermetically seal them. Moisture causes the crystal to develop yellow spots, which causes uneven light transmission.

- Finally mechanical **ruggedness** is desirable, because it makes crystal production easier.

However, the ideal scintillator doesn't exist. The proper choice needs to be done considering a specific application. The characteristics of some commercial scintillators are presented in section 2.1.3 and Table 2.1.

Table 2.1: *Commonly used scintillators properties [Derenzo2010, Lewellen2008, Humm2003].*

	NaI(Tl)	BGO	LSO	LaBr$_3$	LuI$_3$:Ce
Density ρ [g/cm^3]	3.67	7.13	7.40	5.3	5.6
Effective atomic number Z$_{\text{eff}}$	51	74	66	47	60
511 keV photo fraction [%]	17	40-44	32	15	
Light yield (LY) [photons/MeV]	41000	8000	30000	60000	100000
Decay constant [ns]	230	300	40	15-25	23-30
Refractive index	1.85	2.15	1.82		
Peak emission [nm]	410	480	420	370	470
Mean free path, abs. length [cm]	2.59	1.12	1.14	2.13	1.7
μ Linear attenuation coefficient at 511 keV [cm^{-1}]	0.34	0.92	0.85		
Hygroscopic	Yes	No	No	Yes	Very
Rugged	No	Yes	Yes	No	No

2.1.2 The scintillation mechanism of inorganic scintillators

There are two types of scintillators: organic and inorganic. The first type exist in three forms: organic crystals, organic liquids and the widely used plastics.
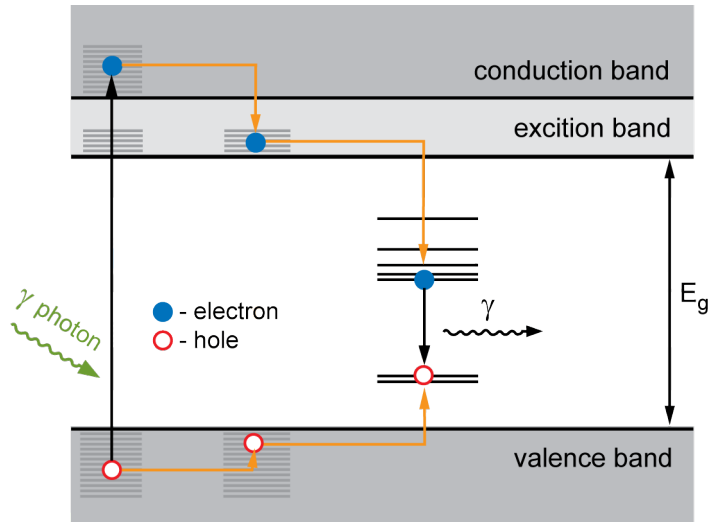
Figure 2.1: *Scintillation crystal band structure scheme.*

Inorganic scintillators are usually in form of ionic crystals. Only the second type found application in PET, because many of them contain a large fraction of atoms with a high atomic number Z, and therefore a short radiation length (see §.2.1.1). Because of this difference, organic scintillators are mainly used for charged particle tracking or "fast neutrons" [Tavernier2010]. Whereas the scintillation process in organic materials is molecular in nature, that in inorganic scintillators is clearly characteristic of the electronic band structure of the crystal [Leo1992]. Stretching of allowed energy levels into bands, is the result of mutual interactions between atoms, in this case, of the crystal lattice of scintillator. When the 511 keV anni-hilation photon enters the crystal, two main mechanisms can occur. It can ionize the crystal by exciting an electron from the valence band to the conduction band, creating a free electron and free hole. Or it can create an exciton by exciting an electron to the exciton band, located just below the conduction (Fig. 2.1). In this state the electron and hole are bounded together as an $e - h$ pair. When the electron de-excites to the valence band it emits the energy, sometimes in the form of visible or UV light. Thus when a gamma is absorbed in the lattice, thousands of $e - h$ pairs are crated with a broad spectrum of energies. All will at least contain the ionisation energy E_i together with an unpredictable amount of kinetic energy. Average energy needed for electron excitation in typical insulator is more then two times higher then the energy of the band gap E_g. Typical excitation energy is about 3 E_g [Lempicki1997]. From this point of view a small band gap is preferred to have a good conversion efficiency.

The parameter influencing the SNR is the light yield (LY) of the scintillator and the non-proportionality. The LY is the number of photons generated in the crystal per unit of energy and it should be high to provide a good SNR.

Nevertheless, the transition with the emission of forbidden gap energy is not interesting in PET, because it is not in energy range the light sensor detect. Even if it partially is, the absorption and emission energy ranges overlap and finally all light is again re-absorbed. These problems are solved by doping the scintillator crystal with impurities atoms e.g. cerium. Thus luminescence centres are created in the crystal lattice, by arising local activation levels in the forbidden energy gap (Fig. 2.1). When excited electrons and holes, travelling in the lattice, encounter

the impurity centre, they are trapped on the levels inside energy gap. Then if a de-excitation mode is allowed, the electron momentarily makes a transition to the ground level with a high probability for the scintillation light emission. Therefore, the forbidden energy gap can not be too small (as mentioned above) since the levels of luminescence center need to fit within. Very important is that the centres are distributed locally but also densely enough. An excited electron need to find a luminescence trap quite fast, before it will be trapped. If the scintillation material is transparent, than in good conditions the scintillation light signal can easily be extracted.

The quantum efficiency η is the average number of optical photons produced for the interaction of one gamma ray in the scintillation [Lempicki1995]. It is given by

$$\eta = \beta S Q. \tag{2.1}$$

As is shown in equation above, the η is a product of three factors. The conversion efficiency β denotes the number of $e - h$ pairs created by the absorption of a impinging gamma photon by a crystal. The transport efficiency S describes the probability that the $e - h$ pairs find a luminescence centre. The last one is the quantum efficiency of the luminescent centre Q. This is the fraction of excited luminescence centres that actually emits scintillation photons. Q is not unity because other competitive non-radiative processes can convert the energy to elastic vibrations, e.g. phonons, quantized modes of vibration occurring in a crystal lattice. The de-excitation of captured electron and holes, which result in radiationless transitions, is called quenching. This mechanism is determined by many factors such as other impurity atom, structural defects during crystal growth, etc. Fluctuations in number of scintillation photons, produced by the crystal cause broadening of the photopeak in the energy spectrum.

2.1.3 Characteristics of commercial PET scintillators

A perfect PET scintillator doesn't exist yet, thus the choice of a scintillation type is determined by destined application dealing with their properties (example of common crystals characteristics in Table 2.1). Due to its high LY NaI(Tl) is since many years the workhorse for gamma rays detection. It was discovered in 1948 *NaI(Tl)* by [Hofstadter1948]. However, NaI(Tl) has a relatively low density and a rather small atomic number, that causes low detection efficiency for higher energies, like used in PET. It is satisfactory for SPECT, where the energy is typically under 200 keV. An additional disadvantage of this crystal is its high hygroscopicity.

NaI(Tl) was used in the first PET scanners, but in 1973 Weber [Weber1973] introduced a better scintillator. It was bismuth germanate ($Bi_4Ge_3O_{12}$), known in its shorter form as BGO. First of all, it is a relatively hard, rugged, non-hygroscopic *BGO* crystal, which does not require hermetic sealing. Although the LY of the BGO is around 5 times less then NaI(Tl), its detection efficiency is dramatically higher. It is the result of its density, that is almost twice of NaI(Tl) as well as a much higher atomic number. Besides low LY, a significant disadvantage of BGO is relatively long decay time, around 300 ns. It finally leads to a reduction in energy resolution, while the pulse integration time is reduced. Another disadvantage of BGO is that the fluorescence intensity increases by 1% per 1°C decrease in temperature. It requires a scanner that is well regulated in temperature.

BaF₂   One of the scintillators with extremely short decay constants is BaF_2. This material is suitable for the TOF method in PET (chapter 1.3). BaF_2 is also non-hygroscopic. In the early 1980s it was used in several PET scanners. However, because of its relatively low density and atomic number, it eventually was abandoned in favour of BGO and LSO.

     A significant milestone in the development of PET scanners was the introduction, by Melcher [Melcher1990] in the nineties, of Lutetium Orthosilicate - Lu_2SiO_5 *LSO* (LSO). It offers the best combination of properties for PET among all scintillators known today. Similarly to BGO, LSO provides a high density and a high atomic number, and has therefore it has good detection efficiency. Moreover, the most important improvements are its very short decay time (about 40 ns), together with a high LY (around 30000 photons/MeV), as opposed to BGO. Observed main disadvantages are the non-proportionality of light output to the deposited energy, slight LY dependency on temperature [Fedorov2005], and a presence of a naturally long lived isotope of lutetium (^{176}Lu) within the crystal. However, lutetium self radioactivity is at low level, that a counting rate is a small fraction of the typical counting rates from the injected tracers. Finally LSO is not hygroscopic, but because it fluoresces when exposed to ambient light, it must be enclosed in a light-tight cover. Actually, the only significant disadvantage of the LSO in comparison with BGO is its lower photofraction.

2.2   Light sensors

     To convert the light from the scintillator into electronic signals, photodetectors are used. It needs to fit the most important requirements of PET detector, described on the beginning of this chapter. Nearly all commercial scanners in use today are of photomultiplier tubes PMT as photodetectors. Nevertheless, promising for PET are also the APDs and SiPMs. This section is focused on these three photodetectors.

2.2.1   Photomultiplier tubes

     The first photomultiplier tube (PMT) was produced by Zworykin in 1936, just around 30 years after discovering the photoelectric effect, that it is based on. Its significance, as a photodetector, is due to several reasons. One of the most important is its very high gain. It is especially important in case of a very weak signals from the scintillator. The most common commercial detector architectures consider a scintillation crystal or crystals coupled exactly on a PMT.

mechanism   Although PMTs are used since about 70 years, the principle of operation is still the same. Light goes through a glass window to *the photocathode*. Due to the photoelectric effect, a certain number of *photoelectrons* are released into the vacuum tube (Fig. 2.2). This number is proportional to the intensity of the light and thus to the energy deposited in the crystal scintillator. The efficiency of visible light conversion into photoelectrons is known as *the quantum efficiency* QE (typically for PMT is 25%). QE is a function of wavelength and temperature. Photoelectrons are directed on the first *dynode* usually by a focusing electrode. The dynodes are maintained at a positive voltage relative to the photocathode, attract the ejected photoelectrons and have high secondary emission characteristics. Photoelectrons
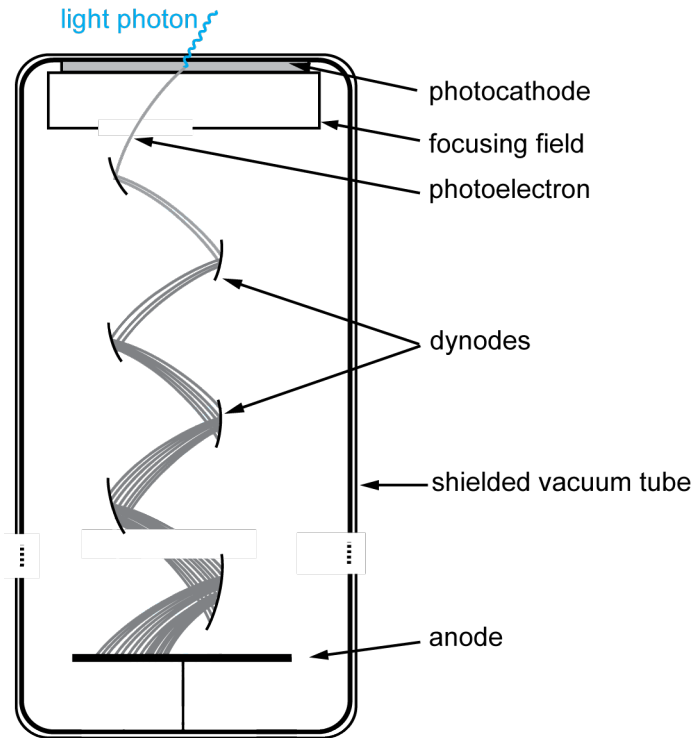
Figure 2.2: *The PMT scheme.*

increase their kinetic energy during acceleration and are able to knock out additive electrons from the dynode they imping on. The multiplication factor - *the gain* - depends on the photoelectron energy, determined by the accelerating potential difference between the dynodes. Each next dynode has a higher potential then the previous and again attracts electrons. This situation repeats until the electron shower finally hits the anode and creates an output signal. A multiplication factor is usually 3-6 per dynode and in total, for a typical 10-12 stages PMT, the gain is around 10^6 [Tavernier2010, Hamamatsu2007, Leo1992].

There are two main reasons of noise associated with the use of PMTs as pho- *noise* todetectors. A dark count noise, caused by *dark current*, that flows in PMT even if it is not illuminated. It has several sources. First of all it is thermal emission of photocathode referred to a system temperature. Additive contribution to the dark current is caused by unwanted gas atoms in the vacuum tube. These pulses may come a fixed time after a true pulse, thus they are known as after-pulsing. The residual atoms from a vacuum may be ionized by photoelectrons, then they can drift back towards the cathode and extract a large number of electrons at the same time. After-pulses correspond to many primary photoelectrons and can easily be confused with true signal pulses. This problem tends to increase as the tube ages but is also present in new tubes.

The second type of noise is *statistical noise*. It is based on the statistical nature of the electron emission in the PMT. First, the number of emitted photelectrons for the same amount of incidence light is not a constant. Also the secondary emission from dynodes fluctuates. The multiplication factor is strongly dependent on the dynodes voltages. Therefore supplies need to be very stable, especially because a standard PMT operates at very high voltages, $1000 - 2000\,\mathrm{V}$.

The PMT is relatively big in comparison with other available light sensors

and for PET compact modules are preferred. Another disadvantage, limiting its use, is its extreme sensitivity to magnetic fields. A PMT can be shielded against the Earth's magnetic field, but is difficult to shield from larger fields. This is particularly important in case of developing PET/MRI dual-modality.
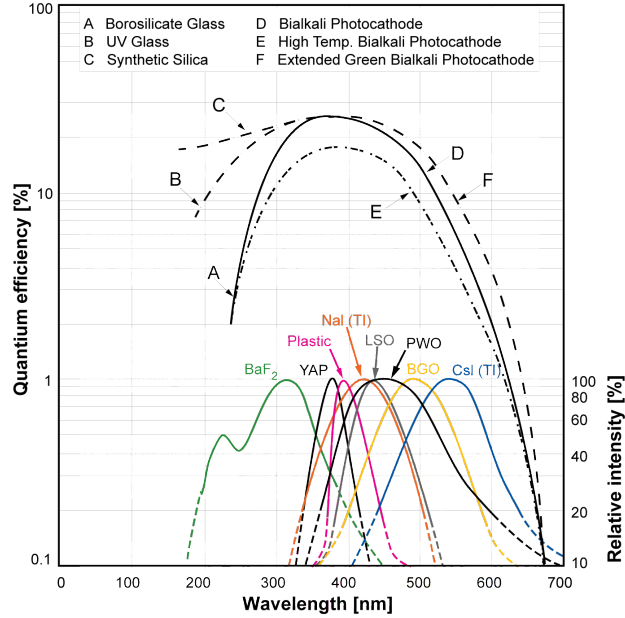

Figure 2.3: *Typical QE as a function of the wavelength for different PMT and scintillator types [Arisaka2010].*

2.2.2 Avalanche photodiode

Photodiode mechanism

A light converter that is alternative to commonly used PMTs are semiconductor photodiodes. They are based on *p-n* junction technology. The standard Si *p-i-n* photodiode (PIN) is the simplest, most reliable and cheapest photosensor. Nevertheless in medical applications its use is limited since that have no internal gain. Such detectors need a low noise preamplifier which adds to the costs, makes the output signal slower and the amplifier noise worsens the energy resolution. However, avalanche photodiodes (APD) are photodiodes with internal gain and these devices can be used in PET. An APD in general is built from an *n*-Si high-resistivity substrate, with a thin boron doped layer as p^+ from one side and phosphorus doped layer on the other, n^+ side. Its working mechanism is also similar to PIN diodes. Whereas the *n*-doped region has an excess of free electrons e in conduction band and almost no holes in valence band, whereas *p*-doped region has many free holes h in valence band and almost no electrons in conduction band. Both *n*-doped and *p*-doped regions are electrically neutral.

Semiconductor can be also described by the Fermi level, that refers to the energy of the highest occupied by electrons level at absolute zero temperature. For other temperatures and for thermal equilibrium the, the probability that particular level is occupied by an electron is given by the Fermi-Dirac distribution. For a pure semiconductor the Fermi level is located in the halfway between the conduction

PIN

APD

and the valence band. Whereas in *p*- type the Fermi level is located closer to valence band and in *n*- type closer to conduction band (Fig. 2.4).

When *p* and *n*-type silicon are in contact, they form a junction. Free charges diffuse to the adjacent region through the border, due to thermal agitation. Thus the excess of negative acceptor ions in the p-region and an excess of positive donor ions in *n*-region build up the potential difference and therefore electric field over the junction (Fig. 2.4). This diffusion process will stop when the generated electric field is strong enough to prevent any further free carrier diffusion. At this point the Fermi level reach equilibrium over the junction. The region where all free carriers are strongly removed by generated electric field is called *depletion region*. Essential point for photodiodes is that any of charge carrier created in the depletion zone is pushed to *n* or *p* side. Whereas charges created outside of the depletion region are not collected but recombine until thermal equilibrium is reached [Tavernier2010, Leo1992].

The depletion zone size is dependent on the magnitude and direction of applied voltage. Under *forward bias* (*p* to positive, *n* to negative), the contact potential is neutralized by remarkably increasing diffusion and decreasing the drift current components. Thus the depletion region is narrowed. With the forward bias higher then the contact potential, the *p-n* junction is able to conduct. The current that flow through the boarder is proportional to the concentration of majority charges.

Reversed bias (*p* to negative with respect to *n*) applied to the junction increase the drift current and decrease diffusion component on the contrary to the forward bias. Only a small drift current flows, and there are technological efforts
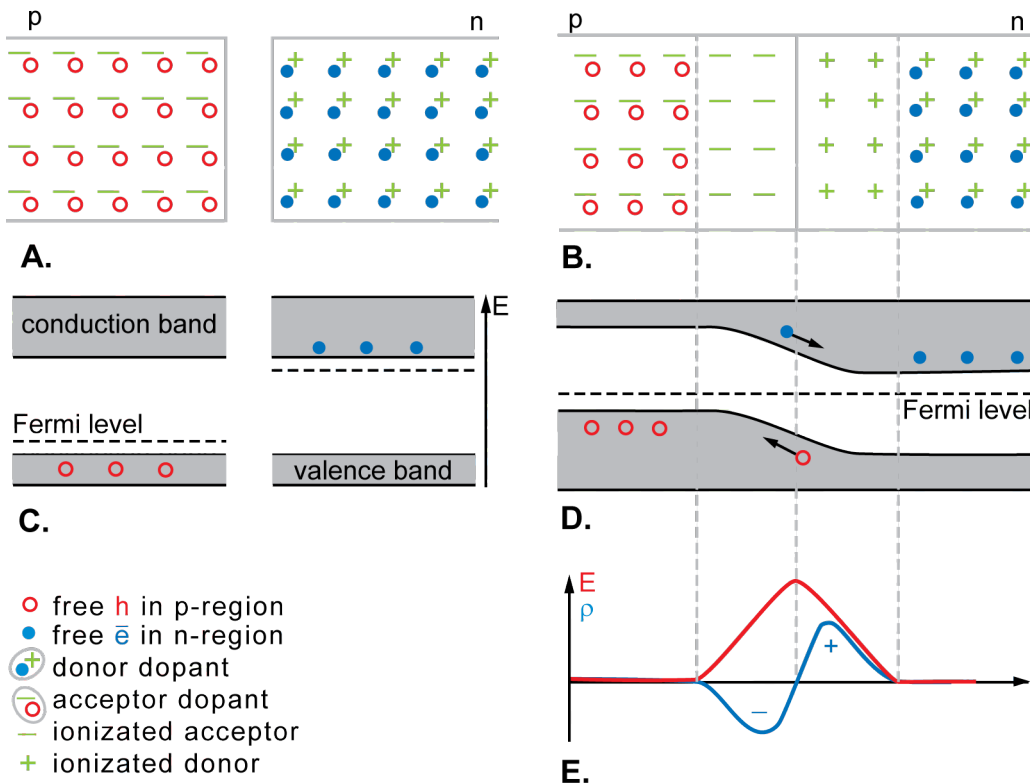
Figure 2.4: *The pn junction scheme. A.) p and n-type materials, B.) pn junction scheme with built up potential barrier, C.) band scheme of p and n materials, D.) band scheme of pn junction with built up depletion region.*
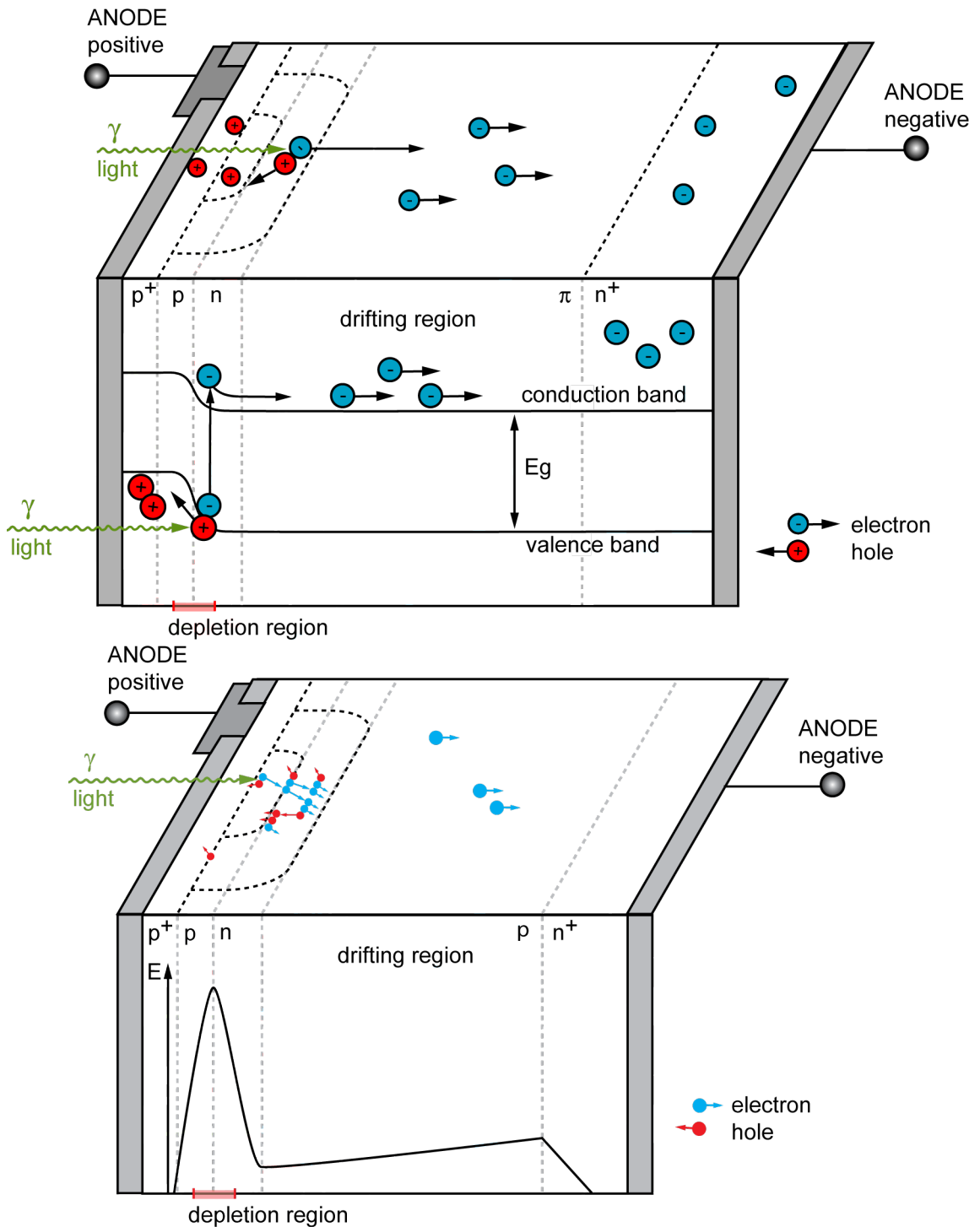
Figure 2.5: *Photodiode scheme: top.) scheme of signal detection in photodiode, b) avalanche creation scheme in a reverse reach-through APD.*

to extremely minimise it. The depletion zone is widened due to increased contact potential difference. Explained situation is interesting in APD, because it offers possibility of avalanche breakdown if high electric field is created and lowers the diode capacitance [Tavernier2010].

Silicon photodiodes change impinging light pulse into a $e - h$ pair in the depletion zone. This occurs only if the energy of the photon is higher then the band gap, for silicon is around $1.1\,\mathrm{eV}$ [Humm2003]. The electric field in the silicon pushes

created electrons towards cathode and holes to anode, creating the current that can be measured (Fig. 2.5). Each light photon produces at most one electron, so the signal levels are very low. In the APD problem was solved by applying much higher bias voltage. Increasing electric field to around $10^4 \, \mathrm{V/cm}$ charge carriers are more likely to collide with the crystal lattice. In consequence their drift speed is saturated to an average value about $10^7 \, \mathrm{cm/s}$. If continue increasing electric field, typically to $2 \times 10^5 \, \mathrm{V/cm}$, a phenomenon similar to the chain reaction appears. The carriers are accelerated between collisions and some of them reach enough energy to create further $e - h$ pairs in the silicon (Fig. 2.5). Naturally situation can repeat and an avalanche is formed [Hamamatsu2004], similarly as in PMT. Due to this internal amplification, the gain ranges between $10^2 - 10^3$. Only a small part of depletion region has strong enough field to create the avalanche. The drift region of APD (Fig. 2.5) is weaker, but from the other hand high enough to keep the carriers at average drift velocity.

Quantum efficiency

The APD has around four times better QE for conversion light photons from scintillator into electric pulses then conventional PMT. In case of photodiodes, quantum efficiency is defined by the number of $e - h$ pairs created by the incident photons, that can be written as

$$QE = \frac{\frac{I_{\mathrm{L}}}{q_e}}{\frac{P_{\mathrm{opt}}}{h\nu}}, \tag{2.2}$$

where I_{L} is the photocurrent, q_e the electron charge, P_{opt} the optical power of incident photon and $h\nu$ the energy of single photon.

The wavelength λ dependence on the quantum efficiency of a silicon photodiode can be explained as follows. The mean free path of optical photons in silicon is strongly dependent on the wavelength. It varies from $0.1 \, \mu\mathrm{m}$ at $\lambda \approx 400 \, \mathrm{nm}$ to $\sim 10 \, \mu\mathrm{m}$ at $800 \, \mathrm{nm}$. Photons with $\lambda < 400 \, \mathrm{nm}$ are stopped in the unavoidable dead layer on the surface of the silicon, and the quantum efficiency drops to a very low value (Fig. 2.6). For photons with $\lambda > 800 \, \mathrm{nm}$, the mean free path is longer than the thickness of the conversion layer and also in this case the quantum efficiency becomes low.

Gain and ionization coefficient

The gain factor is determined by the magnitude and fluctuation of the avalanche. If the electric field is sufficient over the junction, the carriers can reach enough energy to cause further ionisations during collisions. Situation can repeat until the $e - h$ avalanche appears. Under the breakdown voltage V_b the number of carriers is finite. Whereas above it can go to infinity.

The probability of ionising collision is described by *first Townsend coefficients*, also called *electron or hole ionization coefficient*. It is given by the number of $e - h$ pairs generated during the time at a given travelled distance. For electrons is marked as α, for holes β. This rates are sensitive for voltage and temperature changes. It increases fast with voltage and decreases with temperature.The gain increases exponentially with bias voltage
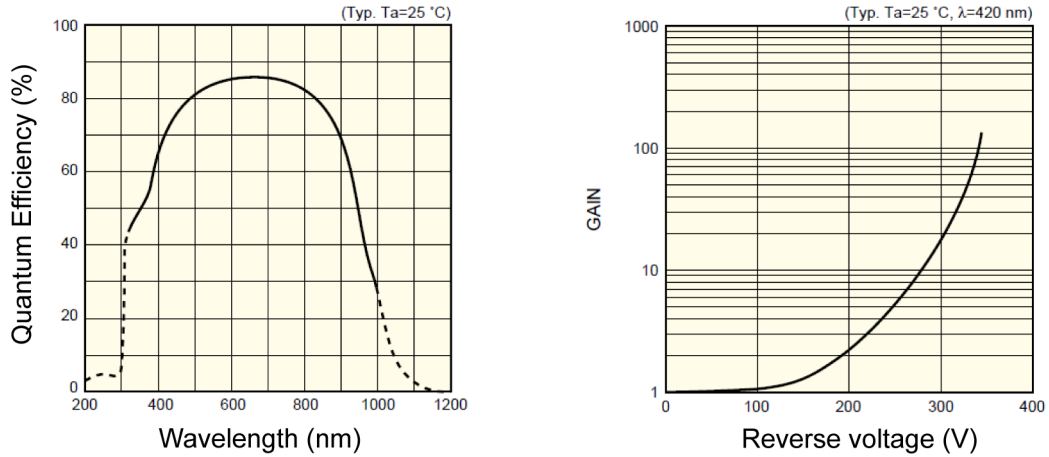
Figure 2.6: *Plots of quantum efficiency vs. wavelength and gain vs. reversed voltage in APD [Hamamatsu2006, Renker2002].*

Generally in APD more favourable is situation, when the avalanche is caused by only one type of carriers. It is referred by *an ionization coefficient*

$$k = \frac{\beta}{\alpha}, \tag{2.3}$$

that represents relative effectiveness of e and h to ionize new carriers. Ideally $k \to 0$, when the avalanche is created mainly by electrons, or $k \to \infty$, when holes carriers are dominant in avalanche building. This allows to increase the APD gain without increasing the excess noise factor to much (see §.2.2.2). However typical k is set to be of order of $0.4 - 0.6$. If both ionization rates are similar, the avalanche is growing more, because both e and h give arise to further carriers. Nevertheless this avalanche is unpredictable and finally may lead to breakdown the device, therefore ionization coefficient should be kept as $k \ll 1$.

Dark current

The output signal of APD is composed of two elements. First is photocurrent, that comes from photons detection. Second is *dark current* I_d (Fig. 2.7). It is understood as a current that flows in a phototodiode even in the absence of incident photons. It can be modelled from two parts [Hamamatsu2004, Chen1999]:

$$I_\mathrm{d} = I_\mathrm{ds} + M I_\mathrm{db}. \tag{2.4}$$

The surface part of the dark current, I_ds, is *a leakage current* caused by a current flowing on the edges of the APD and can be described as a resistor connected parallel to the APD. These charges are not amplified, because they don't enter the avalanche region of APD. *The bulk current I_db is generated in the depletion zone*, therefore it is fully amplified by a gain factor M (Eq. 2.4). The surface dark current dominates total I_d for smaller values of applied reverse voltage. When increase the reverse voltage, the bulk part arise to be dominant, because of amplification process (Fig. 2.8).
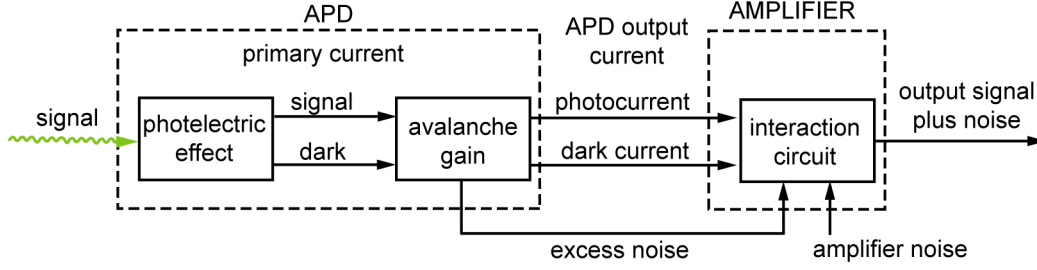
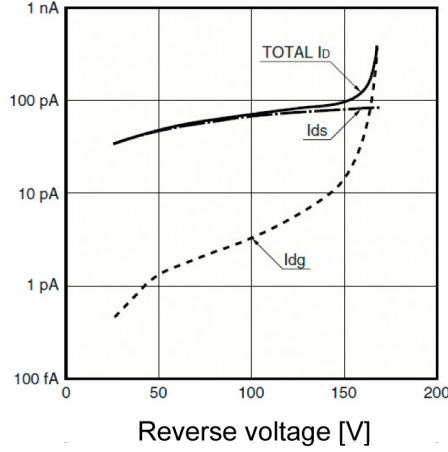**Figure 2.7:** *Photodetection process in APD [Fremout2002a].*

Figure 2.8: *Dark current vs reverse voltage [Hamamatsu2004].*

Excess noise factor

The excess noise refers to the statistical fluctuations in the amplification process. In a photodetector with internal gain, such as APD, the interactions of optical photons produce charges, and for each charge, the internal gain mechanism multiplies the number of charges. The number of primary charges created in the photodiode N by the same amount of light is statistical in nature and can be described by Poisson distribution law. All the charges are not multiplied by the same gain factor, and this is an additional source of fluctuations in the output signal [Tavernier2010]. This is described by *the excess noise factor* F (or ENF)

$$F = \frac{\langle M^2 \rangle}{\langle M \rangle^2} = 1 + \frac{\sigma_M^2}{\langle M \rangle^2} \tag{2.5}$$

where $\sigma_M \overset{df}{=} \langle M^2 \rangle - \langle M \rangle^2$ is the variance of the gain M. That expresses the broadening of the noise distribution to the non-delta shape of the single electron response.

The statistical fluctuations in pulse height can be written as

$$\sigma_{stat}^2 = M^2 \sigma_N^2 + N \sigma_M^2 \tag{2.6}$$

where σ_N is the statistical fluctuation of primary $e - h$ generated in APD by the scintillation photon and it is described by Poisson statistics consequently $\sigma_N^2 = N$. The second part of Eq. 2.6 consist gain fluctuations. Considering light sensor with uniform gain, as PMT, the second element is negligible and thus $\sigma_{stat} = M\sqrt{N'}$, where N' is the number of photoelectrons generated by the photocathode. In case

of APD, the gain variance can be rewritten with use of excess noise factor, as in Eq. 2.5, and consequently the statistical fluctuation are given by

$$\sigma_{stat} = M\sqrt{NF}. \tag{2.7}$$

For the same number of incident photons N will be 2 to 3 times bigger then N' due to the higher APD quantum efficiency $(60 - 70\%)$ then the PMT $(20 - 30\%)$. Apparently the excess noise caused by the multiplication process compensates this fact. Thus the SNR of APD and PMT light sensors is comparable.

When the avalanche is generated by electrons $\alpha \gg \beta$, the ENF can be given by [McIntyre1972]

$$F = kM + (2 - \frac{1}{M})(1 - k). \tag{2.8}$$

The excess noise factor increases with the gain and is dependent on ionisation coefficient k. For gain $M > 10$, expression 2.8 reduces to $F \approx 2 + kM$. If hole multiplication is absent $\beta = 0$, then $k = 0$ and then, based on equation 2.8, $F = 1$ for unity gain $M = 1$. Theoretical limit for higher gains is $F \approx 2$. When β is present, the element kM appears. For a stable avalanche multiplication it is essential that only one type of charges is multiplied, the other type being merely collected. In silicon the difference between the mobility of e and h is small, and the field necessary to start electron multiplication is very close to the field where hole multiplication starts. For PMTs the factor F is typically around 1.2, mainly depending on the gain of the dynodes.

Equivalent noise charge

The signal to noise ratio (SNR) is dependent on the output signal and on both characteristics of APD and preamplifier, given by noise signal:

$$\text{SNR} = \frac{\text{Output signal}}{\text{Noise signal}}. \tag{2.9}$$

The energy resolution on the level of APD is limited by three factors. The first is caused by fluctuation in primary $e - h$ pairs production. The second arises from non uniformity of avalanche process (see §.2.2.2). The last one comes from preamplifier system noise. For short light pulses illuminating the APD surface the root mean square error (RMSE) σ_{tot}^2 on the pulse height can be given by

$$\sigma_{\text{tot}}^2 = \sigma_{el}^2 + \sigma_{stat}^2. \tag{2.10}$$

First element consist statistical fluctuation in pulse height given by Eq. 2.7. The quantity σ_{el}^2 is the electronic noise, generated by both amplifier and the APD. It is very common to express the electronic noise as the *equivalent noise charge* (ENC). It is defined as the charge which should be created in the conversion zone of the APD to produce a pulse of amplitude equal to the RMS of the output noise. Therefore

$$\sigma_{\text{el}} = M\frac{\text{ENC}}{q_e} \tag{2.11}$$

The ENC refered to the input of the APD can be given by [Chen1999]:

$$\text{ENC}^2 = 2q_e[FI_{\text{db}}]\tau a_1 + 2q_e\left[\frac{I_{\text{ds}}}{M^2}\right]\tau a_1 + \frac{1}{M^2}\frac{2}{3}4k_BT\left[\frac{(C_d + C_t)^2}{g_m}\right]\frac{1}{\tau}a_2, \tag{2.12}$$

with q_e electron charge, I_{db} bulk dark current, I_{ds} surface dark current, F excess noise factor, τ shaping time, k_B Boltzmann's constant, T absolute temperature, M APD gain, C_d, C_t detector capacitance and the gate to source capacitance of the first transistor of the preamplifier, g_m transconductance of the preamplifier. Coefficients a_1 and a_2 are dimensionless quantities dependent on the impulse response function and shaping time. They are of order unity for commonly used shaping functions. The first two element of Eq. 2.12 refers to the dark current which is modelled as in Eq. 2.4. The second element, from the surface dark current is usually negligible, because it is much smaller then I_{db} at higher gains. The last part of Eq. 2.12 depends on both characteristics APD (e.g. gain) and amplifier (e.g. capacitances). Detailed calculation of Eq. 2.12 can be found in appendix to [Fremout2002a]. The SNR expressed with ENC basing on equations 2.10 to 2.11 can be written [Fremout2002a]

$$\mathrm{SNR} = \frac{N}{\sqrt{\mathrm{ENC}^2 + FN}}. \tag{2.13}$$

Table 2.2: *Light converters main characteristics [Arisaka2010, Xie2006].*

	PMT	APD	SiPMT	Ideal
QE	25-30%	60-80%	∼100%	100%
F	1-1.3	2	1.1-1.3	1
Gain	10^6	$10^2 - 10^3$	$10^5 - 10^7$	
Power voltage	800-2000V	100-1000V	20-200 V	
Timing	$300\,\mathrm{ps}$	$1\,\mathrm{ns}$	$50 - 200\,\mathrm{ps}$	
λrange	$390 - 410\,\mathrm{nm}$	$400 - 800\,\mathrm{nm}$	$400 - 550\,\mathrm{nm}$	
Magnetic field	sensitive	not sensitive	not sensitive	not sensitive
Temp. dependency	slightly	very big	very big	independent
HV	dependent	dependent	dependent	independent
Preamplifier	not required	required	not required	not required
Compactness	no	yes	yes	yes

Geiger-mode APD, Silicon Photomultiplier

APDs are usually operated in a linear mode, where the signal is proportional to the number of photons detected. Due to the limited internal gain it is so far not possible to detect single photon signals. Nevertheless APDs can also operate as a single photon counters, based on single pixel Geiger-mode silicon avalanche diode (Single Photon Avalanche Diode - SPAD) at operational bias voltage V_{bias} of $10 - 20\%$ above the breakdown voltage $V_{\mathrm{breakdown}}$. SPAD is actually a digital single photon counter with a size of $20 - 200\,\mu\mathrm{m}$. Silicon Photomultiplier (SiPM) is an array of small ($\sim 20 - 30\,\mu\mathrm{m}$), individual SPADs as pixels (also called cells or micro cells), with density of $100 - 10000\,\mathrm{cells/mm^2}$ [Buzhan2006, Dolgoshein2006, Renker2002]. SiPM was first developed in Russia [Gasanov1990, Golovin1989, Golovin1989a], quite fast found to be interesting detector solution [Saveliev2000, Akindinov1997, Antich1997] and be improved
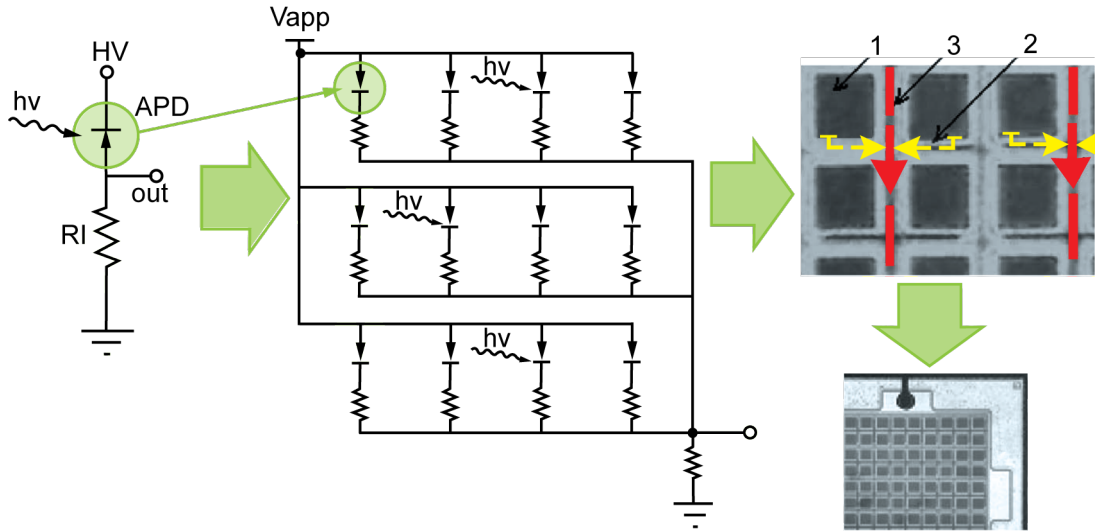
Figure 2.9: *SiPM scheme. left.) electronics, right.) structure [Sadygov2006, Ziemons2009].*

[Bondarenko2000]. Since that time several designs were presented [Sadygov2006]. High interest in this device caused that different institutions use different names for the same product: G-APD – geiger-mode APD [Renker2007, Britvitch2007], LGP – limited Geiger-mode microcell silicon phtomultiplier [Bondarenko2000], MAPD – micro-pixel/channel avalanche photodiode [Sadygov2006], MPGM APD – multi-pixel Geiger-mode APD [Musienko2007], MRS APD – metal resistor structure APD [Saveliev2000, Antich1997, Akindinov1997], and as in this work SiPM – silicon photomultiplier [McElroy2007, Herbert2007].

mechanism   In principle a photon impinging on a one of the pixels can create free carriers that give rise to a Geiger-type discharge. All pixels are connected in parallel to the bias voltage via individual, integrated quenching resistor (Fig. 2.9). Therefore when the pixels voltage drops below the breakdown level, the discharge is quenched. After a short recovery time, needed for recharging, the pixel is ready to detect the next photon. The SPAD pixels are itself binary devices so the signal from it always has the same shape and amplitude. However whole SiPM becomes an analog device. It is because the discharge currents from all pixels are added on a common load resistor. Thus the output signal A is a sum of the signals from all the pixels firing at the same time A_i [Britvitch2007]

$$A = \sum_i A_i. \tag{2.14}$$

The response of the detector remains linear as long as the number of photons remains much smaller then the number of cells. Detailed SiPM working mechanism is described in [Sadygov2006].

characteristics   SiPM as a detector device for nuclear medicine has several really important advantages in comparison to the most popular PMT and APD. It has very compact size that can be easier used especially in multimodalities solutions. The required bias voltage is $20-200V$, that is much less then PMT and APD. The gain can reach $10^5 - 10^7$ as high as PMT. Therefore there is no need for a low noise preamplifier as in APD. The Geiger signal from one pixel is determined by the pixel charge

accumulated in the pixel capacitance C

$$A_i(T) \sim C\Delta V(T) = C(V_{bias} - V_{breakdown}(T)). \qquad (2.15)$$

The single pixel gain increases linearly with overvoltage ΔV, not exponentially as in case of APD. Excess noise factor is low, around 1.1 and increases slightly for higher gains [Guschin2006, Swain2005]. Like other silicon-based photodetectors SiPM has high QE, typically 100% and it is wavelength λ dependent. From the other hand photon detection efficiency PDE (typically $\sim 40 - 50\%$) is lower then QE, because

$$\mathrm{PDE}(\lambda) = \mathrm{QE}(\lambda)\varepsilon_{\mathrm{Geiger}}\varepsilon_{\mathrm{geometry}}, \qquad (2.16)$$

where $\varepsilon_{\mathrm{Geiger}}$ is the probability for a Geiger discharge initialization by a carrier created in active pixel volume, that means firing the pixel; $\varepsilon_{\mathrm{geometry}}$ is a fraction of the total SiPM area that is occupied by an active pixels, given by packing fraction. One more factor affecting the PDE is the recovery time. The efficiency $\varepsilon_{\mathrm{Geiger}}$ is overvoltage dependent. SiPM response signal to a given light pulse depends on PDE and pixel gain. Considering that both of these parameters are dependent on overvoltage $\Delta V(T)$ (Eq. 2.15), therefore SiPM is sensitive for temperature and bias voltage fluctuation. The SiPM has intrinsically very fast recovery time (less then $500\,\mathrm{ps}$) due to the very thin depletion layer and the extremely short duration of the Geiger discharge development [Dolgoshein2006]. SiPM is robust and insensitive for a magnetic field and ionization radiation (as APD), so doesn't need any sophisticated shielding and can be applied for widely investigated nowadays PET/MRI dual-modality. Predicted costs of mass production should be relatively small because it uses standard Metal-Oxide-Silicon (MOS) process. The disadvantage of SiPM is that, for the number of photoelectrons PDE·$N_{photons}$ is close to the total number of pixels $N_{total\#ofpixels}$, nonlinearity of the SiPM response appears. That can lead to output signal saturation.

$$N_{firedpixels} = N_{total\#ofpixels}(1 - e^{-\mathrm{PDE}\frac{N_{photons}}{N_{total\#ofcells}}}) \qquad (2.17)$$

Electronic noise is negligible and the main source of noise in a SiPM is due to dark rate. It comes from charge carriers thermally created in the sensitive volume. The SiPM dark rate increases with temperature from a few ($\sim 1 - 2$) MHz/ mm^2 (at room temperature) to ~ 200 MHz/ mm^2 (at 100 K)[Dolgoshein2006]. It causes problem with detection of small light signals (up to a few photoelectrons). Another problem in SiPM operation is inter-pixel crosstalk. Each pixel should work as independent photon micro-counter. Electrical decoupling is realized by two elements. Quenching resistors for each pixel, which limit the Geiger discharge and at the same time electrically decouple pixel from pixel. Second, by specially designed boundaries between pixels in order to inhibit inter-pixel currents in the silicon itself. Since these boundaries occupy part of the SiPM surface, it reduce the sensitive area and thus geometrical efficiency. Another type of inter-pixel coupling is introduced by optical crosstalk. It originates from photons created in the Geiger discharge ($\sim 10^{-5}$ photons per electron). These photons can propagate to another not primarily fired pixel and initiate a discharge there. Optical crosstalk violates the pixel independence.

SiPMs are a new and promising type of detectors, because they combine the advantages PMTs and APDs. Many groups are testing this device, but no com-

mercial PET systems based on SiPMs are available yet. Probably it is only the matter of time.

3
Setup description

This chapter explains the advantages of the monolithic scintillator block based APD design and the details of the aim of the project. The detector setup structure and signal processing is described. The artificial neural network algorithm is explained.

3.1   Competitiveness of monolithic block idea

Research on PET hardware developments mainly concentrates on improving the sensitivity and the spatial resolution. The detection of gamma rays in nearly all commercial PET scanners is based on the use of block detectors with a large number of small scintillator pixels (Fig. 3.1) [Lewellen2008, Muehllehner2006]. Diminishing the dimensions of the crystal pixel improves the spatial resolution. However, there are serious drawbacks to this approach, such as the detector module complexity and costs of production. Smaller scintillator pixels lead to a lower packing fraction, thus reduce sensitivity. Another important factor limiting the
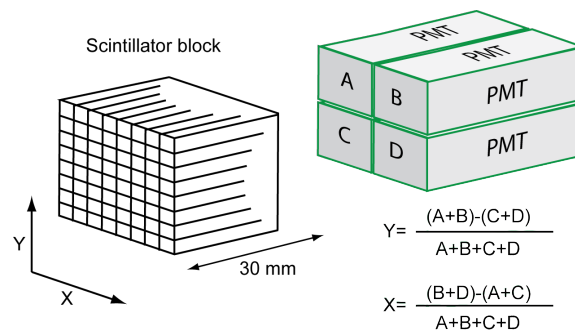

Figure 3.1: *Typical scheme of a pixilated detector design. The pixelated crystal mounted on four PMTs. Position coordinates X and Y calculated from light share.*
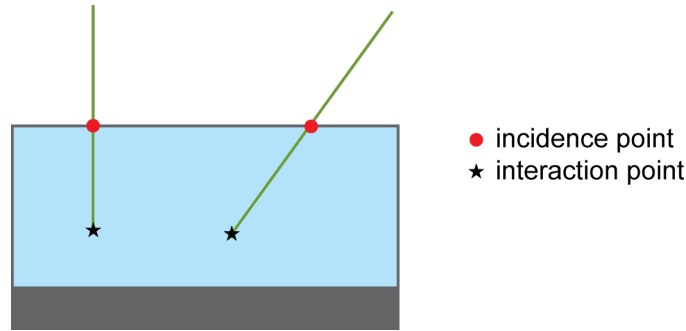
Figure 3.2: *The difference between incidence and interaction point.*

spatial resolution in case of a pixelated detector is the uncertainty of the exact DOI information in the crystal. As a result, the spatial resolution, for a given tracer dose and scanning time is damaged. Therefore to keep a reasonable image quality together with improved spatial resolution, the sensitivity needs to be increased. In case of a pixelated detector design, this is challenging, because the square signal-to-noise ration in image quality is is inversely proportional to the fourth power of the image pixel size. When the image resolution is improved by a factor of 2, one needs 16 times more coincidence events to keep constant image quality [Bruyndonckx2007a]

Using one large and undivided piece of a scintillator, where the position of the gamma interaction is extracted in a continuous way from the light distribution in the block, allows to overcome the referred limitations. The sensitivity of the scanner is increased by avoiding inter-crystal dead spaces (see §.1.4.2). Moreover using a trapezoidal shape rather then cuboid, further diminish the volume gap [Laan2009, Maas2008]. Next, due to lower interior reflection on the crystal sides, the light output increases and hence also enhances the energy resolution. For the monolithic block it can be pushed to around 15%, where for the pixelated design is usually around 20% [vanEijk2002].

To diminish the degrading influence of the parallax effect (see §.1.4.1), the DOI should be known. Uncertainty of the DOI results in uncertainty of interaction point. Thus the spatial resolution degrades. With the help of the neural networks (see §.3.3) it is possible directly to determine the incidence point without determine the DOI [Tavernier2005]. The proposed monolithic block detector design used with a neural network algorithm determines the photon incidence position on the surface of scintillation crystal instead of the interaction point (Fig. 3.2). Thus there is no need for separate DOI calibrations. With the dramatic increase of computing power in recent years, this is now a realistic approach to real-time gamma detection in PET scanners.

As a scintillation crystal LSO was chosen, because it has one of the best characteristics for a PET applications. As a photo sensor, APD is used, as an alternative to PMT. Generally, a PMT in most of cases has better performance, so that in standard PET applications, PMTs are still more common. Nevertheless, considering multimodality solutions as a new generation of medical imaging techniques, PMTs fail for PET/MRI dual modality. In case of the PET coupled to MRI, the main reason is that the detector are exposed to intense magnetic fields. This excludes the use of PMTs. Another advantage of the photodiode is its compactness, that diminishes dead spaces between the detector modules in the PET ring and
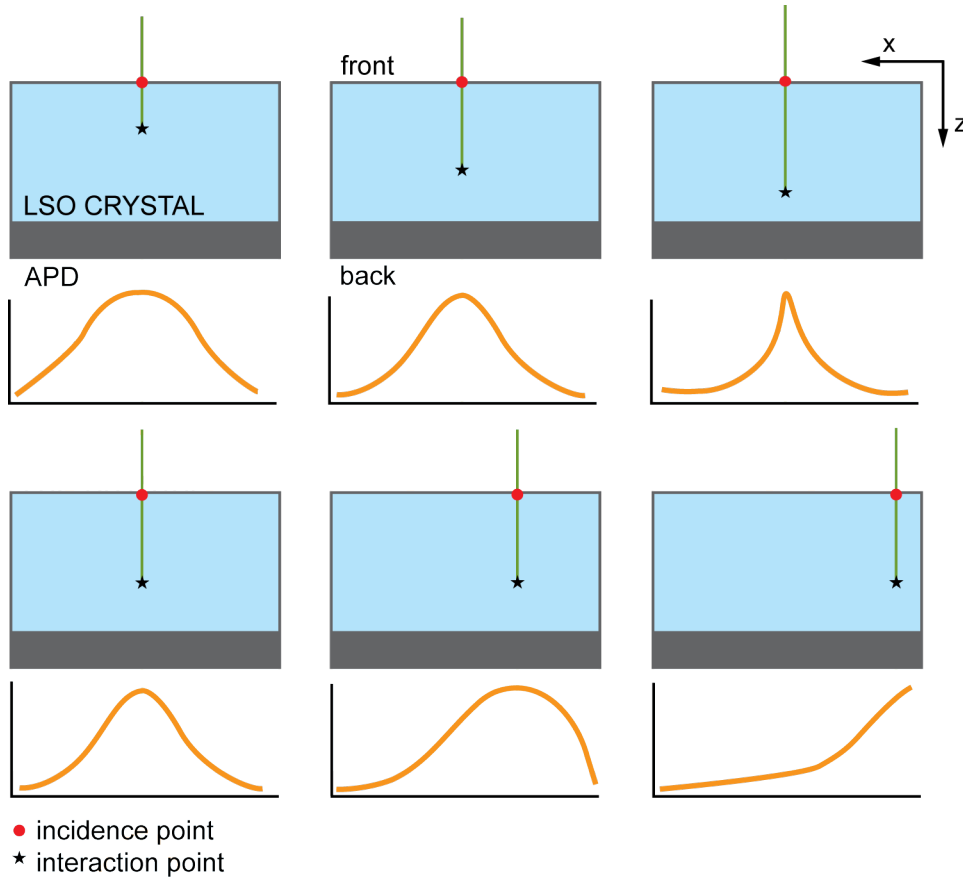
Figure 3.3: *Examples of light distribution as a function of interaction (top row) and incidence (bottom row) position.*

the gantry itself. As of today the APD is the best choice for a photodetector in PET, that is compatible with strong magnetic fields. It is possible that in a near future SiPMs will be improved to the point where this is a better solution.

Until now, several monolithic block detectors were investigated [Lerche2009, Lemaitre2009, Laan2009, Maas2008, Leonard2005]. The block presented in this work has an enlarged volume in comparison to these, already studied designs. The advantages are that it reduces dead space between detector crystals even more and diminishes the crystal edge surface reflection effects. One of the aims of this project is to check how the increased size of the block influences the spatial resolution.

3.2 Setup design

The goal of this work is to test a new version of the monolithic block design concept as a PET detector and to compare the results to previously published. The framework of this thesis contains building the prototype of the detector setup, then put it into operation and investigate the acquired results. The setup is run to collect data in order to analyse spatial resolution reconstruction algorithm robustness to several important parameters, such as incidence gamma beam angle, temperature and high voltage supply fluctuations. The setup is controlled by a program written in *LabView* from *National Instruments^{TM}* [LabView]. All data analysis, function fits and spatial resolution reconstruction processes are done in
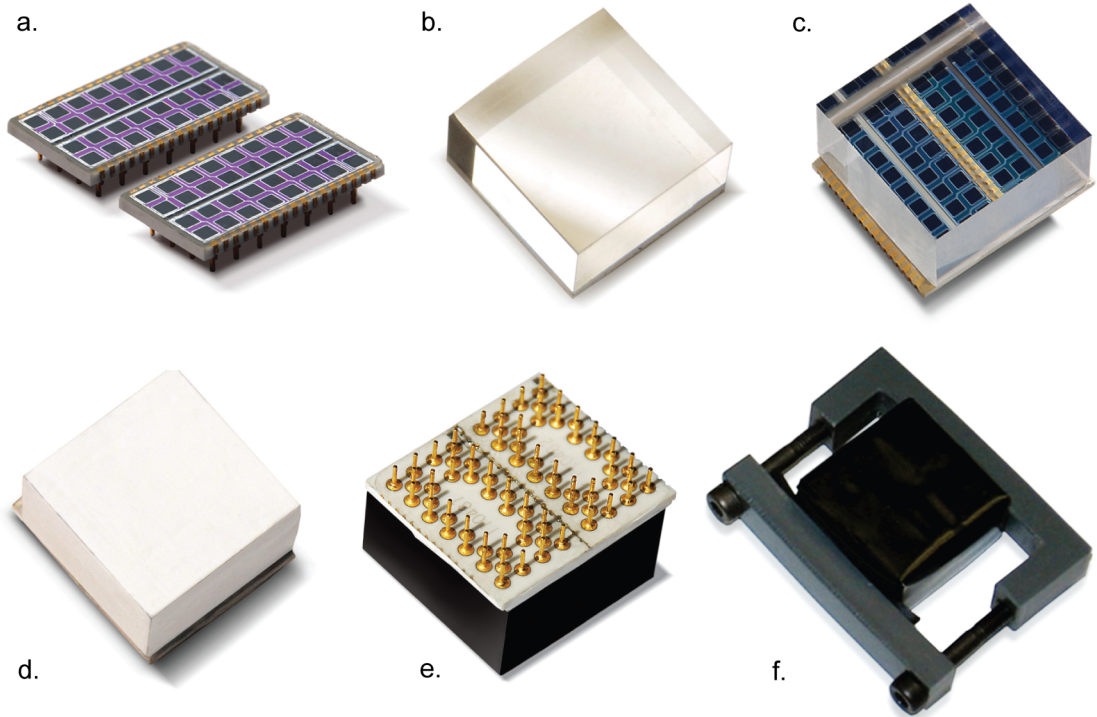
Figure 3.4: *The detector module photos: a). Hamamatsu S8550 APDs, b). monolithic* $20 \times 20 \times 10\,\text{mm}^3$ *LSO crystal, c). the crystal mounted on two APDs, d). wrapped in Teflon tape, e). wrapped in black tape, f). to avoid crystal sliding placed in a plastic shaper.*

$Mathematica^{TM}$ with extension of the package *Neural Networks* [Wolfram].

3.2.1 Front-end detector

The gamma detector is a $20 \times 20 \times 10\,\text{mm}^3$ polished monolithic block of LSO. Five sides of the block are wrapped in Teflon tape [Teflon] (Fig. 3.4.d) to increase reflectivity on the crystal edges and enhancing light output [Leonard2005, Fremout2002].

The sixth side of the crystal ($20 \times 20\,\text{mm}^2$) is coupled to two Hamamatsu S8550 APD [Hamamatsu2006] (Table 3.1). This APD array consists of 4×8 pixels, each with an active surface size of $1.6 \times 1.6\,\text{mm}^2$ (Fig. 3.5). Two monolithic silicon wafers, each of them comprising 16 APD pixels, are combined in a single housing. The ceramic carrier plate is $1.0\,\text{mm}$ thin. To protect the APDs, the surface is completely covered with a $0.5\,\text{mm}$ epoxy layer. The common ground and the 32 diode anodes are contacted by a plastic grid array at the back side of the carrier plate [Kapusta2003, Pichler2001]. The S8550 APD has a *reversed type* structure, that is specifically designed to couple with scintillators due to its short wavelength ($< 500\,\text{nm}$) selective operation. Generally it is designed that the depletion layer comprises two regions: on the front part, typically about $5\,\mu\text{m}$ from the surface of the photodiode, a relatively thin *multiplying region* with a field sufficient for impact ionization. And behind the multiplying region, a wider *drift region* of fairly low field adequate for rapid charge collection. Thus the design permits the use of a relatively wide depletion region, which reduces the capacitance per unit

Table 3.1: *Technical characterisation of the S8550 Hamamatsu APD array* [*Hamamatsu2006, Kapusta2003*].

Device size	$218.4\,\mathrm{mm^2}$ $(19.5 \times 11.2\,\mathrm{mm^2})$
Total active area	$81.92\,\mathrm{mm^2}$
Number of pixels	32 (4×8)
Pixel size	$1.6 \times 1.6\,\mathrm{mm^2}$
Pitch	$2.3\,\mathrm{mm}$
Bias voltage range	$100 - 400\,\mathrm{V}$
Operating gain range M	1-100
Spectral response range	$320 - 1000\,\mathrm{nm}$
Quantum efficiency at $420\,\mathrm{nm}$	$60 - 70\%$
Dark current per pixel $(M = 50)$	$10\,\mathrm{nA}$
Terminal capacitance per pixel $(M = 50)$	$10 - 15\,\mathrm{pF}$
Supply voltage	$\pm 2.5\,\mathrm{V}$
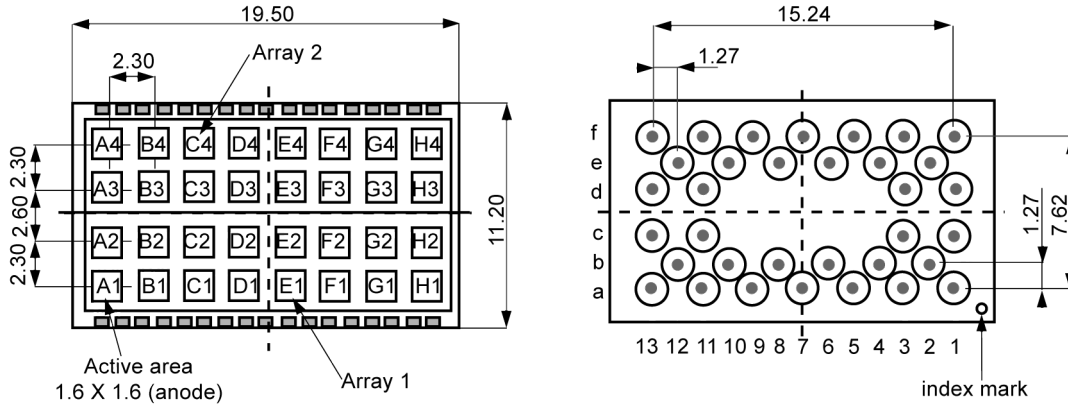
Figure 3.5: *Hamamatsu S8550 APD scheme* [*Hamamatsu2006*].

area, while still permitting operation at quite low bias voltages $(< 500V)$. Since LSO emits at a short wavelength of $\sim 420\,\mathrm{nm}$, most of its light is absorbed within the first $1 - 3\,\mu\mathrm{m}$ of the depletion layer and generates electrons, which undergo full multiplication. Most of the dark current, on the other hand, undergoes only hole multiplication, and so its contribution to the noise is reduced significantly [Kataoka2005, Knoll2000, McIntyre1996]. The biggest disadvantage of an APD is its low internal gain and consequently its low SNR.

To ensure good transfer of light from the scintillator to the APD, the optical glue Meltmount [Meltmount] is used. It has a refractive index of 1.582 (at 25°C), that is in range between the LSO 1.82 and the APD epoxy layer ~ 1.53. Thus the probability of internal reflections at the exit surface is diminished. Meltmount is rather a very viscous liquid and doesn't provide permanent coupling. Therefore after some time, the crystal slips down from the APDs. To ensure a stable geometry, the detector module is placed in a special holder made from plastic material (Fig. 3.4.f). To protect the Teflon layer from the plastic holder it is covered with black tape before mounting in the holder. The resulting detector element is called a front-end *detector module*.
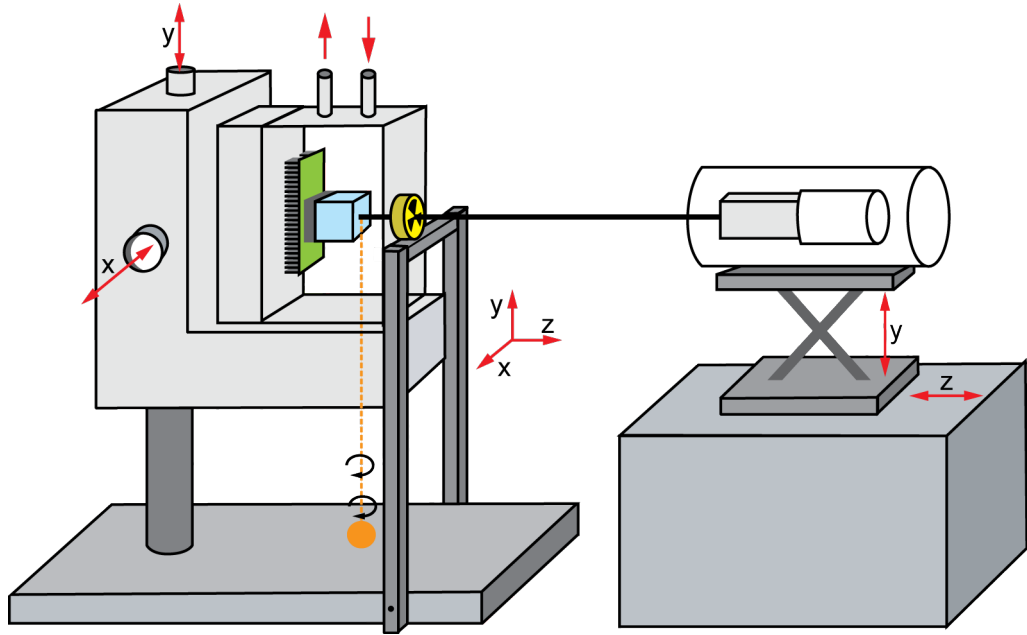
45

Figure 3.6: *Scheme of the bench setup.*

3.2.2 Bench setup with read-out electronics

The aim of the setup is to test machine learning algorithms as a method to determine the gamma incidence point in the scintillator. The reconstruction process (see §.3.3) requires measurements of light distributions for known beam positions along the crystal at different photon beam angles. To this end, a bench setup is built.

The front-end part, i.e. the detector module equipped with 64 APD pixel outputs is placed into the socket of PCB - manufactured in CIEMAT, Madrid (Fig. 3.8). Each APD pixel is equipped with its individual readout chain consisting of a Cremat front-end preamplifier (Table 3.2), a CAEN N568B spectroscopic amplifier channel (Table 3.2), and a CAEN V785 peak sensing ADC channel (Table 3.2). The detector module and the PCB with the 64 Cremat preamplifiers are mounted in a light tight, aluminium box. In the reminder of this text, this box will be referred to as *the detector box*. To keep the detector module at a constant temperature, the box is cooled to $17 - 19°C$ by a flow of cold liquid from a Huber cooling unit [Huber]. The cooling pipe is mounted against the back side of the box and the box itself is isolated by a layer of isolating foam (Fig. 3.9). To protect the electronics from the risk of condensation, the box is flushed with dry air. For further protection a container with silica gel blue (from Fluka cat.no. 85342) is
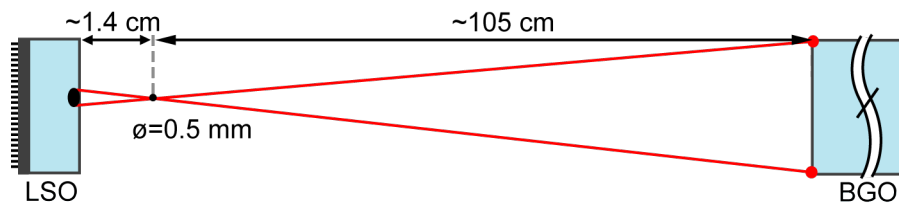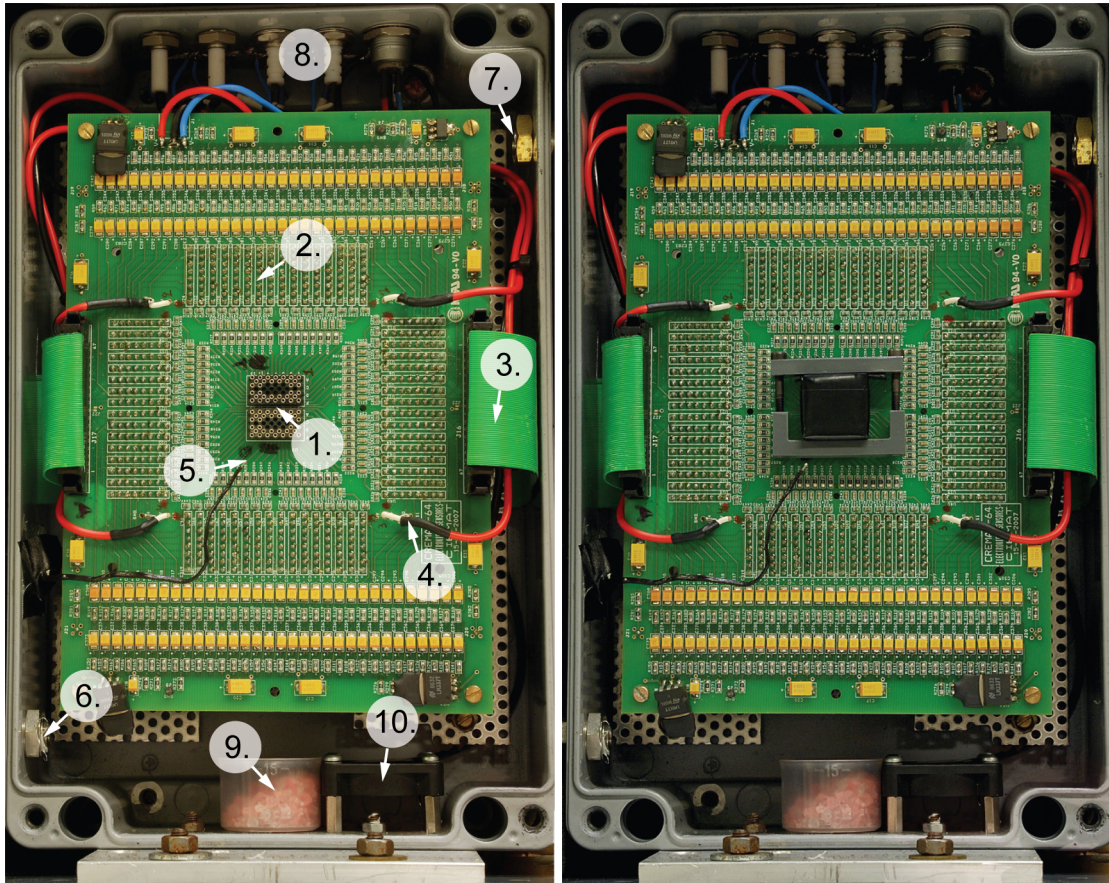

Figure 3.7: *Scheme of the theoretical beam size estimation provided by the geometrical detector arrangement (not to scale).*

1. APD socket
2. Socket for a Cremat
3. 32 channels output
4. Single APD subarray power supply
5. Temperature sensor

6. Dry air flow input
7. Dry air flow output
8. Power connectors
9. Silica gel conainer
10. Fan

Figure 3.8: *The detector box: left) inside of the detector box, the CREMAT pream-plifiers are plugged in from the bottom side of the printed circuit board, right) the same box also without face cover, but with mounted the detector module.*

placed inside the box.

The detector box is placed on a $1\,\mu$m precision computer controlled $XY\Omega$ stage [Platform], allowing to scan the whole surface of the detector. The detector box can be rotated over an angle Ω around a vertical axis going approximately through the centre of the detector (Fig. 3.6).

Beam size estimation

As an annihilation photon emitter, $\varnothing0.5\,$mm ^{22}Na is used. At the time of the measurements its activity was $12-15\,\mu$Ci. The source is mounted in front of the box ($1.2-1.6\,$cm away from the crystal surface) in a holder with adjustable xyz position (Fig. 3.9). The source holder is fixed on the rotating platform, thus the source rotates together with the detector box (the reason why, is explained later during results analysis, Fig. 4.3). The reference detector is a $20\times20\times50\,$mm^3 BGO crystal coupled on a XP2020 PMT [Photonis] by optical grease
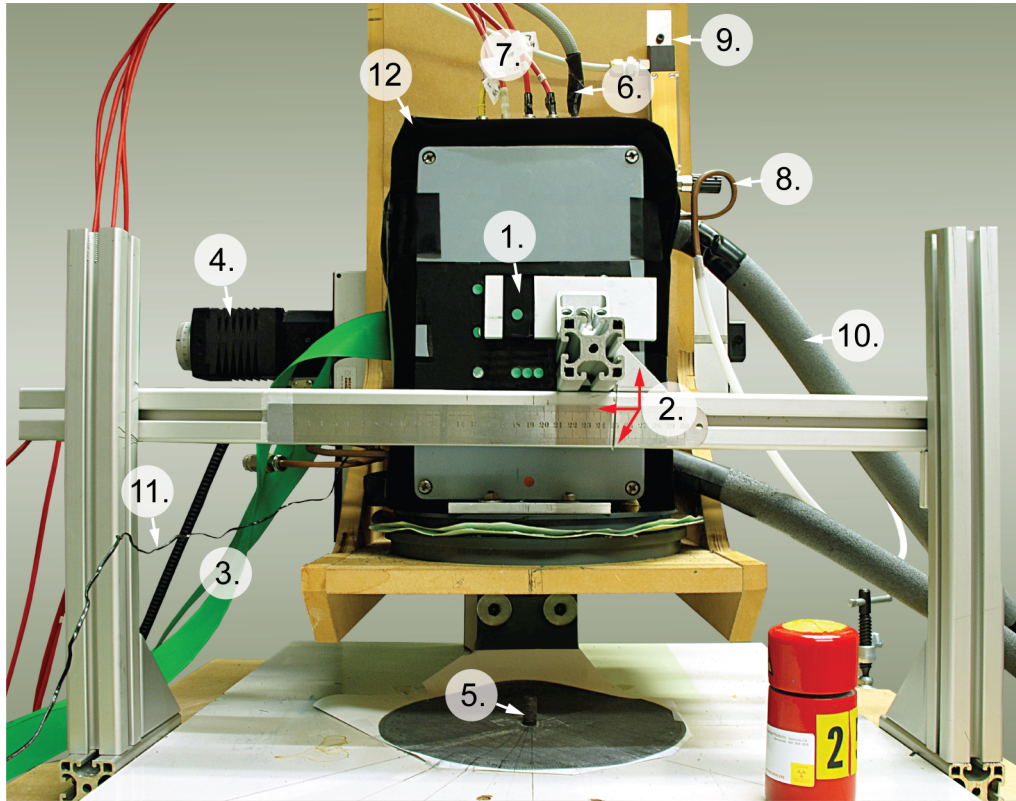
1. Sodium source
2. Source holder
3. 2x32 channel signal flat cable
4. Horizontal stepping motor
5. Center of rotation
6. PCB power cable

7. APD power cables
8. Dry air flow output
9. Dry air bubbler
10. Cold licquid pipes
11. Temperature sensor cable
12. Isolating foam

Figure 3.9: *Front view to the detector box with source on the adjustable holder.*

[DowCorning]. This module is placed 110 ± 3 cm from the source (measured from the surface of BGO). Although this geometric arrangement should provide beam of a 0.76 mm (Fig. 3.7), in fact the beam is wider. Several effects contribute to the beam size impinging on the detector: dimension of the reference crystal, dimension of the source, positron range in the source and gamma non-collinearity. Therefore the size of annihilation photons beam is estimated empirically by a fitting sigmoid function to a coincidence count rate plot as a function of the beam position [Lemaitre2009, Maas2008]. Data were obtained from measurement, when the beam is moved (10 mm) over the edge of the crystal, with a $250 \, \mu$m step. The obtained sigmoid count rate profile is the result of a convolution between the photon beam profile and a step function representing the edge of the LSO block. Assuming that the photon beam can be described by a Gaussian function, the measured count rate profile is fitted with

$$\int_{-m/2}^{\infty} A e^{-\frac{1}{2}\left(\frac{x-y}{\sigma}\right)^2} dy \tag{3.1}$$

where m is size of the block, σ the width of the photon beam, and A a scaling factor. The fitting is done in *Mathemetica*. Because of the background events in

the measurement, a constant term B is added to the fit function. Estimated in such way beam width equals 1.09 ± 0.06 mm FWHM 511 keV in x and y direction along the crystal (Fig. 3.10). The evaluated beam size depends on the range of the data chosen for fitting and the number of collected data (due to better statistics for higher number of events). It is observed that for separated measurements the evaluated beam changes from 0.1 to maximum 0.2 mm.
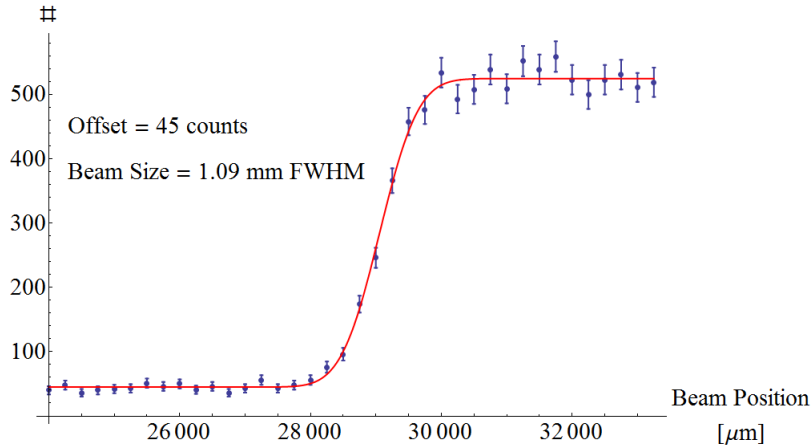

Figure 3.10: *Beam size estimation. Sigmoid fit (- red solid) to the count rate plot (- blue points) at the edge of the crystal. Scanning step 0.25 mm.*

The ADC trigger signal

The general readout chain is described in the first part of §3.2.2. However, a specific triggering circuit is employed to select coincidence events from the all incoming pulses. This needs more careful explanation.

The CAEN N568B amplifier is equipped in three types of outputs: OUT (only internal amplification, $100\,\Omega$ impedance, dynamic range ± 8 V max - 1 MΩ load), xOUT (further 10x fixed amplification of the OUT value, $100\,\Omega$ impedance, dynamic range ± 4 V max into $100\,\Omega$ load) and FOUT (fast output, $100\,\Omega$ impedance, 100 ns differentiation time constant, ± 4 V max into $100\,\Omega$ load, rise time typically 25 ns, gain factor approximately 20 to 30).

The coincidence readout uses xOUT to increase the gain. The signal is sent to the CAEN V785 peak sensing ADC, that exports signal to the PC. The exporting process is controlled by the CAEN VME bridge V1718 [CAENvme]. The programs to read, form and save the data, to control the VME bridge and also the XYΩ moving platform are written in LabView. The coincidences are triggered in the ADC by a parallel circuit (Fig. 3.11). This circuit determines the electronic coincidence between the APD and the PMT single signal rates.

The coincidence trigger employs the FOUT signal from the CAEN N568B amplifier, as the APD part of coincidence. It is generated faster than normal OUT. The ADC requires the triggering gate-to-peak delay of at least 250 ns and the FOUT fulfils this condition. 64 APD signals are summed by the home made analogue 32 channels summing modules and then by two channels summing module (LeCroy).

Both signals, from APD and PMT are discriminated (by LRS mod6201 or CAEN mod96 discriminators). The threshold level is determined from the pulse
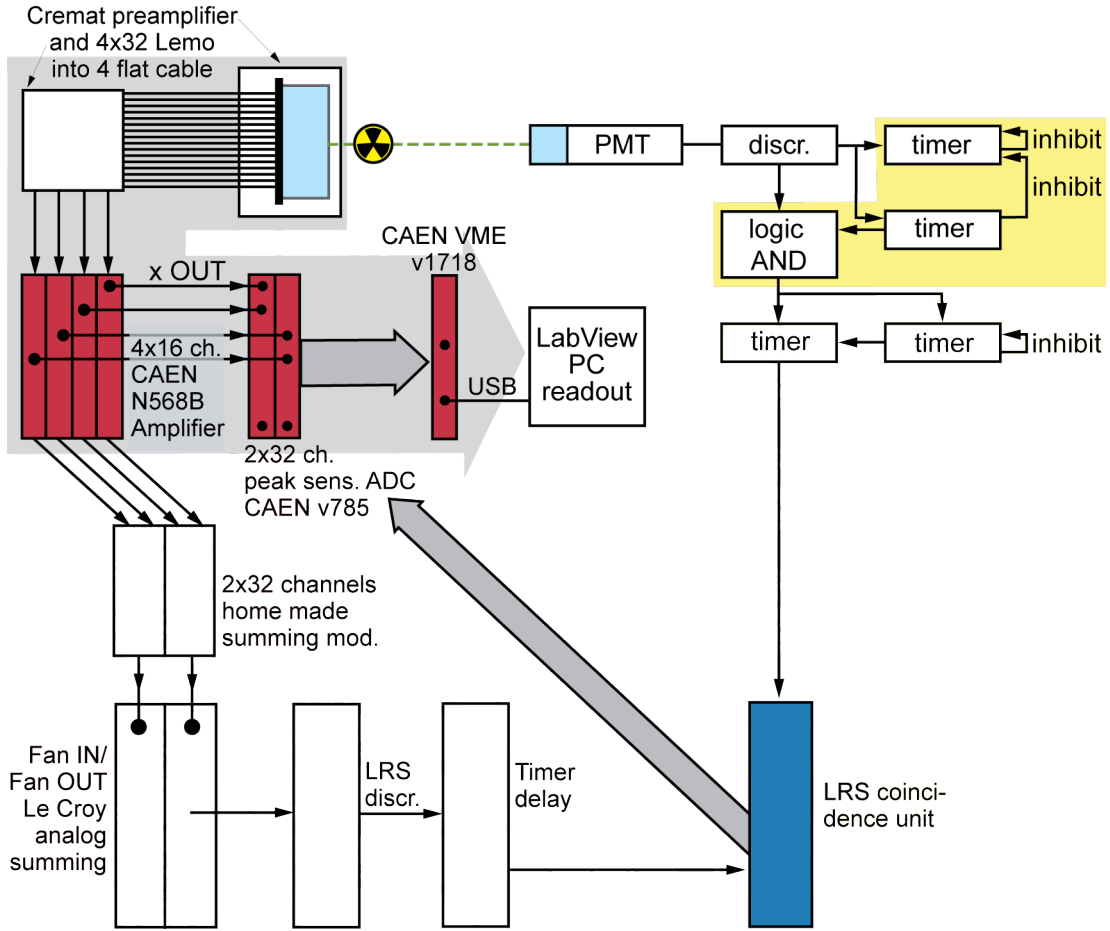
Figure 3.11: *Scheme of the experimental setup.*

spectrum analysis obtained with help of Tektronix TDS 5104 digital oscilloscope. The same oscilloscope is used to observe the time shift between both signals. That help to optimise the delay and the width of the coincidence signals (it is set for approximately 35 ns each). The logic AND is performed in the coincidence unit (LRS mod.622C). The coincidence time window is $\Delta\tau = 75$ ns. The ADC triggering gate set by the coincidence unit equals around $1.2\,\mu$s.

The PMT signal requires a additive small logic circuit to avoid single electron peaks and after-pulsing (see §.2.2.1). This is done with use of timers (CAEN mod2255B) and logic unit(LRS mod.622C).

3.3 Artificial neural networks - a positioning algorithm

The scintillator based PET detector can be described as a non-linear system, that encodes an annihilation photon beam position coordinates into a light distribution, which is converted to a detector response by the APD. A mathematical algorithm, to find the photon position has to work in the opposite direction. It is used to extract the information from the scintillation light distribution, i.e. from the set of APD outputs. One of the possibilities, proposed by [Clement1998, Delorme1996] for application in PET, is *the artificial neural networks* (ANN) algorithm. Its design is motivated by analogy with the neural structure in brain, which is a living proof that it is a fast and powerful tool. Investigations showed the ANN approach

Table 3.2: *Main specifications of Cremat preamplifier type CR-110 [Cremat2006] (assuming temperature 20°C and $V_s = \pm 6.1V$, unloaded output), CAEN N568B spectroscopic amplifier [CAENamp], CAEN V785 peak sensing ADC [CAENadc] and CAEN VME V1718 [CAENvme].*

Cremat CR-110		
RMS ENC	200	electrons
Gain	1.4	V/pC
Decay time constant	140	μs
Maximum charge detectable per event	1.3×10^7	electrons
Power supply voltage (V_s)		
maximum	± 13	V
minimum	± 6	V
Operating temperature	-40 to +85	°C
Output offset	+0.2 to -0.2	V
Output impedance	50	Ω
CAEN Amplifier 568B		
design	16 channels/module	
Coarse gain/Fine gain	6/0	
Operation gain	~ 38	
Input risetime	10	μs
Shaping time	0.2	μs
Offset	Constant for all channels	
CAEN ADC V785		
design	32 channels/module	
resolution	12-bit	
Conversion time	$5.7\,\mu$s/$32ch$	
Event buffer memory	32	
Fast clear time	600 ns	
CAEN VME V1718		
Up to 30MByte/s sustained data transfer rate		
Data width:	D8, D16, D32, D64	

is competitive due to its fast data processing and efficiency [Tavernier2005].

3.3.1 From the universal approximation to the MLP network

The problem to extract the position from the measured light distribution can be viewed as a regression problem where a function needs to be constructed which maps the vector **x** containing a set of APD responses onto an incidence position coordinate y, i.e., $F(\mathbf{x}) = y$. Therefore finding a detection algorithm can be viewed as a function approximation problem.

Let $f : R^{\mathcal{N}} \to R$ ($\mathcal{N}$ is the number of length distibution samples) be the function mapping the vectors $\mathbf{x}^k$ onto impact positions y^k. The superscript $k = (1, \ldots, n)$ denotes a particular event in the data set, in total containing n events. A desired function is $F\left(\mathbf{x}^k\right)$, a parametric estimator of f whose parameters are chosen such as to minimize the

RMSE:

$$\sum_{k=1}^{n} \left(y^k - F\left(\mathbf{x}^k\right) \right)^2 \tag{3.2}$$

To find such an estimator *the universal approximation* theorem [Haykin1999] can be applied:

Let $\phi(\cdot)$ be a nonconstant, bounded and monotonically increasing continuous function. Let $D^{\mathcal{N}}$ denote the $\mathcal{N}$-dimensional unit hypercube $[0,1]^{\mathcal{N}}$. Then, given any function f defined on $D^{\mathcal{N}}$ and $\varepsilon > 0$, there exist an integer M and sets of real constants α_i, b_i and w_{ij} where $i = (1, \ldots, M)$ and $j = (1, \ldots, N)$ such that we can define

$$F\left(\mathbf{x}\right) = \sum_{i=1}^{M} \alpha_i \phi \left(\sum_{j=1}^{N} w_{ij} x_j + b_i \right) \tag{3.3}$$

as approximation of $f\left(\cdot\right)$, i.e.

$$\left| F\left(\mathbf{x}\right) - f\left(\mathbf{x}\right) \right| < \varepsilon \tag{3.4}$$

for all $\mathbf{x} = (x_1, x_2, \ldots, x_N)$ in the input space.

MLP Finding the set of parameters $\mathbf{W}$, $\mathbf{b}$, $\mathbf{v}$ can be done by using an ANN. The abilities of ANN are acquired due to the interconnected structure of individual simple processing units called *neurons*. The processing ability of the network is stored in the inter-unit connections strengths called *synaptic weights w*. These weights are obtained from a set of training patterns.

The most classical network architecture is the *multilayer perceptron network* (MLP) where neurons are arranged in layers: one input layer, one or more hidden layer(s) and one output layer. The input layer receives all input values in parallel which are then passed to connected neurons of subsequent hidden layers via weighted connection. One neuron from a layer is fully connected to each neuron of the next layer. A hidden neuron performs a non-linear transformation of the biased sum of its inputs by using an *activation function ϕ* and passes the transformed value to neurons of subsequent layers. Finally, the transformed values are passed to the linear output neurons [Leonard2005, Bruyndonckx2004].

Hence the universal approximator F can be implemented as an ANN with N input nodes and a hidden layer with M neurons. The link connecting the jth input node with the ith hidden nodes is given by w_{ij}, whereas the bias of the ith hidden node is represented by b_i. The link connecting the ith hidden nodes with the output node, later in this work denoted as $\hat{y}$, is given by α_i (Fig. 3.12). All parameters w_{ij}, b_i, α_i are represented by the following global parameters, $M \times N$ matrix $\mathbf{W}$, the vector $\mathbf{b}$ $(M \times 1)$ and vector $\mathbf{v}$ $(M \times 1)$.

$$\mathbf{x} = \begin{bmatrix} x_1^k \\ \vdots \\ x_N^k \end{bmatrix}, \mathbf{W} = \begin{bmatrix} w_{11} & \cdots & w_{N1} \\ \vdots & \ddots & \vdots \\ w_{1M} & \cdots & w_{NM} \end{bmatrix}, \mathbf{b} = \begin{bmatrix} b_1 \\ \vdots \\ b_M \end{bmatrix}, \mathbf{v} = \begin{bmatrix} \alpha_1 \\ \vdots \\ \alpha_M \end{bmatrix} \tag{3.5}$$

The output of the ANN is defined by a sum of the hidden layer outputs weighted by α_i and it can be also expressed as:

$$\hat{y}\left(\mathbf{W}, \mathbf{b}, \mathbf{v}\right) = \mathbf{v}^{\text{T}} \phi \left[\mathbf{W}\mathbf{x} + \mathbf{b}\right] \tag{3.6}$$
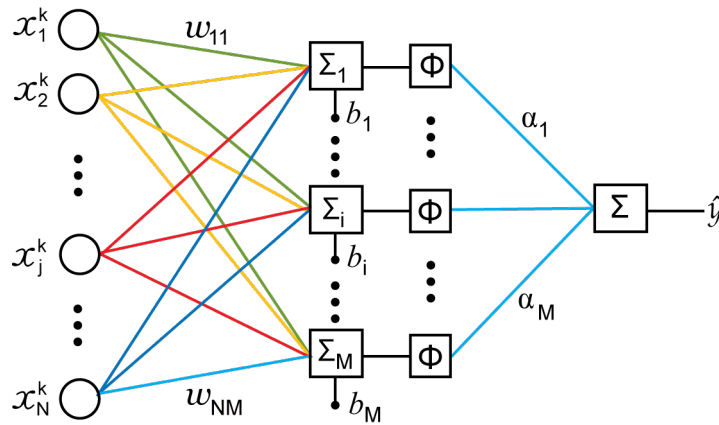
Figure 3.12: *Scheme of multilayer perceptron network with N inputs, one hidden layer with M neurons [Bruyndonckx2006, Haykin1999].*

The transfer function $\phi(x)$ of the neurons in the hidden layer is usually given by sigmoid [Haykin1999]

$$\phi(x) = \frac{1}{1 - e^{-x}}. \tag{3.7}$$

The output layer with one neuron has a linear transfer function. This discussion considers one hidden layer. For more layers equations such 3.3 or 3.6 expand. The structure of the network applied in this work is explained in next three subsections.

The artificial neural networks algorithm has another important advantage, i.e. *learning* the *learning* ability. Before a network will be used for data analysis, it needs to be trained with a set of inputs, called *training data set*, whose outputs are known. This process allows to adjust weights and biases so that the actual outputs conform to the desired outputs.
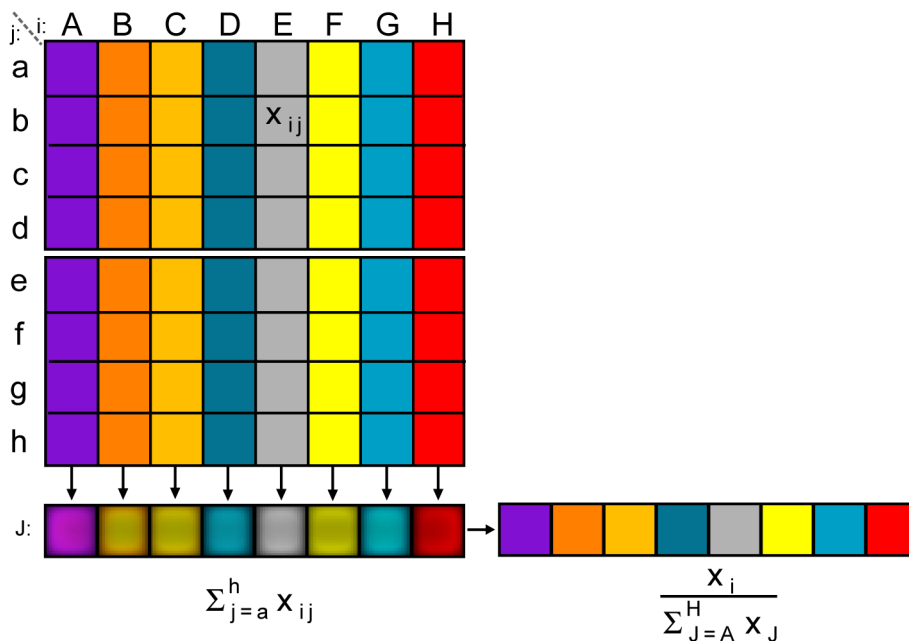

Figure 3.13: *ANN inputs design*

53

3.3.2 The ANN inputs design

Although the answer of trained ANN for a given input is usually immediate, the learning process takes longer. To diminish training time, without losing quality of the final network function, several steps are done. First, the APD responses are processing in such way to diminish the network complexity by reducing the number of neural inputs. For ANN training in the x direction along the crystal, for each event, the pixels of APD are summed in columns (Fig. 3.13), since they have no extra information about the horizontal resolution. In analogy, for an y direction inputs are sums of the rows. It diminishes the number of inputs from 64 APD pixels to 8 pixels sums, i.e. the network inputs $N = 8$. Thus the dimensionality of the problem is reduced and the risk to be caught in a local minimum during training is less.

normalisation   The next step to simplify the problem is to normalise the inputs such that their sum equals one. This can be done, because the light distribution depends on the impact position, not on the energy deposited. Due to this ANN does not use the energy amplitude as an another parameter [LeCun1993].

shuffling   The training data are shuffled before the ANN learning process. Data set is in order of scanned beam positions. If data are trained without shuffling, ANN start training for first beam position and start to specialise for this position. After that data of the next beam position are introduced. The weights have to change such that the NN starts to generalizes to also recognize the second beam. Now the NN could be optimized for beam position 1 and 2. When data of third beam position are given, the NN has to generalize again etc. This problem is avoid by shuffling the network data set and thus the speed of learning is also improved.
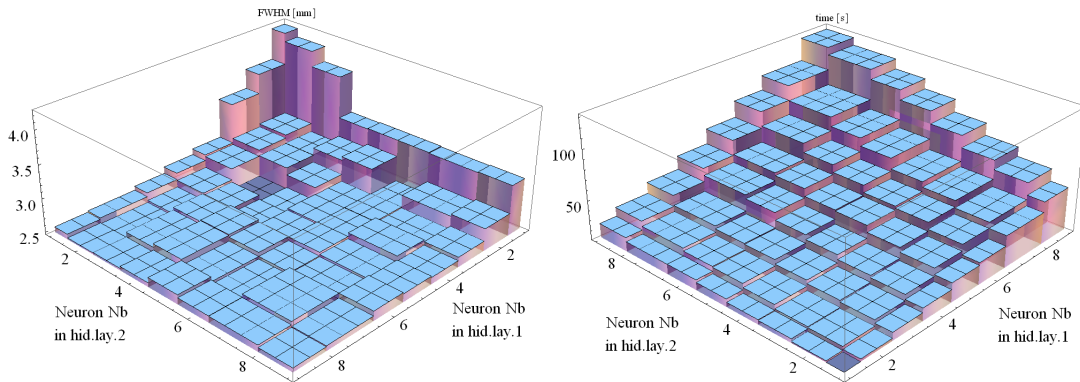
Figure 3.14: *Neuron number calibration. Neuron number in two hidden layers in function of a.) obtained spatial resolution, b.) time of training*

3.3.3 Network structure

The ANN used has eight inputs corresponding to the summed APD signals and a single output representing the incidence position of the photon along the considering horizontal or vertical side of the LSO block. Although the universal approximation theorem states that a single hidden layer ANN is able to model most functions, it does not guarantee that this network structure is the best choice in terms of learning speed and generalization. For a regression problem, it is often useful to have two hidden layers. During the training process, the nodes in the

first hidden layer extract local features of the function to be modelled. The second hidden layer combines the outputs of the first hidden layer to represent more global aspects [Haykin1999]. The number of nodes in the hidden layers is chosen experimentally. In each of the hidden layers, the number of neurons is increased until the resulting spatial resolution saturates (Fig. 3.14.a). A higher number of neurons just prolongs the training time (Fig. 3.14.b). For this study it is decided to use two hidden layers with five neurons each, for all ANNs (Fig. 3.12).

3.3.4 The ANN training, validation and evaluation

The training procedure is an iterative process adjusting the parameters of the *training* network ($\mathbf{W}$,$\mathbf{v}$,$\mathbf{b}$) to minimize the global RMSE between the desired output y_k and the predicted position $\hat{y}_k$ for all input events $\mathbf{x_k}$, where $k = (1, \ldots, n)$ is the event number in the training data set,

$$\mathrm{RMSE}\left(\mathbf{W}, \mathbf{b}, \mathbf{v}\right) = \sqrt{\frac{1}{n} \sum_{k=1}^{n} \left(y_k - \hat{y}_k\left(\mathbf{x_k}; \mathbf{W}, \mathbf{b}, \mathbf{v}\right)\right)^2} \qquad (3.8)$$

The way the parameters are adjusted depends on the training algorithm used. The ANN minimization problems are hard to solve, because they are often very ill-conditioned [Lemaitre2009]. For such problems, the *Levenberg-Marquardt* (LM) [Wolfram2005] algorithm is often a good choice due to of its robustness and faster convergence. In this work all data processing and analysis were done using Mathematica$^{\mathrm{TM}}$, [Wolfram], with the neural network add-on package and LM algorithm availability [Wolfram2005].

When the ANN is trained too long, it can lead to over-fitting of the data in *validation* the training set. The ANN starts to fit the noise structure in a particular training set and hence losses generality (Fig. 3.15.a). To avoid this, we used a separate *validation* data set, from the same measurement, but not used in the training data set. After each training cycle, the total RMSE on all events in the validation data set is computed. While the total RMSE in the training set keeps diminishing as training progresses, the RMSE on the test events will come to a plateau or start to increase again (Fig. 3.15.a.b). At this point, training is stopped.

Finally, the performance of the trained ANN is evaluated using a third data set, *evaluation*
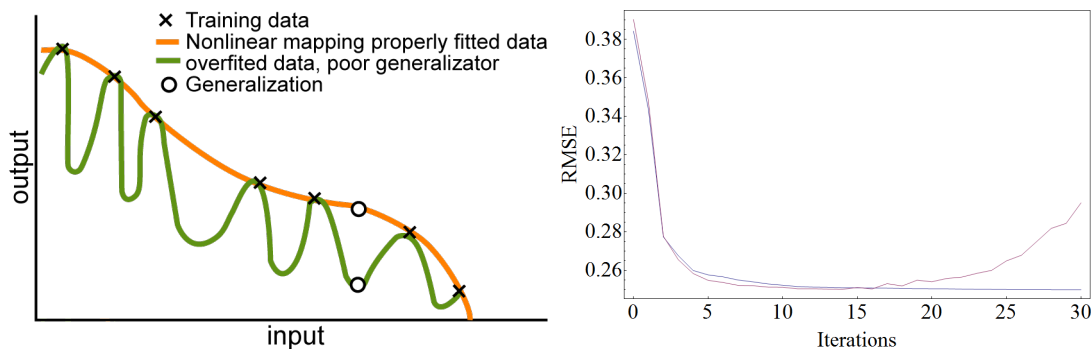
Figure 3.15: *ANN training. a). Generalization problem [Haykin1999] - over-training caused by loosing generality between similar training events b). Validation, training is stopped when the error for validation data start to increase*

an *evaluation set* that was not used in the training nor in the validating process. For each event in the evaluation data set, the impinging position is computed using the trained ANN, and the result is compared with the true position of the photon beam. The FWHM of the position error distribution obtained using all photons from every beam position yields an average spatial resolution.

4

Studies of an APD based monolithic block detector.

This chapter summarises the investigation done for an APD based detector. The first part describes the data structure and data acquisition process. All calibrations and preparation for measurement are described. Then the ANN structures used for the spatial resolution estimation are explained. The last part shows the result of the ANN robustness studies.

4.1 Materials and methods

4.1.1 Measurements characteristics

Two types of measurement are performed to study the performance of the monolithic block. In order to investigate robustness of the ANN algorithm, the LSO crystal is scanned by a perpendicular beam, along the horizontal direction for a constant vertical position, that is close to the middle of the one of APDs. This type is called later *a single line scan*. Scanning step is set to $0.25\,$mm and at one position the scanning time is $20\,$s. This results in ~ 50 events per beam position.

The second type of data sets are acquired, by scanning the whole surface of the crystal, with the step of $0.5\,$mm at different beam angles: $0°$, $5°$, $10°$, $20°$, $30°$ and $45°$. These are called *full line scan*. The scanning time per position is also $20\,$s ($\sim 200 - 300$ events). A full measurement takes around 20-24 h. This measurements is done to study the influence of the beam angle (for the considered size of the crystal block) on the spatial resolution of the detector.

The APD gain is set $10\,$V above the manufacturer specified voltage at which the gain is 50 V_{50}. It should give the final gain approximately 90x (see §.4.3.3). The temperature is set to be in the range of $17 - 19°$C.

4.1.2 Data arrangement

Data are read from the ADCs by a LabView control program and are saved in a raw form

$$\{x, y, t, \{64 \text{ ADC channels values}\}\} \tag{4.1}$$

where x denotes the horizontal location of the source along the crystal (expressed in μm), y vertical position and t the relative coincidence (register) time. The last element consist of 64 ADC channel values. If some of the channels are overflow, the event is rejected by the LabView control program. 12 bit ADC channel range have 4 V. Thus 1 bit correspond to ~ 1 mV.

Two channels in the setup were working not properly. First, the top APD array marked as $A3$ (Fig. 3.5) is dead, because of problem in one of the modules in the signal processing chain. The detected value of the channel has a random value. To prevent degrading influence on the ANN training is replaced with 0. The second problem is the last pixel labelled as $H4$ in the bottom APD. The reason is a broken connection between APD and the amplifier. This channel somehow reads only the noise level. This information is sometimes used to check the offset value. For higher gains the pixel $B4$ of the top APD is overflowed, because of high internal offset of CAEN amplifier. Otherwise this channel is working properly.

4.1.3 Type of source

The ^{22}Na source used in the measurement was produced in 01.04.2002, and its activity at the time of production was $100\,\mu$Ci. The activity at the time of measurement is therefore about 15 μCi.

The characteristics of ^{22}Na as a radioactive source are as follows: in 90% of the decays, in addition to a positron, a gamma ray of 1275 keV is emitted. In 10% of the decays, only the gamma ray of 1275 keV is emitted. That is another potential source of false coincidence detection. The influence of 1275 keV rays, also called $3^{\text{rd}}\,\gamma$, depends on the geometry of the setup. In this setup (Fig. 3.7) the fraction of $3^{\text{rd}}\,\gamma$ detected is approximately calculated at $\sim 8.7\%$ (see §.5.4). However this value can be still reduced by setting the energy window such as it cuts pulses with energy higher than photopeak, e.g. 600 keV. Then mainly scattered rays can be detected in coincidence. From the count rate plots the influence of events scattered on the background is roughly estimated at around 10% (see §.5.4).

4.1.4 Meaning of the non-perpendicular beam measurements

To diminish the training procedure in a realistic scanner, the number of trained networks should be reduced. It is done by considering the detectors ring as the pairs of coincidence detectors, rather than individual detectors. Thus the particular number of networks corresponds to each pair of detectors. This number depends on the range of incidence ray angles of all possible coincidences (i.e. passing through the FOV) between the detector pair. For a crystal block of 2 cm width and a standard PET ring diameter (of around 1m), the minimum requirement is one network. It is in case of opposite detectors, since the range of possible coincidences is smaller than 5° (Fig. 4.1). It is found in works of [Bruyndonckx2007a, Bryundonckx2003, Lemaitre2009], that the ANN works fine
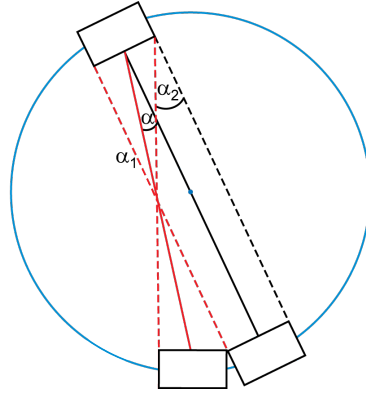
Figure 4.1: *Example of angle range $\langle \alpha_1, \alpha_2 \rangle$ for a particular detector pair.*

if the incidence angle is $\pm 2.5°$ from the angle that ANN was trained for. The top limit of required networks number is given by requirement that the coincidence is considered only if it pass through the FOV, e.g the adjacent detectors pair do not need to be trained.

Therefore the analysis of the influence of incidence beam angle on the spatial resolution estimated by ANN is important. On the level of the studies made in this work it is enough to speak about the incidence angles, but it is important to realise the relation of these studies with the realistic scanner.

4.1.5   Crystal shape estimation

The raster scans covers area slightly larger then the crystal itself. Thus the shape of the crystal can be seen as the count rate plot (Fig. 4.2 and 4.4). The edge of the plot is used to measure the beam size (see §.3.2.2). For ANN training only the data inside the crystal are selected, therefore information about the edge location along the crystal is required. The edges are defined as the positions, where the differences between successive rates have extremum (black line on Fig. 4.2). The distance between such calculated locations is 20 mm in the case of a perpendicular beam. When the crystal is rotated, the scanning range is wider then 20 mm. It is due to the enlarged scanning surface given by the crystal projection on the plane
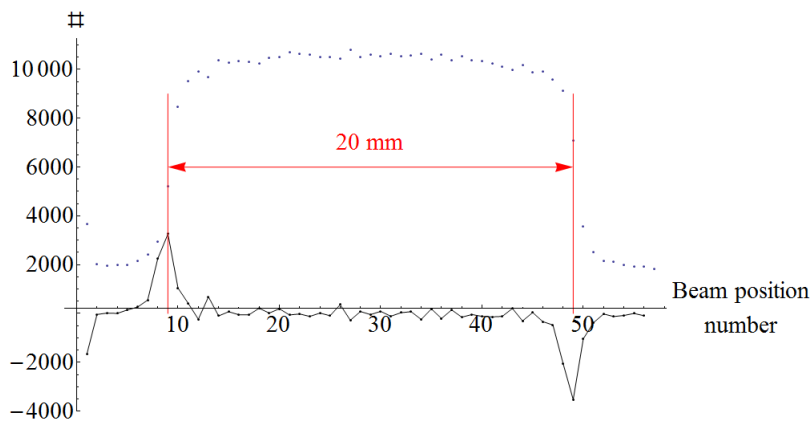

Figure 4.2: *Edge of crystal block estimation, based on the differences between count rate points along the crystal (black line).*

perpendicular to the beam direction (Fig. 4.3). On the edges of a such scanning range the beam penetrate smaller crystal volume. Thus sensitivity on the edges is lower and the count rate plot is smoother for bigger angles (Fig. 4.4).
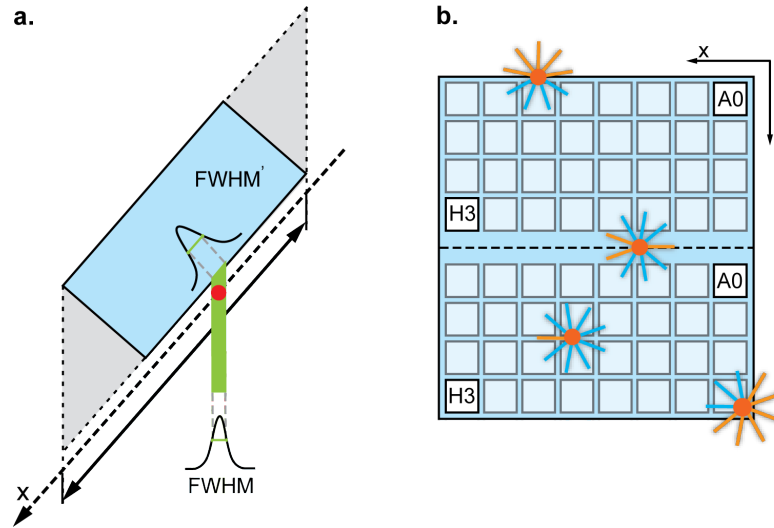

Figure 4.3: *Influence of beam angle and position on the analysis quality. a.) The influence of the beam angle on the spatial resolution and the scanning range; b.) Schematic the influence of the beam interaction position on the sensitivity (blue - example of scintillation rays detected, orange - example of rays lost)*

4.1.6   Random count

Before data acquisition, the setup was optimised to minimise the random fraction in the coincidence events. The random rate depends of the single rates of coincidence detectors - APD and PMT, and the coincidence time window (Eq. 1.13). The single rate of APD can be diminished by increasing the source distance from the detector, but it causes enlarging the beam size due to changed setup geometry. It can also be done by decreasing the APD high voltage, however this reduces the APD gain. The APD singles rate also diminish if increase the discriminating threshold of the signal.

The single rate of the PMT does not change significantly with the source position changes, since this distance is relatively big and the source can not be moved to much to not destroy the beam size. The PMT high voltage can not be to low, because of not high annihilation photon rate. The PMT single rate is also determined by the discriminating threshold.

The third factor, i.e. the coincidence window is determined dealing with time delay between PMT and APD signals and their time windows. It is set for 75 ns. Summarising, due to the compromise between these parameter, the random rate is estimated between $2-6\%$ of coincidences.

4.1.7   Calibrations - APD HV

The detector is tested for different value of the APD gain. To have the same value of the gain on all APD pixels, the same voltage offset relative to the voltage where the gain is 50 [APDdata], is used for all channels. To avoid unintentional
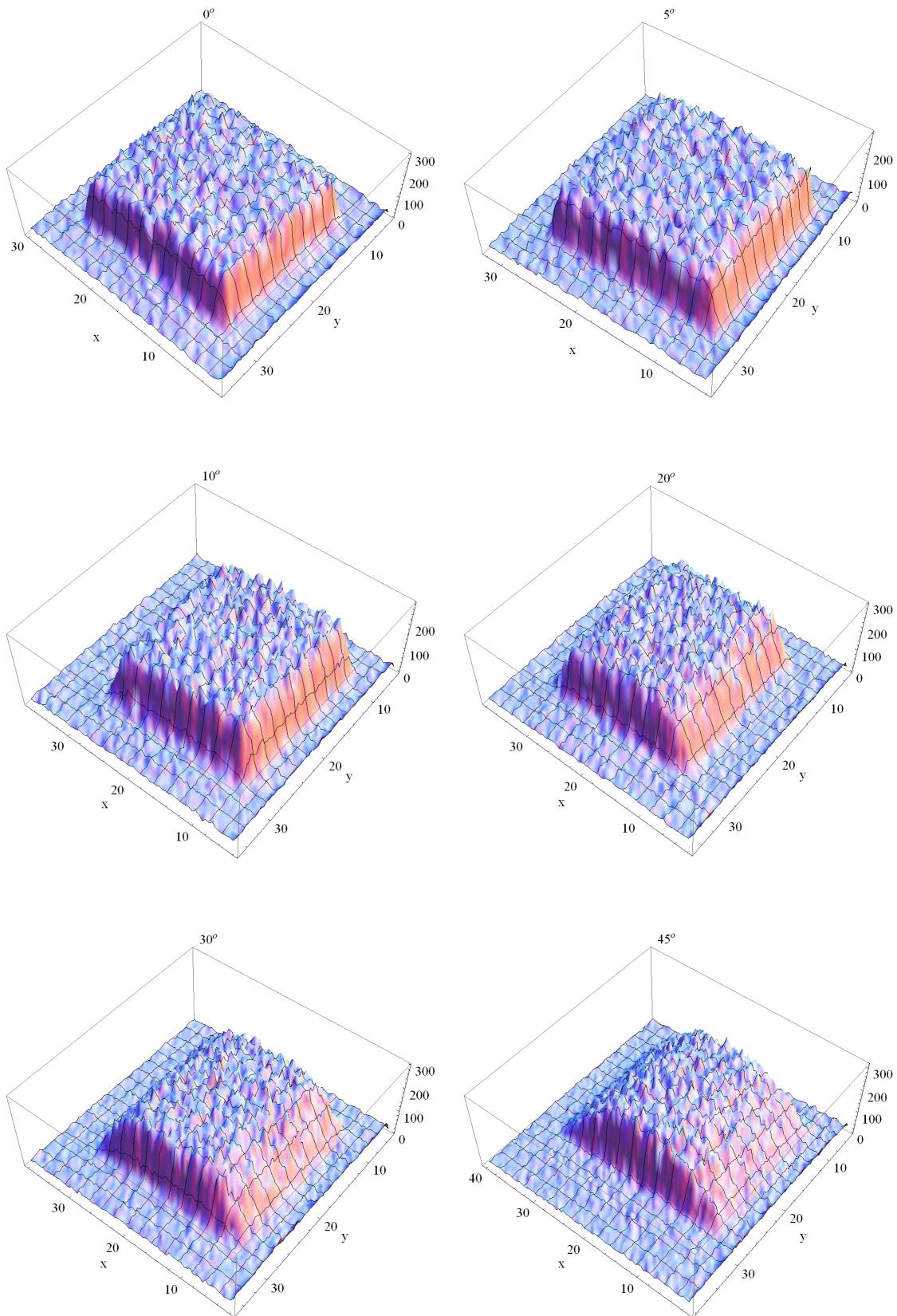
Figure 4.4: *3D count rate plot of full raster scan at beam angles (from the top left to the bottom right)* $0°, 5°, 10°, 20°, 30°, 45°$.

passing the breakdown voltage V_B, the APD power generator is calibrated. Each APD consist of two pixels arrays with separated power supply. Therefore two dual channel power supplies are used in the setup. The voltage is measured with use of Fluke 11 multimeter, with input impedance $> 10M\Omega$ [Fluke]. The voltage between HV display and output differs at around 6-10 V (dependently on the HV channel). It is caused by the wrong power supply display and the multimeter input impedance.

The power supplies voltage is set at $\Delta V = V_{50} + 10\,V$ for all applied APD subarrays. It is the voltage of the highest gain below the breakdown. Breakdown voltages for APDs subarrays, based on the S8550 APD data sheets, are respectively 473, 465, 480 and 479 V at the APD socket.

4.1.8 Energy resolution

To evaluate the energy resolution, a Gaussian function is fitted to the photo-peak in the pulse height spectrum for the sum of all the pixels per event. For this spectrum the spectra for all beam positions are added(Fig. 4.5). The energy of the photopeak is given by the position of the photopeak in the spectrum with subtraction of the noise peak position. The noise peak is acquired from a separate measurement, where the ADC triggering is random. The noise peak measurement is done for one particular beam position in the center of the crystal. For a full raster scan the energy resolution is $\sim 18\%$ (Fig. 4.5).

A slightly better energy resolution is obtained when using a single horizontal line scan measurement (Fig. 4.6), around $\sim 15.5\%$.This could be due to the fact that, a single line scan is made at the level of the bottom APD, where all channels send proper signals (see §.4.1.2). During the full raster scan, the beam moves over whole crystal surface, i.e. over two APDs. Two APDs consist of four submodules [Hamamatsu2006], each with rather constant gain. Each supermodule has own power supply channel. It probably gives four slightly different gains, unless the APD submodule high voltages are perfect. That could explain the broadening of the photopeak.
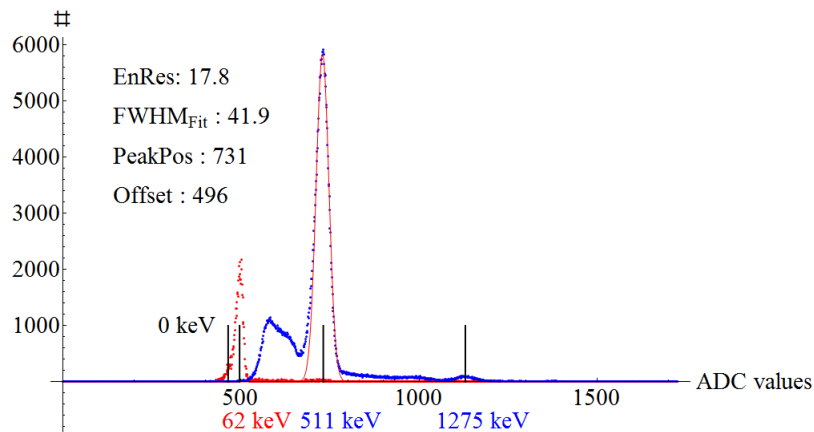

Figure 4.5: *Energy spectrum of ^{22}Na. The energy scale based on the known photopeak to high energy peak distance.*
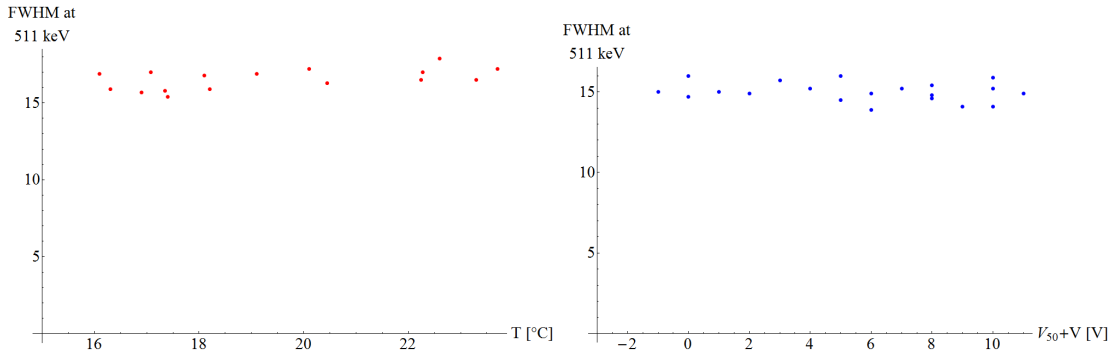
Figure 4.6: *Energy resolution for single line scan in function of temperature (left) and APD high voltage $V_{50} + V$ (right).*

4.2 ANN algorithms

4.2.1 Spatial resolution estimation

Several ANN training constructions are tried and the results are compared. Each requires its own evaluation. All calculations are done in Mathematica 6 and 7 with the use of the extra Neural Networks package. The final result of the algorithm is the estimated beam location along the crystal in x or y direction. The spatial resolution is the FWHM of the histogram from the differences between the position estimated by ANN and known beam position. The FWHM $= 2.35\sigma$, where σ is obtained from a Gaussian function fit to the errors histogram (Fig. 4.7). The Gaussian function is a good model to describe the error histogram. Nevertheless the bottom part of the error data usually are wider then it is predicted by Gaussian fit. Therefore, to see a relation with this deviation, the FWTM is also estimated. The FWTM is interpolated width at tenth of peak maximum.

On the other hand, in case of APD it is easy to overestimate the FWTM. It is
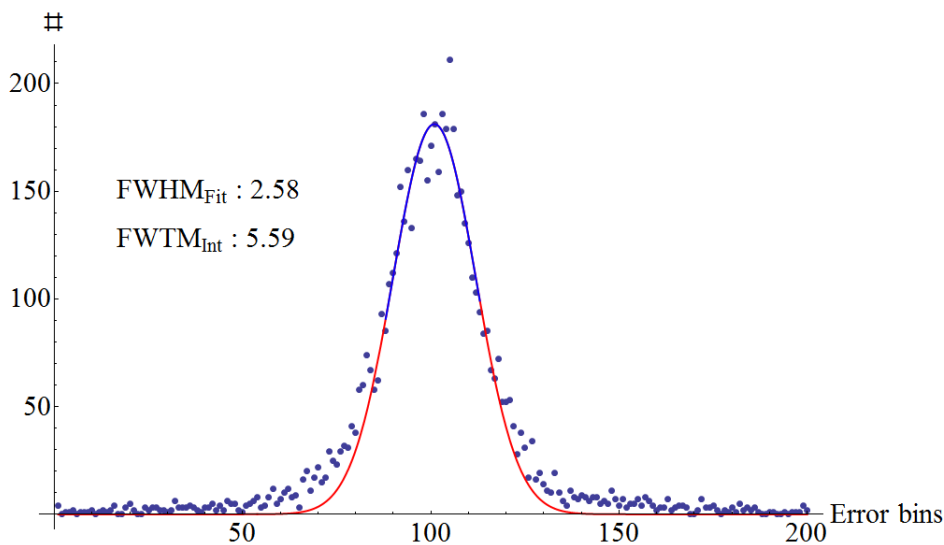

Figure 4.7: *Example of a Gausian fit to histogram of differences between known and estimated beam position. The FWHM$_{\text{Fit}}$ is the spatial resolution. The FWTM$_{\text{Int}}$ is the peak width interpolated at tenth of maximum.*

because the noise in APD setup can be more then 10%. The noise events consist: random fraction that is predictable (see §.4.1.6); the third 1275 keV gamma events influence, that is rather negligible if the ^{22}Na source is in distance bigger than 1 cm from the crystal (see §.4.1.3); and the events scattered from the background, but it is difficult to evaluate this fraction. The FWTM represents a few physical effects like: randoms, radioactive decay of LSO etc. but the FWTM interpretation in case of presented detector is difficult.

Because the resolution is measured in the plane perpendicular to the photon beam, acquired result is rather "LOR resolution", (Δx_{LOR}) then the detector resolution, Δx_{det}, that is usually measured in the plane of the detector. Schematically it is presented on Fig. 4.3. The relationship between the two resolution definitions is given by

$$\Delta x_{\mathrm{LOR}} = \Delta x_{\mathrm{det}} \cdot \cos \alpha \qquad (4.2)$$

where α is the photon incidence angle. This effect also causes smoothing the edges of the count rate plot (see §.4.1.5). All presented in this work spatial resolutions are Δx_{LOR}. This small calculus is presented to highlight the distinction between two plains where resolution can be measured (Fig. 4.3-left).

The spatial resolution estimation process uses only the data acquired when beam impinge in the crystal range. Unfortunately the ANN performs poorly, close to the edge of the crystal. This problem is called *edge effect*. There are two probable reasons. First, the real physical effect. It could be reflections, but it is not proved. The second reason due to training procedure. It is the edge of the output domain over which the neural network is trained. During the evaluation the network can estimate the beam position outside the crystal, while the known position is limited. These cause the increase of the systematic error on the edges and squeeze the error profile. However the problem is not yet fully understood. Simulation studies could help to understand the edge effect. Physically it might be a mirroring effect at the edges and should lead to an superposition of the light shapes [LiZhi2011].

4.2.2 Preparation data for network training

Only the events that fulfil certain conditions are selected from the raw data set, and form the *ANN data set*. First of all, only the data acquired from beam positions inside the crystal surface are accepted (see §.4.1.5). Another requirement is that events needs to have a total energy of at most 1 FWHM from the photopeak position, i.e. choosen data are in range of 2 FWHM over the photopeak. The photopeak range is set manually.

The ANN data are processed that each event consist of {8 ANN input, ANN output}. Where ANN input refers to the light distribution (see §.3.3) and ANN output is a known incidence beam position. There is separated ANN data set for each beam angle.

The ANN data set is shuffled (to avoid generalisation problem see §.3.3.2) and then divided on the training and validation set. The training set consists of 25% of whole data, but not more than 20000 events. It is found that 20000 events is enough to train efficient network in reasonable training time (Fig. 4.8). Rest of ANN data set is the data for network evaluation.
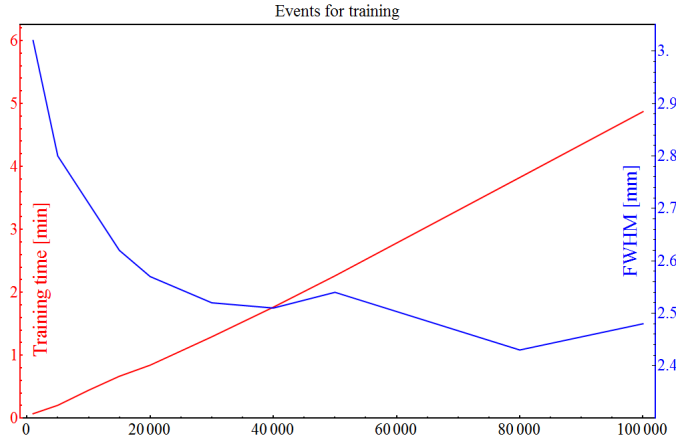
Figure 4.8: *Number of events required for efficient network training. Considering FWHM error of ≈ 0.1 mm, the FWHM becomes reasonably stable when more than ≈ 20000 events is used for training. Total number of events in this data set equals 200253. For training 30 iteration is used.*

4.2.3   Error of parameter estimation of the ANN

The error of the spatial resolution acquired from neural network evaluation is calculated as the standard deviation of 10 separated trainings on the same data. The procedure was applied to several data sets obtained from measurements with different conditions. The standard deviation is typically 0.1 mm. By changing the training data set, the resolution fluctuations are bigger dependently on the data set quality i.e. fault pixels number, noise level or geometry arrangement quality. However in a realistic scanner, the network needs to recognize and distinguish data sets not only between the beam position but also angles, so the error can be further enlarged.

4.2.4   GNN

The network modelled by the most straightforward learning approach is called here *general neural network* (GNN). The network (basis described in §3.3) is simply trained and validated with the training data set. Such trained GNN is then tested with the evaluation data set. For each event, the location of the photon beam is estimated and compared with the NN outputs. The FWHM of the histogram of these differences represents the spatial resolution. Schematically GNN process is described on the top part of Fig. 4.9.

The GNN method is used for general spatial resolution studies e.g. in 4.3. Results of data from full raster scan at different beam angles are shown at Fig. 4.10 (blue line). The resolution in x direction oscillates around 2.5 mm FWHM until 30° where it increases to around 3 mm and to ~ 3.5 at 45°. In the vertical direction it is relatively constant, because there is no rotation in this direction, and equals on average 2.43 mm FWHM. The operations presented in next sections allow to significantly improve this results.
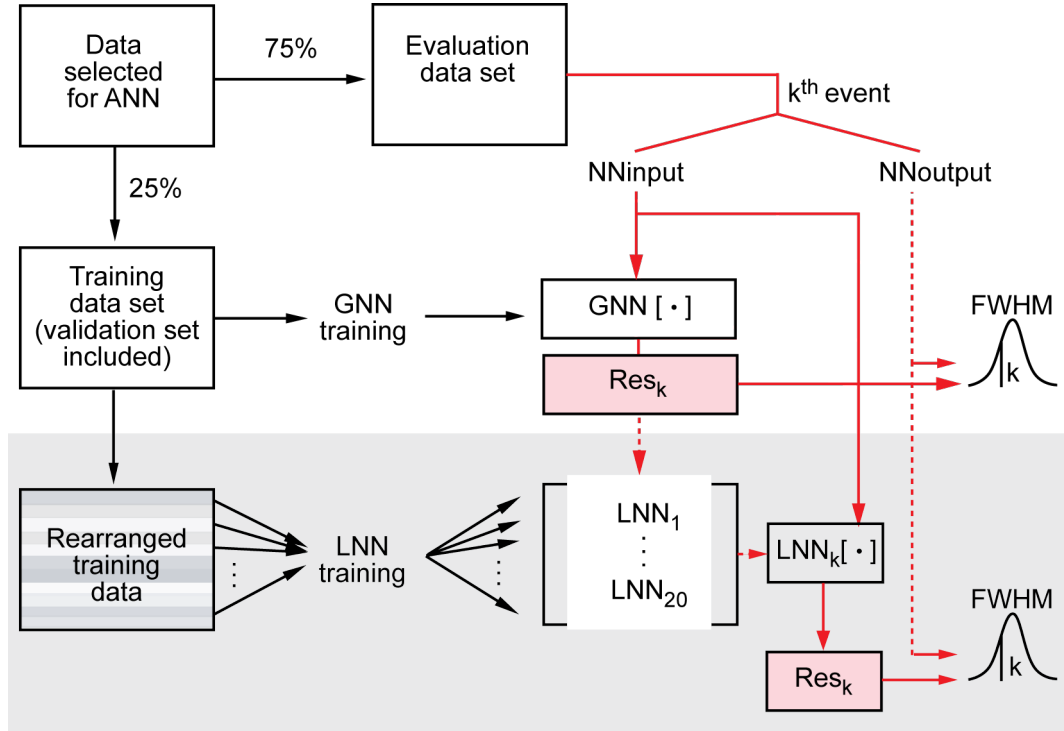
Figure 4.9: *Scheme of spatial resolution estimation by the ANN. The GNN - white bacground, the algorithm extended by the grey background part describes the LNN.*

4.2.5 GNN of center crystal data

The overall spatial resolution is degraded by edge effects (see §.4.1.5). To estimate the damaging influence of this effect, the GNN was tested with the data selected from the center of the crystal. The data registered for beam positions at less then 3 mm from the crystal edges are omitted. This operation improves the result considerably and gives a view of the potential best spatial resolution provided by the detector.

The results obtained on the center crystal part are shown at Fig. 4.10 (green line). This operation gives usually the best result. The horizontal resolution is rather constant, around 2 mm FWHM, until 20°. At bigger angles it starts to increase. At 45° it reaches around 3 mm. For the vertical direction it stays on average at 1.95 mm FWHM. In both cases the values from GNN are enhanced by around 0.4-0.5 mm.

However, in a realistic scanner, in order to achieve high sensitivity, edges have to be also considered. Until the problem of the edges is solved, the spatial resolution from the GNN needs to be enhanced in an other way.

4.2.6 Local performance

This approach is a supporting method that allows to look into details of the resolution estimating process. The network is trained in normal way (see §.4.2.4). But the evaluation set is divided in subsets of 1 mm beam position ranges along the crystal. The each group is evaluated separately. The example is shown on Fig. 4.11.

The best FWHM is found in the center of the crystal. A few mm from the edge
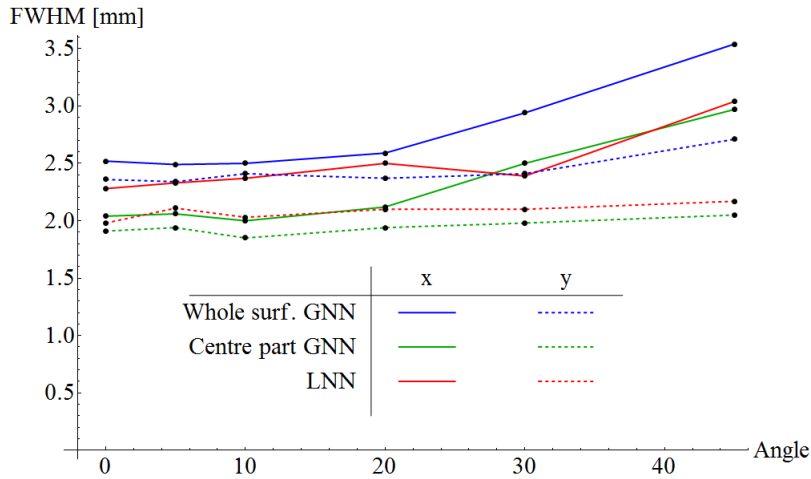
Figure 4.10: *Spatial resolution studies for full raster scan over the incident beam angle and for different ANN approach.*

resolution is worse due to edge effects (see §.4.2.1). It is in data ranges $5-6$ mm or $14-15$ mm at Fig. 4.11. The FWHM and FWTM very close to the crystal border are enhanced. There the GNN can give positions that are outside of the crystal. Then the local resolution profile is squeezed, due to systematic error that rises quickly at the edge. The systematic error describes how much the error histogram is shifted from the position 0.

Results of local analysis are put together on one plot for each data set. The horizontal analysis of full raster scan analysis at different angles is shown on Fig. 4.12. The FWHM is obtained due to Gaussian fit (FWHM$_{\text{Fit}}$). Whereas FWTM is approximated by interpolation (FWTM$_{\text{Int}}$). The behaviour of the functions get worse with the angle, especially higher then $30°$. The FWHM in the center shows a resolutions below the results obtained from GNN. It is constant and close to 2 mm FWHM. The systematic error reaches maximum at the edges of the crystal. The behaviour of FWTM is analogue to FWHM. But since it is interpolated at tenth of the photopeak height and due to high noise level, it is usually overestimated. Therefore the FWTM in this setup is not the most reliable parameter.

For angles bigger than $30°$ some artefacts also appear, i.e. such as the FWHM peak significantly increased around 5 mm from the edge. Besides the edge effects, it is due to the top APD, the dead channel A3 and bigger offset of channel B4 (see §.4.1.2). They are both in the region of anomalies. Especially channel A3 send false signal for the ANN during the training.

Fig. 4.13 shows the local results in vertical direction analysis. Since that is not in the axis of the crystal rotation, these result does not depend of the angle. Therefore only one plot is presented.

4.2.7   LNN

The aim of this approach is to train networks in smaller data regions. It could partially eliminate the influence of false events, that bring false information to network during training.

The training process requires a rearrangement of the training data set. The set is divided in smaller, equal subsets, that correspond to each 1 mm along the
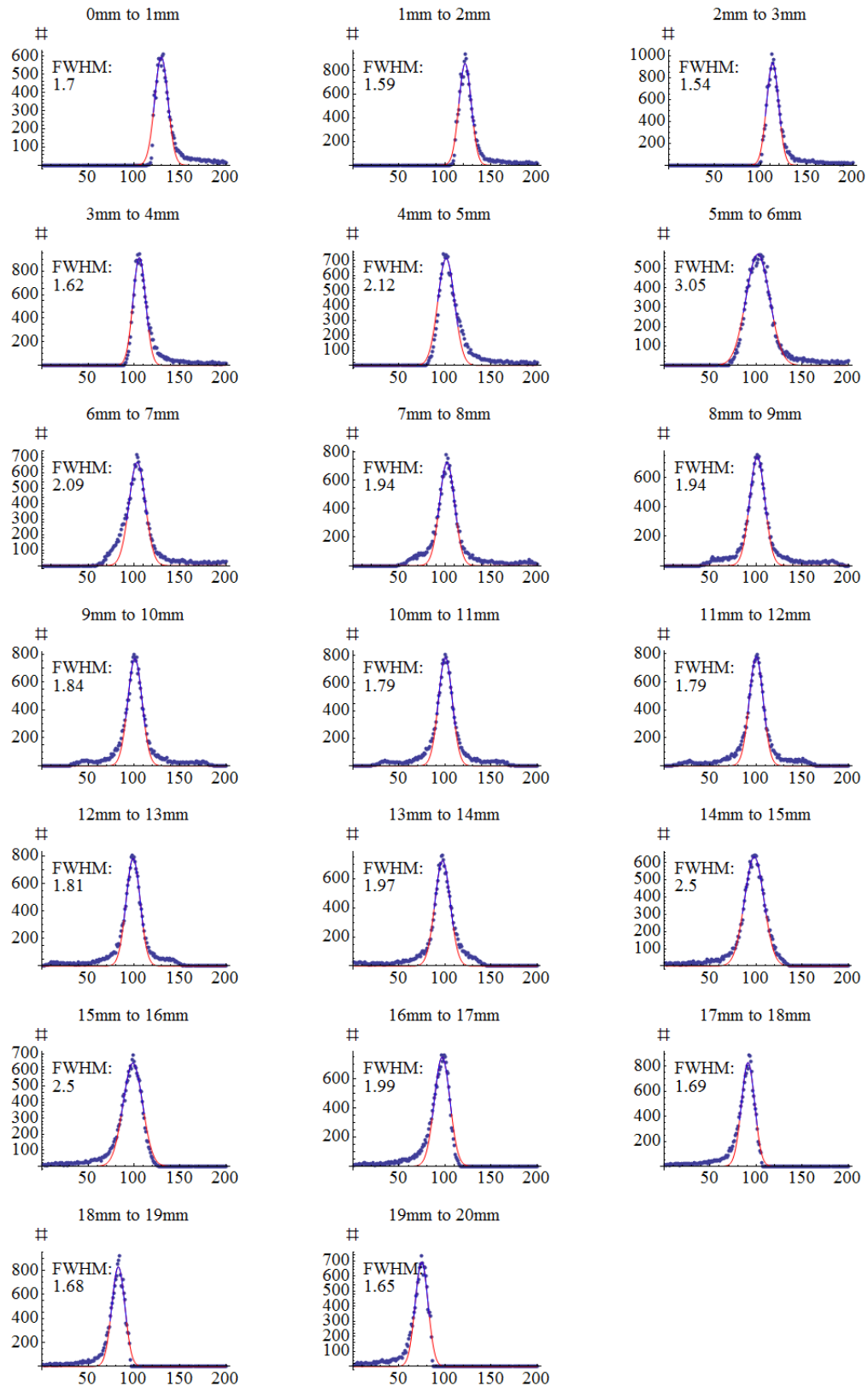
Figure 4.11: *Local spatial resolutions (FWHM value) for a full horizontal raster scan at perpendicular beams ($\Delta HV = V_{50} + 10$, 20 s scan per position, scanning step 0.5 mm, $T = 17°C$). Red plot is the Gaussian fit function.*
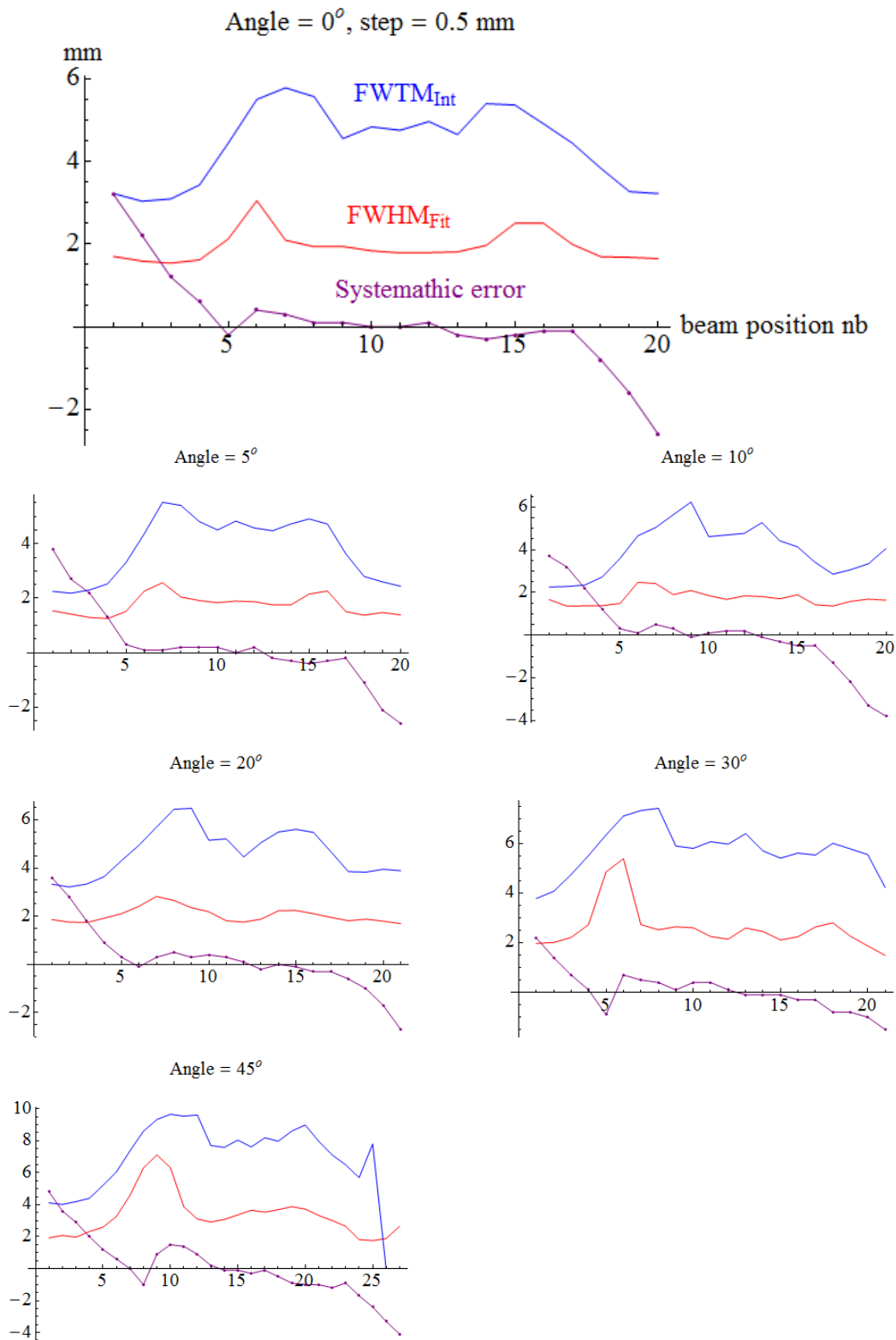
Figure 4.12: *Local performace of GNNs evaluation at different beam angles: systematic error, FWHM (from Gaussian fit), and FWTM (interpolated). Result for full raster scan analysed in **horizontal** direction ($\Delta HV = V_{50} + 10$, 20 s scan per position, scanning step 0.5 mm, $T = 17°C$)*
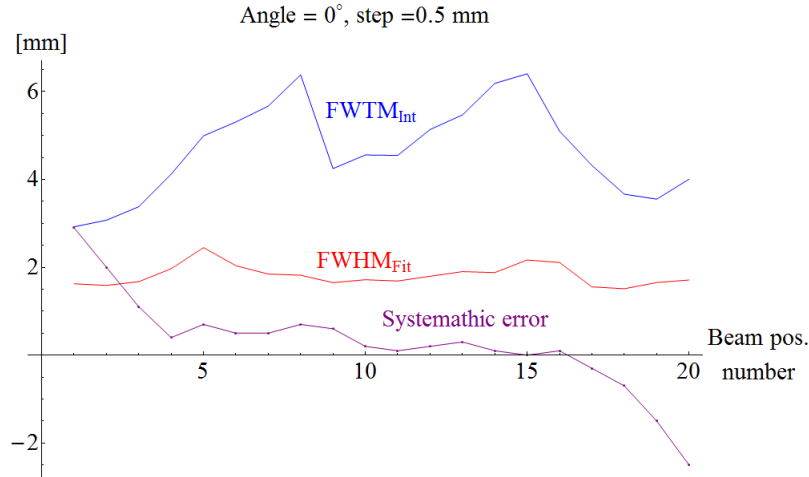
Figure 4.13: *Local information of GNNs evaluation: systematic error, FWHM (from Gaussian fit), and FWTM (interpolated). Result for full raster scan analysed in* **vertical** *direction($\Delta HV = V_{50} + 10$, 20 s scan per position, scanning step 0.5 mm, $T = 17°C$).*

crystal surface. The subsets width is 5 mm, so that there is substantial overlap between neighbouring regions. Each subset is used for training individual networks. The number of local networks depends on the number beam positions along the analysed direction, so also on the angle of incidence beam (see §.4.1.5). For example for a perpendicular beam there are 20 LNN along 20 mm surface.

Evaluation process consists two steps. First, where considered event is evaluated with GNN. Such estimated beam position just indicates which LNN should be chosen for a real evaluation. The FWHM obtained in that way is usually much better than results from simple GNN.

The resulting spatial resolution for a full raster scan in the horizontal direction is improved of around 0.2 mm (Fig. 4.10 - red line). This method allows to push overall resolution closer to the level of the result acquired within the center part of the crystal (see §.4.2.5). The most significant improvement is found for angles bigger than 30°. For the last two angles, the resolution is the same as these obtained from GNN evaluation with the central crystal data events. The LNN results in y direction are slightly worse compared to these from the center data events evaluation. It stays constant around 2.08 mm FWHM.

The LNN approach is especially effective in case of a single line scan. It can be caused by edge effects that have bigger influence for full raster scan, since the effect is summed in the network data set for full raster analysis. Anyway the LNN is a solution proposed for a future PET scanner since it always enhances final resolution.

4.2.8   5GNN

To check the accuracy of the network training, *the five general neural networks* 5GNN are trained. The training data are divided in 5 different sets, each 20000 events. In case of files with a too short data length, the set is shuffled five times and each time the first 20000 events are chosen. All sets are individually trained, thus 5 different GNN are obtained. Next, each event from evaluation data set is tested with each of these networks (Fig. 4.14). Resulting estimated position are
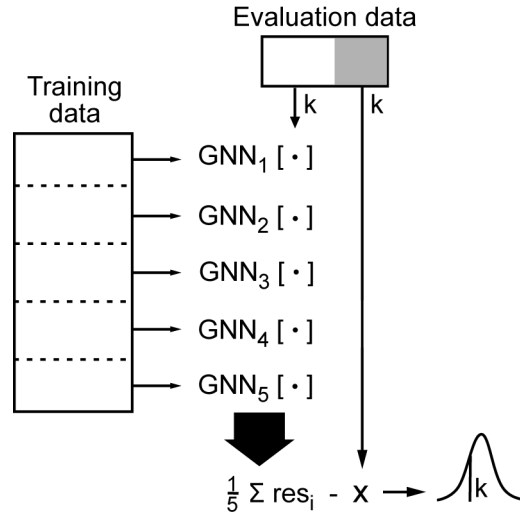
Figure 4.14: *The training scheme of the 5GNN approach.*
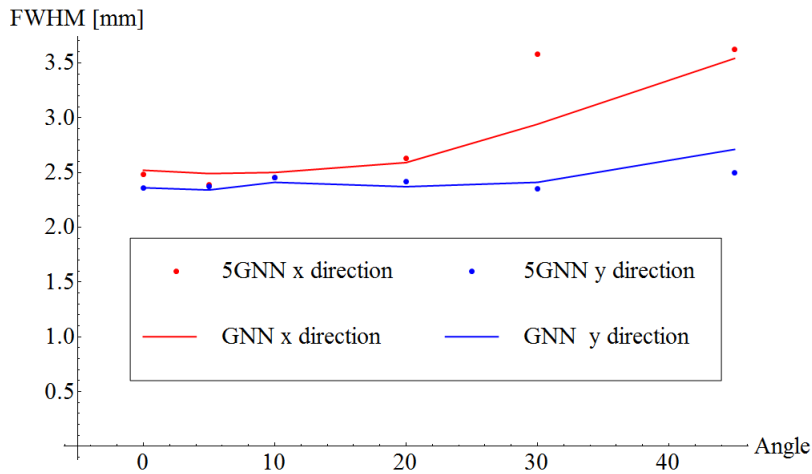
Figure 4.15: *Spatial resolution obtained from the standard GNN approach per the incidence beam angle in comparison with the results of the 5GNN training approach.*

averaged and used for spatial resolution estimation (see §.4.2.1).

This method doesn't improve the potential systematic error on the estimated beam location. If there is a constant source of error, it is not recognized by 5GNN. If the result of GNN is changing more significantly from one training to another, then the 5GNN can be used for better approximation. In this case 5GNN improves precision of the calculated beam.

The comparison results from the 5GNN approach and the GNN are shown on the Fig. 4.15. The data analysed come from the full raster scan at different angles. Generally results from 5GNN and GNN are relatively uniform, except the resolution of beam at 30° that is visibly deviated. There is no explanation for this anomaly. It is also checked that applying 5GNN results in LNN approach doesn't significantly change the resolution in comparison with standard LNN approach.

4.2.9 Data pre-filtering

One more idea is tested. It is a specific pre-filtering of the training data, done before the ANN training process. Raw neural network inputs are formed in eight numbers for each event (see §.3.3.2). The maximum of the the particular network input is considered as the position that is the closest to the incidence point. This maximum is compared with the known beam position. In some cases the difference is bigger than 3 mm, and then the event is removed from the training data set.

The aim of the previous filtering is to simplify the training process, make it faster and more accurate. Apparently the resolution obtained in such way is hardly better (never more then 0.1 mm FWHM). Actually sometimes it is even worse then the results obtained without prefiltering process (usually of about 0.2 mm FWHM). From these reasons this approach is not applied for spatial resolution reconstruction.

The power of the ANN learning seems to be stronger then the manual filtering. It is possible that during the filtering, not obvious useful informations about intrinsic signal deviations are ejected. Thus the training set can be deformed.

4.3 Robustness of ANN

To investigate the robustness of the ANN algorithm, several measurements in different conditions are done. To decrease the data acquisition time, instead of a full raster, only one horizontal line scan along the LSO block is made. Conclusions are drawn from the comparison of the different results. A perpendicular beam is positioned at the center of the bottom APD, because it has better channel activity (see §.4.1.2). The APD voltages are set at $V_{50} + 10\,\mathrm{V}$ as default,. The temperature during measurements is set at $18 \pm 0.6°C$. The beam step size is reduced from $0.5\,\mathrm{mm}$ to $0.25\,\mathrm{mm}$. The rest of settings is the same as in the full raster scan.

4.3.1 Influence of random events in ANN training data

The robustness against random events in the NN training data is evaluated. It gives a view of the random events influence in a realistic scanner.

The fraction of random events present in the measured data set is computed by Eq. 1.13. In order to change the random fraction in the data set, additional random events are added by assigning random, uniformly distributed, positions to a given fraction of training events. The neural network, trained with such a data set, is tested with a real data set without artificial random events added (indexed by *ED*) or with an affected data set (*ED+R*). Two training mechanisms are applied, the standard GNN and LNN. Schematically the analysis is presented at Fig. 4.16.

The Fig. 4.17 shows the obtained FWHM resolution as a function of the percentage of random events added. The zero point on the horizontal axis corresponds to a random fraction of $\sim 2 - 3\%$. The LNN is much less sensitive to random influence then the GNN. A significant degradation of the spatial resolution for LNN starts only when, more than $20 - 30\%$ of randoms are added. Below this value the influence of other factors such as signal to noise ratio are probably more important in determining the attainable resolution. The GNN is already less accurate
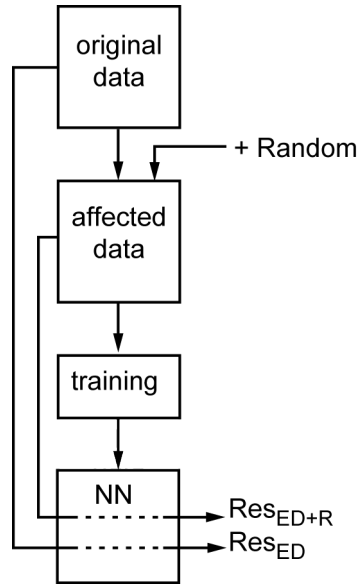
Figure 4.16: *The ANN robustness against random events analysis scheme*
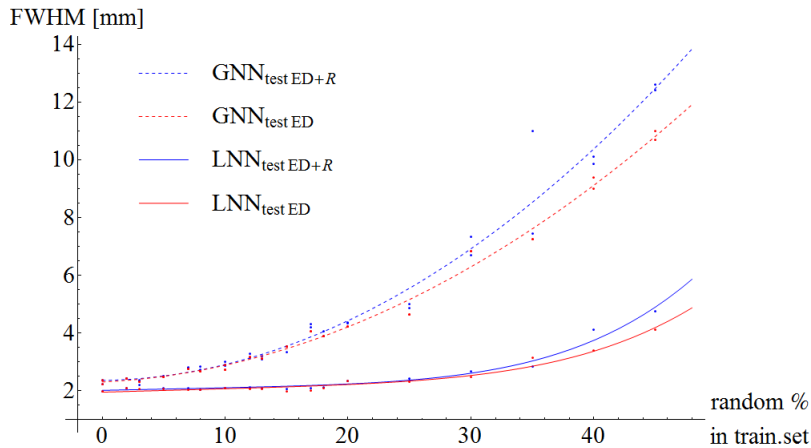
Figure 4.17: *Influence of random events in training data set on the resulting spatial resolution. $GNN_{test\ ED+R}$ - the GNN trained with the evaluation data containing artificial random events, $GNN_{test\ ED}$ - the GNN trained with original evaluation data, for LNN respectively the same options $LNN_{test\ ED+R}$ and $LNN_{test\ ED}$.*

when 10% of random is introduced to the training set. The difference in resolution between testing sets ED and ED+R is rather negligible for a reasonable random fractions range. For higher random fraction the undisturbed set gives slightly better resolution.

4.3.2 Spatial resolution dependency on the temperature and APD high voltage

The aim of this analysis is to predict the environmental influence on the spatial resolution of a future PET machine. Data are acquired for temperatures ranging from 16 to 24°C and next for different gains expressed as the APD high voltages V above the voltage V_{50} needed to operate at a gain 50 . Several measurement at the same conditions are repeated to check the system stability. Thus for some
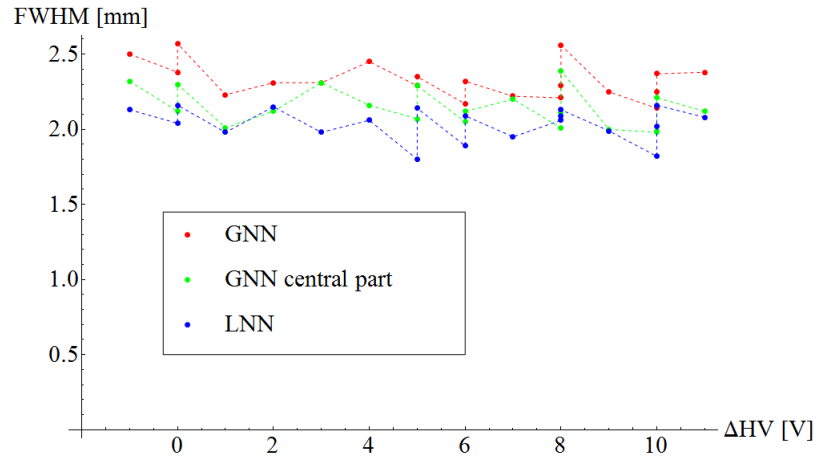
Figure 4.18: *Spatial resolution in function of gain expressed as APD high voltage above V_{50}. Central part of the crystal consist the surface range more then 3 mm from the edge.*
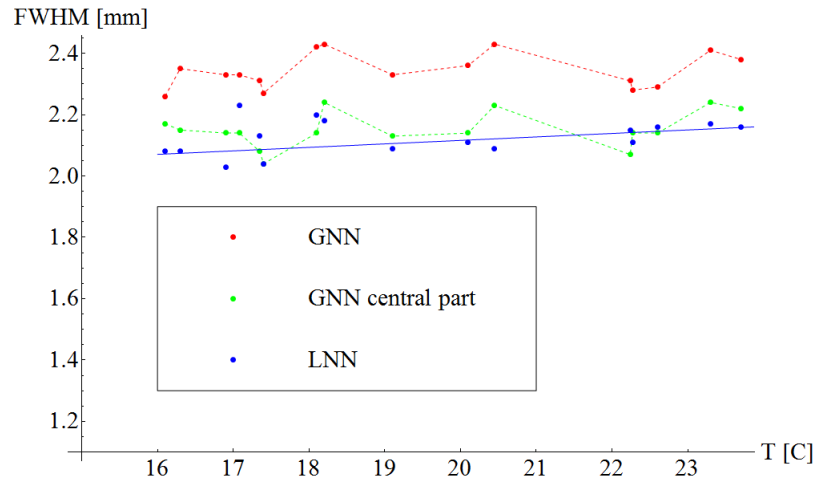
Figure 4.19: *Spatial resolution in function of modulated temperature inside the box. Central part of the crystal consist the surface range more then 3 mm from the edge.*

temperature or HV values more results are plotted (Fig. 4.18 - 4.19). Data are acquired in a single horizontal line scan. For each set an individual network is trained and evaluated. The analysed HV and T ranges are not wide, because the aim of this test is not to measure the endurance of the detector but the harmful influence of the potential T and HV fluctuation in realistic scanner. In a well working commercial device these changes shouldn't be larger than considered here.

The top of the HV range is determined by the APD breakdown voltage V_B. The bottom limit is set by the value, where the photopeak is still easily distinguished from the noise in energy spectrum and no problem with the hardware threshold occurred. Within this range we do not observe any dependence on the resolution on the gain of the APD (Fig. 4.18). Chosen HV fluctuation range provides stable spatial resolution.

Considering temperature analysis, the upper limit is set by the temperature at stable conditions in a non-cooled system. The lower limit is determined such as there is no risk of water condensation inside the box. The temperature is measured by a probe close to the LSO block (Fig. 3.8). Data acquisition is started

when the thermometer indicates a stable value. An increasing temperature slightly deteriorates the spatial resolution (Fig. 4.19). The fitted function indicate some resolution degradation with the temperature. It is expected, but since the FWHM error is ~ 0.1 mm the fit can have also different slope. Then expected degradation can be not visible.

Considering §4.2.4, §4.2.7 and §4.2.5, three types of results are presented on Fig. 4.18 - 4.19, resolutions from standard GNN, LNN and center evaluation data GNN. The differences between these three methods are not the same as in case of full raster scan. The resolution obtained from GNN approach, at the temperature of full ratster scan measurement, $\sim 18°$C, is almost the same. However the LNN gives resolution similar to the center part of the crystal. In case of full raster the there is significant difference between the result of these two methods. That could be explained by the fact, the influence of edge effect on overall resolution in full raster scan is bigger then in single scan.

4.3.3   Photopeak position in function of temperature and gain

The analysis, that result is shown on Fig. 4.20, is done to check the relation between the system signal amplification and modulated temperature inside the box or APD voltage supply. The photopeak position is calculated by subtraction the noise peak position, acquired from separated measurement, from the relative photopeak position on energetic spectrum. Photopeak scale is given in the signal amplitudes registered by the ADC (see §.4.1.2). The gain smoothly increases with the APD high voltage and decrease with growing heating in the detector.

The gain of the detector can be estimated, from the plot of photopeak dependency on the APD high voltage. The voltage during measurements is set at $V_{50} + 10$ volts. Since the the gain of V_{50} is known, it is found that the gain during measurement is around 90. In this small range of high voltage fit by a line function is reasonable model.

The photpeak position decreasing with increasing temperature can be explain by two facts: the APD gain is temperature dependent, and the LSO light yield as well [Weber2003]. The LY dependency is $-0.7\%/°C$ [Rey2007]. The change of the photopeak position, estimated from the plot at left on Fig. 4.20, equals $\sim -4\%/°C$. It means that $-3.3\%/°C$ is due to the gain change and the rest due to light yield.
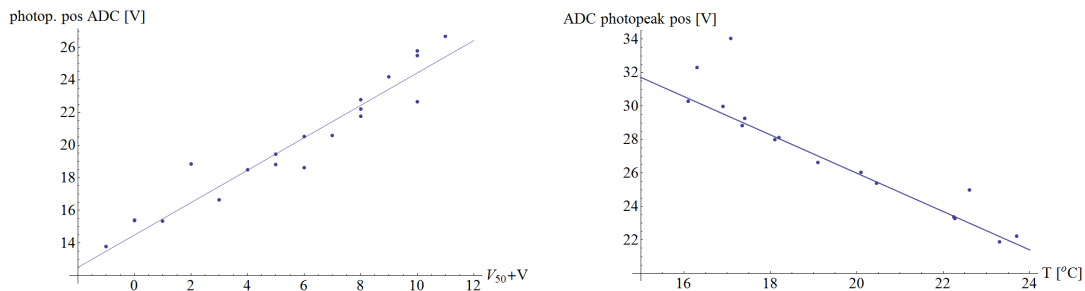

Figure 4.20: *Photopeak position dependency on APD HV and temperature.*

4.3.4 The temperature and APD high voltage fluctuation influence for ANN training

In a real system, the HV can drift over time. In section 4.3.2 the influence of high voltage on the spatial resolution is presented. For further study of this issue, the impact of HV differences between the time the training data are acquired, and the time the trained network is used, is investigated.

The training data are collected for several APD high voltages $\Delta HV = V_{50} + V$, $V = \{0, 2, 6, 8, 10\}$ V. Each of these five trained networks is evaluated with the data sets acquired at different APD voltage.

The result of this analysis is summarised in figure 4.21. The figure shows the difference in spatial resolution between:

a) a measurement where the training data set and the evaluation data set are acquired at the same APD voltage,

b) a measurement where the training data set and the evaluation data set are acquired at different voltages.

Each plot shows this difference is resolution, when the training data set is acquired at a given voltage, as a function of the voltage, as a function for the evaluation data set. In each plot, the voltage used for the training data is shown as a grey highlighted point.

The error of the resolution difference is $\sqrt{2} \cdot 0.1$. The error of spatial resolution is considered as 0.1 (see §.4.2.3). It is applied to all presented in this section results.

In this plots we noticed an anomaly for the data acquired at $V_{50} + 5$. This is probably due to same problem with this particular data set.

We can conclude from this plot that there is no significant degradation in resolution if the difference in voltage is less than 4 V.

Both parameters the light yield of LSO and the APD gain are temperature sensitive. Hence a temperature shift results in a change of measured light distributions. To study a possible impact of temperature changes on the spatial resolution, the analysis analogue to presented above is done. A neural network trained separately with data acquired at temperature $T = \{17.4, 19.1, 20.45, 23.3\}^{\circ}$ C is evaluated with data acquired at different temperatures.

First observation from the plots Fig. 4.22 is that LNN significantly improve an accordance of the resolutions. Some results from GNN are spread (for $T = 20.45^{\circ}$C or $T = 23.3^{\circ}$C) and there is no clear uniformity in behaviour against the temperature. Result seems to be smoother if points for $T = 19.1^{\circ}$C, 20.1°C and maybe 23.3°C are omitted. Taking into consideration that air conduct the heating slower then metal elements inside the detector box, there is some uncertainty on the true APD temperature.

Concentrating on resolutions calculated with LNN and concerning the resolution error, the influence of temperature data set mismatch on the network evaluation is quite small. Generally there is no significant change in range around 5°C from the temperature that training data are acquired. On the plot for $T = 23.3^{\circ}$C the LNN there can be some resolution deterioration under the temperature of 17°C, i.e. if the mismatch is higher then 6°C. Results from GNN in most of analysed cases are very spread, therefore the conclusions are based on LNN results.
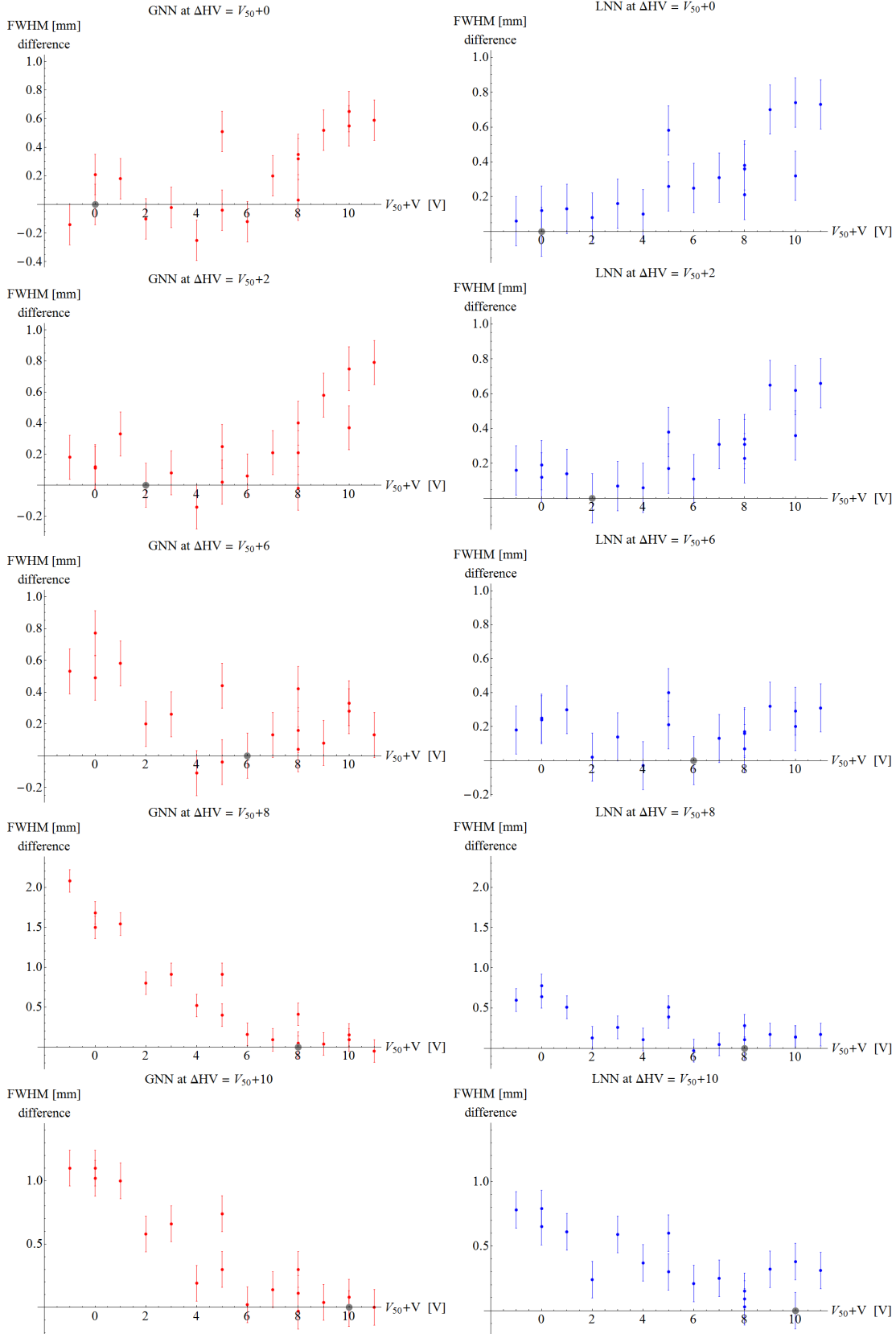
Figure 4.21: *If the training data are acquired at different condition than the evaluation data, the resolution is degraded. This will be the case e.g. for differences in APD supply voltage. The plots presents measurement of this effect for five GNN (red) or LNN (blue) trained at $V_{50}+0, V_{50}+2, V_{50}+6, V_{50}+8, V_{50}+10$ V. Plots show differences in resolution with respect to the resolution trained and evaluated at point highlighted in grey.*

Figure 4.22: *Differences between GNN (red) or LNN (blue) trained at certain tempera-
ture and corresponding original resolutions. If the training data are acquired at different
condition than the evaluation data, the resolution is degraded. This will be the case e.g.
for differences in temperature inside the detector box. The plots presents measurement of
this effect for four GNN (red) or LNN (blue) trained at $17.4°C, 19.1°C, 20.45°C, 23.3°C$.
Plots show differences in resolution with respect to the resolution trained and evaluated
at point highlighted in grey.*

4.3.5   Temperature and APD high voltage error
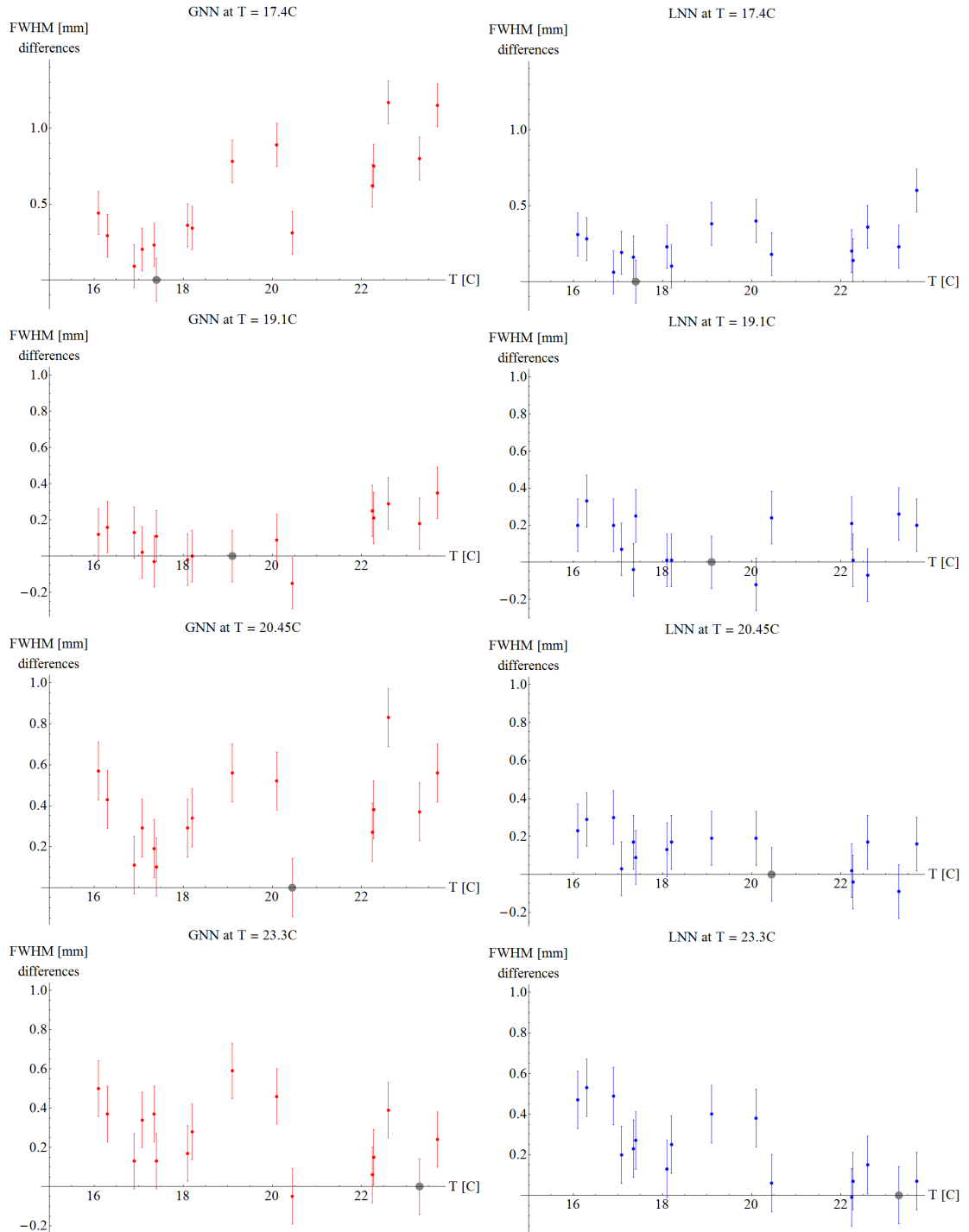
After start-up the setup needs time to stabilise; more in particular the temperature needs time to stabilise. The measurements are started when the temperature change of the temperature probe is lower then 0.6°C over five minutes. However, the measured value does not reflect the real APD temperature. It examines the air environment around the photosensor. Most of the heat is transferred by the connections with the PCB, where the pramplifiers are mounted, the main source of heat. Therefore the temperature error can be much bigger then 0.6°C.

We use two, home-made, two channels, power supplies to provide the high voltage of the APDs. For longer measurements small voltage display change is observed. The influence of this fluctuations is difficult to evaluate.

4.4   Conclusions from ANN robustness studies

The horizontal resolution for perpendicular beam is in the most straightforward GNN approach 2.5 mm FWHM. By choosing the center part of the beam position data for network evaluation the result is pushed to around 2 mm FWHM. In vertical direction corresponding resolutions equals 2.4 and 1.9 mm FWHM. Local analysis of full raster scan confirms the resolution in the center of the crystal as below 2 mm. However, in a realistic scanner whole surface of the crystal needs to be considered. Therefore the resolution in the center part just indicate potential limit of used detector. The resolution of full data is deteriorated by the edge effects. Nevertheless the use of LNN approach every time enhances the result. The resolution acquired with LNN for perpendicular beam, in x direction is about 2.3 mm, and in y direction around 2 mm FWHM. This method is proposed for future scanner designs. In single line scans LNN is able to push resolution to the level of central part of the crystal.

The spatial resolution is found to be stable up to the angle of 20-30°. If employ additive LNN analysis the degradation begins later. Also with LNN the systematic error is smaller over the incidence beam angle. At the angle 30° the resolution estimated by LNN method is around 2.5 mm FWHM. In the same situation, the error in case of a pixelated detector PET (of 1 cm pixel length), is in range of 5 mm. That is around two times of the result from LNN and makes proposed crystal design competitive.

The ANN algorithm is rather robust for small temperature and APD high voltage fluctuations. It is of order of a few °C and a few volts respectively. Such small fluctuation shouldn't but may appear in a realistic scanner. It is shown it has negligible influence.

The ANN works fine if the fraction of random events in the data set is lower then 10% for GNN method. In case of LNN the resolution start to be worse significantly at more than 25-30% of random in the data set.

5

Study of detectors using alternative light sensors

Here the analysis of data from two PMT and one SiPM based detectors is considered. The first three sections are directed at individual detector resolution. The last one presents conclusions from the comparison between block detectors equipped with the different light sensors.

The monolithic block detector design is an approach investigated by several groups in order to find the most satisfying performance. By courtesy of the group from the University of Science and Technology of China (USTC), Hefei, the group from Delft University of Technology (UT), Netherlands and the group from Forschungszentrum Jülich (FZJ), Germany, three other detectors data were analysed. The main difference between these detectors is the light sensor: two use PMTs, and one uses a SiPM. All data sets were analysed with the same ANN based spatial resolution estimation procedure.

5.1 Data from the PMT based detector - USTC

5.1.1 The detector and data acquisition description

The data received from USTC come from a detector, that instead of using a APD as a light sensor, uses a PMT. Instead of LSO, LYSO scintillator is used [Kimble2002]. However LSO and LYSO have very similar properties as a scintillators and this difference should not matter very much for a comparison. The data acquisition setup is based on the same general idea as presented earlier in this work.

The data are acquired from a detector that comprises a $25.5 \times 25.5 \times 10 \, \text{mm}^3$ monolithic LYSO scintillator coupled to a Hamamatsu 64 channels multi-anode
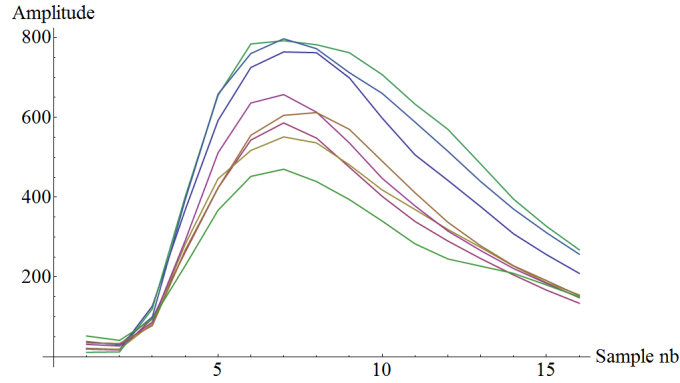
Figure 5.1: *Single event presented as 8 sampled sums of signals from PMT pixel columns.*

PMT H7546B [Hamamatsu2007a]. This PMT construction consist of the Hamamatsu PMT model R7600-00-M64, the same as used later in §5.3. The sensitive area of the PMT ($18.1 \times 18.1\,\text{mm}^2$) is smaller then the size of the crystal. This arrangement reduces the detection efficiency of the detector, but is compatible with the future scientific plans of the group [Yonggang2010]. One detector module with a $\varnothing 5.0\,\text{mm}$ Pb-collimator (Pb thickness $50\,\text{mm}$) is used to create a narrow beam [Yonggang2010] from a $\varnothing 0.25\,\text{mm}$ ^{22}Na point source, using the principle of geometrical collimation, that is explained in §3.2.2. The measured beam size is 0.6 mm. A detailed electronics setup description can be found in [Yonggang2010].

Data are acquired using a perpendicular incident photon beam from the single horizontal line scan from the left to the right side (-12 to $12\,\text{mm}$) of the LYSO with a step size $0.25\,\text{mm}$ at the vertical middle of the crystal ($y = 0$). At each position 2048 events are recorded. The PMT pixels are summed in 8 columns (see §.3.3) ant continuously sampled at 50 MHz. When a photon is detected 16 samples of each of the 8 summed signals are stored (Fig. 5.1).

5.1.2 Energy resolution -spectrum

By placing the radioactive source between the two detectors an energy spectrum is measured. The energy resolution equals $\sim 14\%$ of the $511\,\text{keV}$ [Yonggang2010]. We cannot confirm this information with the data set we received, because insufficient information about the offset.
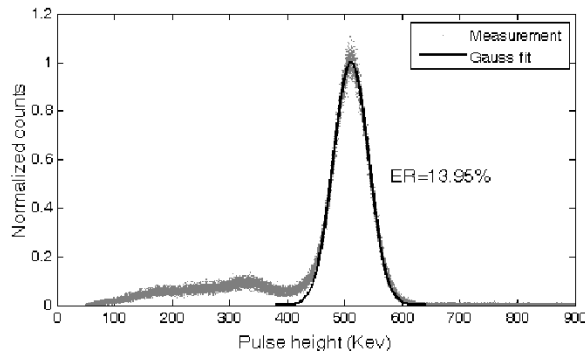
Figure 5.2: *The energy spectrum [Yonggang2010].*

5.1.3 Result on position resolution

The way of the data saving allows to introduce two type of ADC simulation. *integrating vs peak* The event energy, as the example shown in Fig. 5.1, can be given by the amplitude *sensing ADC* of the signal (as in a peak sensing ADC), or as integral under the signal plot *simulations* (integrating ADC). Both of approaches are tried.

The Fig. 5.3 shows the spatial resolutions obtained with different ANN train- *analysis types* ing performances. The results are grouped in six (A. to F.) pairs. Each pair correspond to the analysis done with the integrating and the peak sensing ADC simulation. Whereas particular groups represent spatial resolution:

A.) calculated with use of the most straightforward ANN approach, the GNN algorithm (see §.4.2.4),

B.) 5GNN (see §.4.2.8), full data for training and evaluation,

C.) GNN evaluated and trained with center crystal data, 3 mm from the edge,

D.) calculated with use of LNN (see §.4.2.7), full data for training and evaluation,

E.) from the GNN evaluation with center crystal data, but trained for full data set (see §.4.2.5),

F.) result of LNN trained for full data and evaluated with center crystal data (it comes after point E.).

The resolutions estimated with simulation of the peak sensing digitalization *conclusions* are up to 0.2 mm worse (Fig. 5.3). It could be that the amplitude of the signal is less stable than the area under the pulse shape. Then the ANN can create slightly worse model of the function. That is only hypothesis, but it seems that in a realistic scanner the integrating ADC is a better choice.

The most straightforward data analysis utilizing GNN algorithm produces poor results (bars pair A. at Fig. 5.3). A slight improvement is obtained by 5GNN test (see §.4.2.8 and column B. at Fig. 5.3). The resolution is improved for about
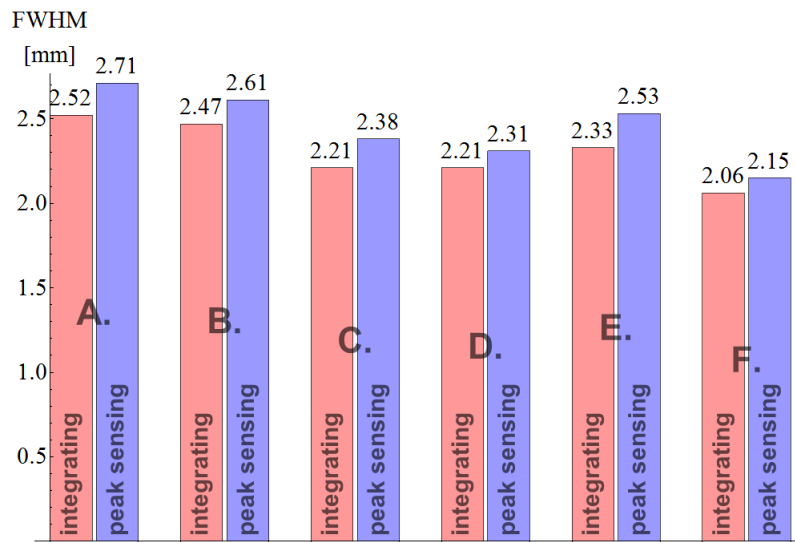
Figure 5.3: *Spatial resolution acquired for different training performances and two digitalization simulations with a PMT based detector. Bars are grouped in six pairs from A. to F. The pair shows the difference between integrating and peak sensing ADC approach results. Whereas groups are explained in the text.*
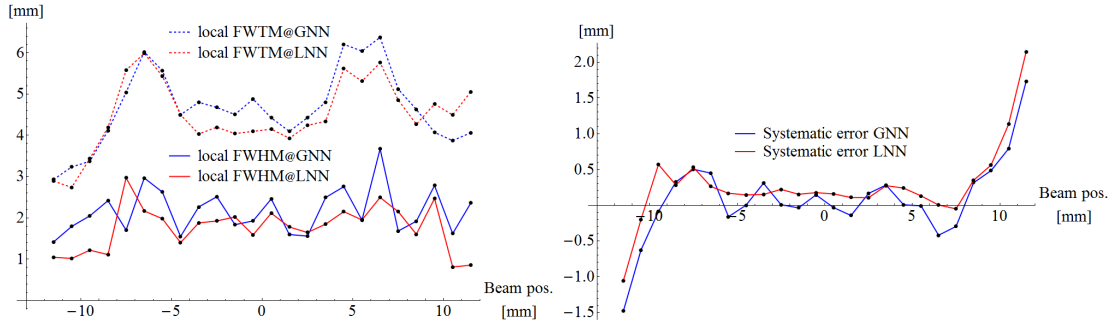
Figure 5.4: *Local spatial resolution and systematic error of the GNN and LNN evaluation.*

0.3 mm if the data set for training and evaluating doesn't include events with 3 mm of the edge (column C.). That shouldn't be surprising since the active area of the light sensor is significantly smaller than the scintillation crystal. However similar result is obtained with LNN training approach with full data set. The most optimal result is reached if the center crystal part data are used to test with GNN and LNN trained with full data set (columns E. and F.). Thus the destructive influence of the edge effect is excluded.

For comparison analysis (see §.5.4) the results of integrating ADC simulation are considered since they are slightly better. Other data sets, analysed in this work, are collected in setups that employ peak sensing hardware ADC.

5.1.4   Local analysis

As is shown on Fig. 5.3, none of the training algorithm pushes the spatial resolution below 2.2 mm without manipulation of the evaluation data set (i.e choosing center part as in column F.). Therefore the local analysis of the GNN (column A.) and the LNN (column D.) algorithms is done to follow the resolution build-up process. It considers evaluation data divided on 1 mm ranges (see §.4.2.6). Local analysis of results are presented in Fig. 5.4. Calculations for the plot are done with the data from integrating ADC simulations. The resolution measured as the average of center part of the crystal is in case of GNN 2.17 ± 0.33 mm and in case of LNN 1.86 ± 0.22 mm where the error is the standard deviation of resolutions in this region. For the peak sensing ADC case these values are slightly worse. The edge effect influence has fundamental importance for the final result at full crystal length. Moreover the edges of crystal are not covered by the PMT, therefore the network can have more problems in this area.

problems   Fitting the Gaussian function to the histogram of the edge groups of evaluation data is more complicated because the data are more often spread (Fig. 5.5.D). Sometimes unknown double peak appears (Fig. 5.5.C). The reason of this double peak is not understood. The edge part histogram can be easily recognized by an seriously increased systematic error (Fig. 5.4) and the characteristic asymmetry i.e. longer tail on one side and fast slope on the side of the crystal end (Fig. 5.5.B). All these cause over fitting and results close to the edge usually seems to be to small. There is also a characteristic peak in the resolution plots around 4-5 mm from the edge. It is easily recognized in FWTM plots at Fig. 5.4.
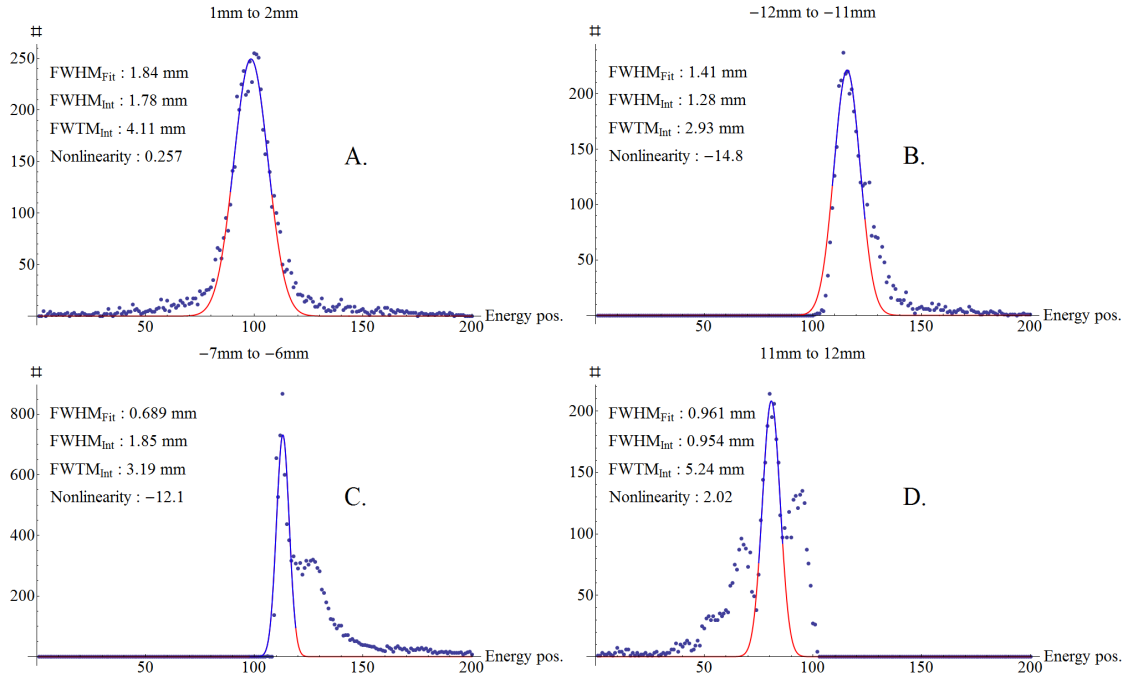
Figure 5.5: *Fitting problems. A. correct fit, B. the edge data, fast slope and tail visible, C. second peak in histogram (data from §5.2), D. data spread - over fit.*

5.2 Data of SiPM based detector - UT Delft

The main difference between the data presented in chapter 4 and the data from UT Delft are the latter are acquired using a SiPM light sensor instead of an APD. In this case also the number of pixels is different. The setup and the data acquisition are performed similar to us. Nevertheless several detector module details need to be explained, because they have a significant influence on the spatial resolution.

5.2.1 The detector and data acquisition description

The detector consists of a 4×4 SiPM pixels array 3035G16 from [SensL], coupled to a $13.2 \times 13.2 \times 10\,\mathrm{mm}^3$ monolithic LYSO (Fig. 5.6) with optically polished surfaces [CPhotonics]. The $13.2 \times 13.2\,\mathrm{mm}$ crystal surface is coupled to the light sensor active area using the Sylgard 527 gel [DowCorning1]. The other faces of the crystal are covered with a highly reflective PTFE-based material [Spectralon]. The SiPM pixels are mounted onto a $550\,\mu\mathrm{m}$ thick white float glass substrate using flip chip technology [SensL]. The 16 silicon dies are mounted at a pitch of $3.3\,\mathrm{mm}$. Each pixel has an active area of $2.85 \times 2.85\,\mathrm{mm}$, made up of 3640 Geiger-mode avalanche photodiodes as microcells. The SiPM array is operated at the manufacturer - specified bias voltage of $29.3\,\mathrm{V}$, exceeding the breakdown voltage by $2.0\,\mathrm{V}$ corresponding to a gain of $\sim 10^6$. The data is collected by irradiating the detector with $511\,\mathrm{keV}$ photons at a series of known positions and angles of incidence on the crystal front surface (front-side readout FSR) [Schaart2009]. At each position and angle, the light distributions of reference events are recorded.

Measurements are performed using the setup described in detail in [Maas2009], while the general idea can be found in §3. Briefly, the detector is contained in a
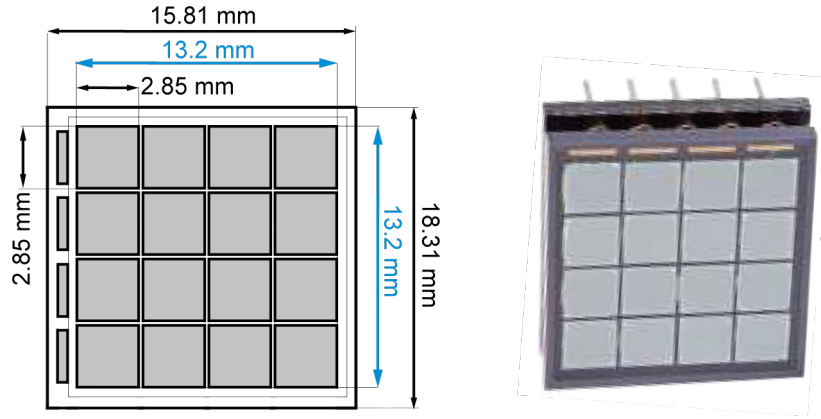
Figure 5.6: *SiPM light detector. Left) scheme of the dimensions of SiPM, right) the SiPM from [SensL]. The data set is obtained with the earlier version of shown SiPM [Schaart2009], however the pixel geometry is the same.*

temperature-controlled box and can be irradiated at different positions and angles of incidence with a $\sim 0.64\,\text{mm}$ diameter test beam of annihilation photons, defined by placing the detector close to a $0.5\,\text{mm}$ diameter ^{22}Na source and operating it in coincidence with a collimated BGO detector placed on the opposite side of the source. The SiPM signals are preamplified using a 16-channel readout board designed to minimize nonlinearity due to SiPM impedance variations. The design and characteristics of these preamplifiers have been described in [Seifert2008]. The preamplified SiPM pulses are shaped and their pulse heights digitized using a multichannel data acquisition system [Maas2009]. In parallel, a trigger signal was generated by adding the 16 SiPM signals by means of a fast summing amplifier on the preamplifier board. All measurements were conducted at $\sim 24°C$ [Schaart2009]. Data sets consist a full raster scan done with the $0.25\,\text{mm}$ step at angles $0°, 15°, 30°, 45°$.

5.2.2 Training process optimization

The same number of events is registered at each beam position. On this reason, there is no possibility to draw the count rate plot in order to check and determine the exact crystal edges. However, the scanning area covers whole crystal surface.

Several ANN training and evaluation performances (see §.4.2) are tried to optimise and study the resolution estimation process. The most significant results are summarised in Table 5.1. The resolutions in both horizontal x and vertical y direction at all four beam incidence angles are evaluated. Resolutions between 2.7 and 3.4 mm, dependently on the beam angle, are found by simple training and evaluating the full data with GNN and LNN according to the general rules explained earlier (see §.4.2 and Fig. 4.9). To diminish the edge region deteriorating influence, the data for evaluation and training are selected from the center crystal part with omitting 1.5-2 mm or 2-3 mm (in given x, y or both xy directions). The area removed is slightly different for each angle due to enlarging scanning range during beam rotation in horizontal direction (see §.4.1.5). It covers from $(-6.5 - 6.5\,\text{mm})$ for perpendicular beam to $(-9.2 - 9.2\,\text{mm})$ at $45°$ angle.

Tests are done with the assumption that the evaluation data should be lower
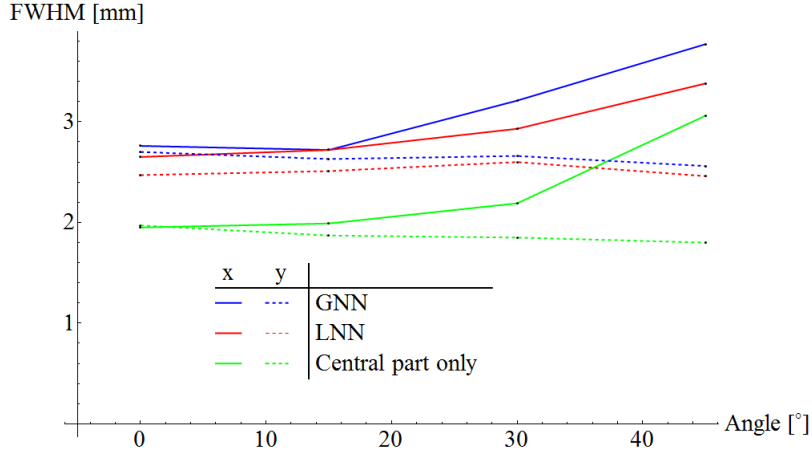
Figure 5.7: *SiPM spatial resolution results at x and y direction. Different ANN approaches: GNN, LNN, and the last, GNN evaluated with central part of data only (4 positions, i.e. 2 mm from the edges).*

Table 5.1: *Performances of ANN training process. Explanation in text.*

Nb	Edge cut in evaluation data set [mm]	Cut in GNN training data set [mm]	Angle 0°		Angle 15°		Angle 30°		Angle 45°	
			GNN	LNN	GNN	LNN	GNN	LNN	GNN	LNN
			x direction							
1.	0	0	2.76	2.65	2.72	2.72	3.21	2.93	3.77	3.38
2.	1.5-2 *x*	0	2.28	2.36	2.29	2.33	3.63	2.78	3.62	3.38
3.		1.5-2	2.51	2.34	2.51	2.15	2.86	2.49	3.69	4.39
4.	2-3 *x*	0	2.41	2.60	2.52	2.36	2.95	3.31	3.06	3.56
5.		1.5-2	2.01	2.19	1.99	2.51	2.22	2.57	3.08	3.74
6.		2-3	2.44	2.19	2.34	2.31	2.62	2.84	3.47	3.61
7.	2-3 *xy*	0	2.37	2.59	2.52	2.34	2.92	3.30	3.06	3.55
8.		1.5-2	1.95	2.14	1.99	2.09	2.19	2.68	3.07	3.88
9.		2-3	2.39	2.15	2.34	2.48	2.59	2.83	3.47	3.6
			y direction, angle should have no influence							
11.	0	0	2.70	2.47	2.63	2.51	2.66	2.60	2.56	2.46
12.	1.5 *y*	0	2.34	2.24	2.20	2.26	2.15	2.27	2.01	2.10
13.		1.5-2	2.29	2.44	2.43	2.06	2.46	2.11	2.46	1.98
14.	2.5 *y*	0	2.45	2.41	2.31	2.45	2.26	2.4	2.15	2.24
15.		1.5-2	2.00	2.20	1.92	2.32	1.93	2.35	1.88	2.16
16.		2-3	2.13	2.24	2.37	1.96	2.36	3.1	2.36	3.06
17.	*xy* 2.5	0	2.38	2.34	2.26	2.36	2.18	2.29	2.12	2.21
18.		1.5-2	1.97	2.16	1.87	2.26	1.85	2.30	1.80	1.92
19.		2-3	2.14	2.71	2.35	1.91	2.31	3.00	2.29	2.82

or at least the same range as the training set. It is found that diminishing the LNN training set doesn't significantly enhance the results, therefore in all cases presented in Table 5.1 LNN is trained with the full crystal surface. On the other hand the best resolutions are estimated with use of GNN trained with 1.5-2 mm edge cut set. Whereas the best option for evaluation is to cut 2.5-3 mm at least in analysed direction (i.e. horizontal x, vertical y or in both). Due to these operation the considered resolution is better then, the acquired with the simplest ANN algorithm, of around 1 mm (Fig. 5.7).

In case of the beam rotating direction - x the resolution stays reasonably constant up to 30° where slight FWHM degradation is registered. For angle 45° resolution is worse for around 1 mm. In y direction as expected, the resolution is more stable over the angle and in the best case is below 2 mm. Other tried evaluation ideas (i.e. selection of data more from central part in GNN or LNN training data) doesn't yield constant or significant enhancement.

5.2.3 Comparison of the results obtained with SiPM and APD for gamma rays arriving under an angle

Fig. 5.8 shows a comparison between the results from SiPM presented in Fig. 5.7, and from APDs as in Fig. 4.10. Although the resolution is in general slightly better for the APD, the best resolutions obtained are nearly the same (Fig. 5.8). Results starts to differ above the 30°. All operations with the data set are done to diminish the influence of the edges on the spatial resolution. In that way the final result is expected to be closer to obtained in the center of the crystal (third row of Fig. 5.8. The fact the SiPM detector has a smaller crystal surface than the APD detector crystal block, can be the reason of the worse resolution even in LNN approach (first two rows of Fig. 5.8). The resolution deteriorating edge range covers a bigger fraction of the crystal surface then in APD based detector.

Another important factor is the pixel size and pixel number under given crystal contact area. Their influences are difficult to assess for the moment. In both experiments results include the beam size which is in case of SiPM based detector ~ 0.64 mm and for ADP ~ 1.09 mm.

The rotation mechanism is similar. For APD based detector the source is fixed on the front of the box and rotate with it (Fig. 4.3). Therefore during scanning the distance between the source and the tested monolithic block detector is constant, by the cost of the distance between a source and the reference detector (see §.3.2.2). In the SiPM measurements, care was taken to keep the distance between the source and the detector under investigation constant for different angles of incidence. Specifically, the source and coincidence PMT were kept at the same position in the laboratory coordinate system. The same was true for the axis of rotation, which also coincided with the front surface of the crystal under investigation, so that distance between the source and the point at which the beam hits the crystal front surface is independent of the angle of incidence. The translation stages used to move the crystal through the beam were mounted on top of the rotation stage, so that the source-crystal distance remained the same for all (x,y) irradiation positions. Theoretically the beam size in both experiments should be rather stable over the incidence angles.
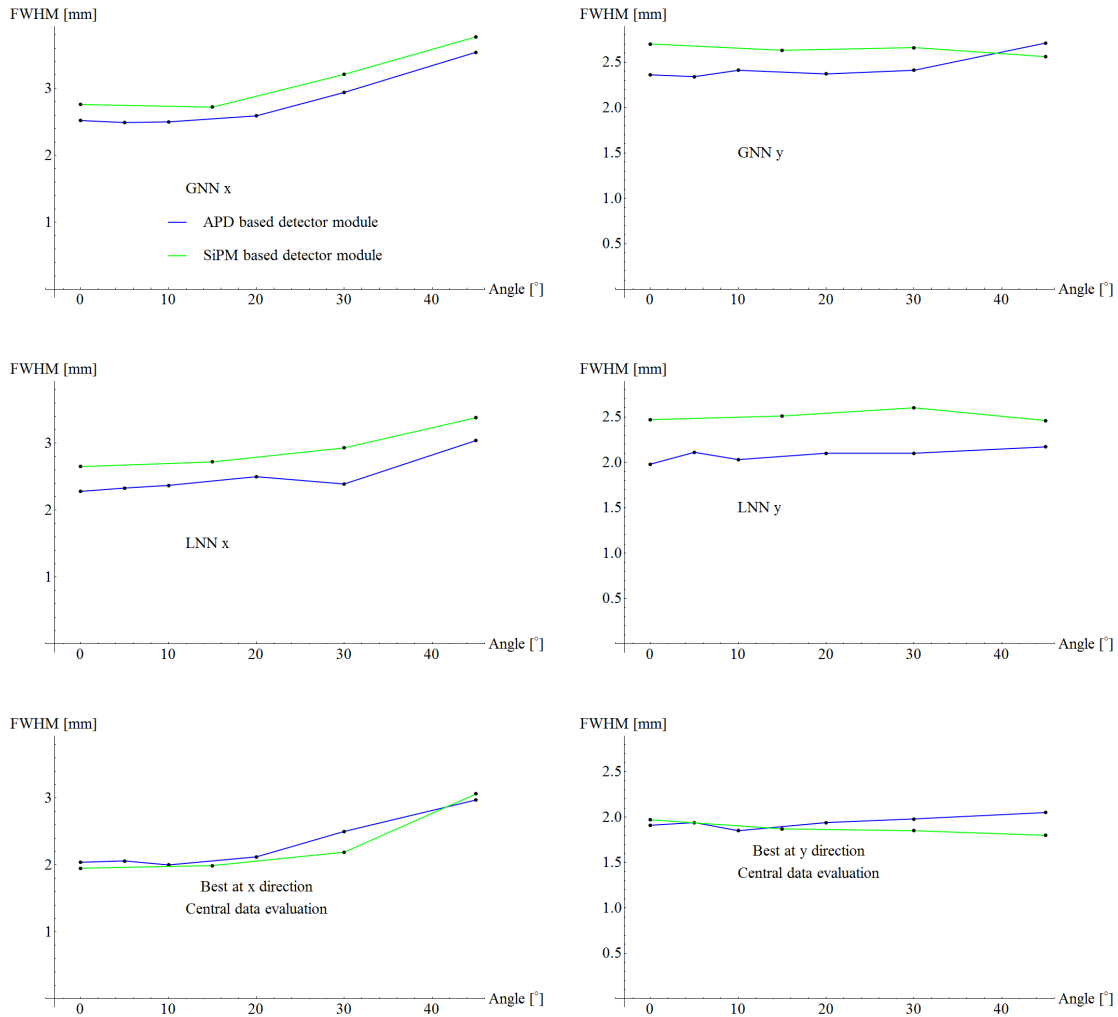
Figure 5.8: *Spatial resolution comparison between APD based and SiPM based monolithic block detectors for different angles and ANN solutions.*
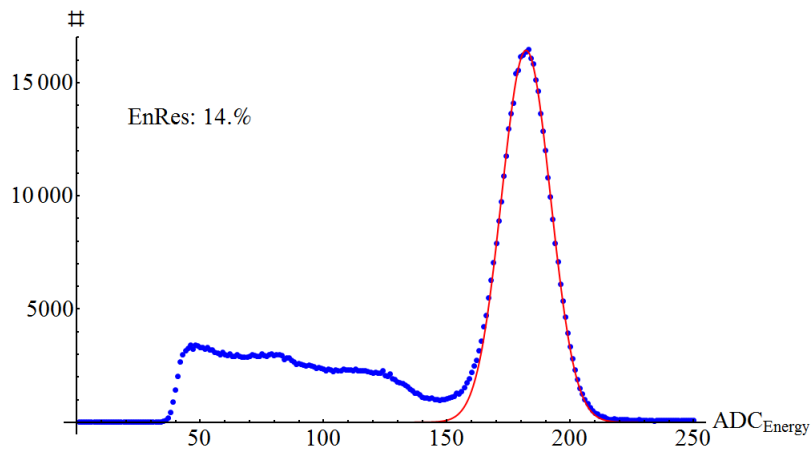
Figure 5.9: *Pulse height spectrum of the SiPM based detector measured by irradiating the entire detector with 511 keV photons.*

89

5.2.4 Energy resolution

Fig. 5.9 shows the energy spectrum. The plot is made for a perpendicular beam taking into account all beam positions. The energy resolution equals 14% FWHM at 511 keV [Schaart2009]. As expected it is stable over the rotation angle.

5.2.5 Local information extraction

Figure 5.10 shows the result of local analysis of GNN and LNN (see §.4.2.7). Both algorithms GNN and LNN give similar resolution at the center of the crystal (beam positions between -2 and 2 mm). Considering x direction the FWHM from LNN algorithm starts to increase around $3 - 4$ mm from the edge up to $2 - 3$ mm. Then it diminishes because of the crystal end. The effect repeats in y direction. In the SiPM data, the FWTM is sometimes larger due to presence of a second peak in some of the differences histograms (Fig. 5.5.C). Systematic error gets worse closer to the edges.
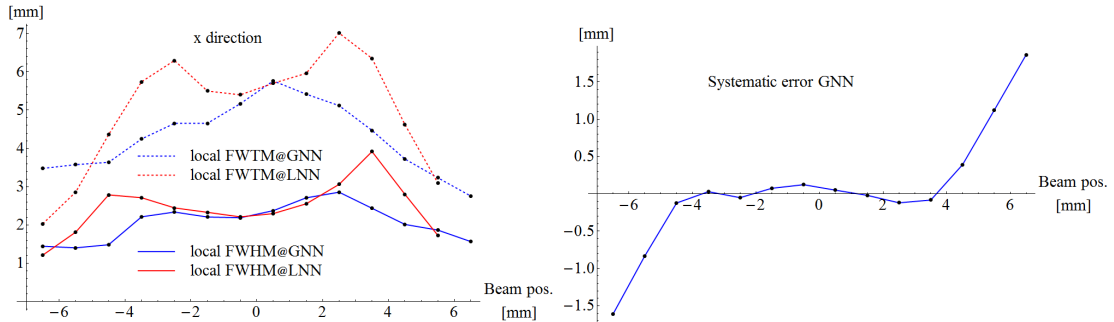
Figure 5.10: *Local spatial resolution and systematic error for perpendicular beam at x direction.*

5.2.6 ANN comparison with nearest neighbours method

The group from UT Delft uses a nearest neighbours statistical algorithm instead ANN for resolution estimation algorithm. The method is explained in [Maas2009]. In brief the data acquisition and setup are based on the same idea as the setup with APD based detector. The entry point of an unknown annihilation photon is estimated by calculating the sum-of-squares differences of its light distribution with those of all events in the reference set. A subset of the reference data consisting of L closest matches (nearest neighbours) is selected, and the most frequently occurring entry point within this subset is assigned to the unknown event (Fig. 5.11).

At Fig. 5.12.*Left* the solid line shows the FWHM of the detector spatial response in the x-direction as a function of x. At each x, all results obtained between x - 0.5 mm and $x + 0.5$ mm (e.i. over the entire length of the crystal in the y-direction) were combined into a 2D error histogram in order to minimize statistical fluctuations. The same calculations are done in y direction. Only perpendicular beam is considered. In this measurement the source is closer to the detector box, because the the source moving axes is parallel to the box surface (i.e. no space for rotation is needed as in angular scans). Thus the beam size is ~ 0.54 mm.
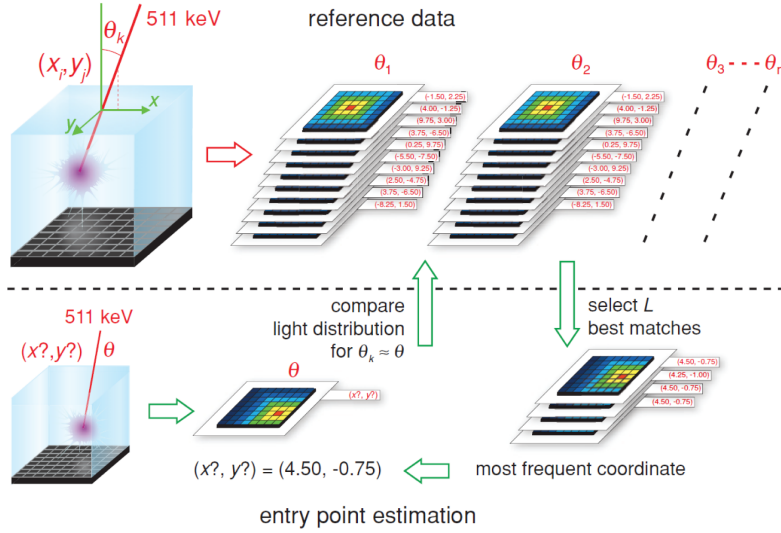
Figure 5.11: *Schematic representation of the nearest-neighbour algorithm used to estimate the entry point (x, y) of the annihilation photon from the scintillation light distribution measured by the SiPM array [Schaart2009].*
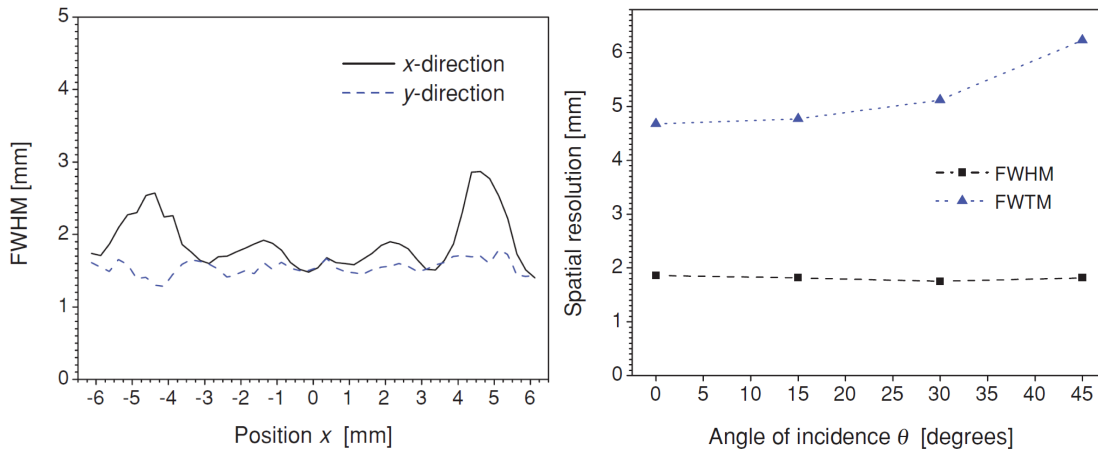
Figure 5.12: *Nearest neighbourhoods method. **Left**.)FWHM of the detector spatial response in the x-direction (solid black curve) and inthe y-direction (dashed blue curve), as a function of x. Data are measured at perpendicular incidence, using an ∼ 0.54 mm FWHM diameter test beam and with 1000 reference events and L = 750; **Right**.) FWHM and FWTM of the average detector spatial response in the x-direction, measured as a function of the angle of incidence using an ∼ 0.64 mm FWHM diameter test beam. Data are obtained with 250 reference events and L = 1000 [Schaart2009].*

Edge effect appears in both methods: nearest neighbours or ANN. In the first approach (Fig. 5.12.Left) the spatial resolution fluctuations starts ∼ 3 − 4 mm from the crystal edge. In case of ANN, this effect appears closer to the center part (Fig. 5.10).

The nearest neighbours analysis (Fig. 5.12.Right) gives much stable, and significantly smaller spatial resolution, than results of ANN Fig. 5.7. That is when full data set is analysed. The near neighbours give resolution in average 1.86 mm, while the LNN gives (i.e. for x direction of perpendicular beam) 2.65 mm FWHM. Just selecting the center part of data for ANN evaluating allows to push the resolution below 2 mm (except data acquired at angle 45° in x direction) as shown at
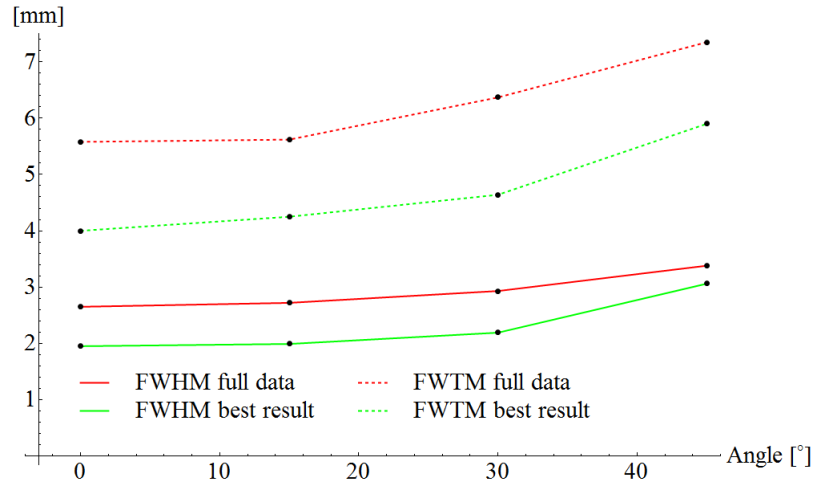
Figure 5.13: *FWHM and FWTM of the ANN analysis for x direction. Best result is obtained by ANN evaluation with center part of the crystal.*

Fig. 5.13.

The average FWTM value at x direction for nearest neighbours equals 4.68 mm. That can be locally compared with the ANN results of perpendicular beam at Fig. 5.10. Generally the FWTM from the ANN calculations for a given incidence angle is $\sim 1\,\text{mm}$ worse then for the nearest neighbours (Fig. 5.12.Right). Again the best results in FWTM from ANN is nearly the same or even slightly better then this calculated with nearest neighbours (Fig. 5.13). On the other hand, the FWTM is easy to overfit due to the noise (see §.4.2.1). Since the setup for SiPM and APD detector studies are different, the noise level is also different. It is difficult to compare the noise influence for FWTM in both analysis. Therefore the FWTM comparison may have no sense.

There is a question of the algorithm application, because the ANN requires less time for image reconstruction then the nearest neighbours method, but by cost of accuracy as it is shown.

5.2.7 Pixels sensitivity uniformity

The SiPM pixels scintillation light response is in general uniform. However, pixels number 11 and 13 seems to have a lower sensitivity. Fig. 5.14 shows the standard deviation of each pixel over all beam positions at perpendicular beam. The values between pixels should be relatively uniform if pixels generate the same amplitudes dependently on the number of incoming photons. Two pixels, eleventh and especially thirteenth, seem to significantly diverge from rest.

These problems could explain small asymmetry in FWHM maximum over the horizontal direction on Fig. 5.12.left and 5.10. Nevertheless statistic algorithms usually can handle such problems quite well. Acquired resolutions are competitive with existing pixelated detector approaches.
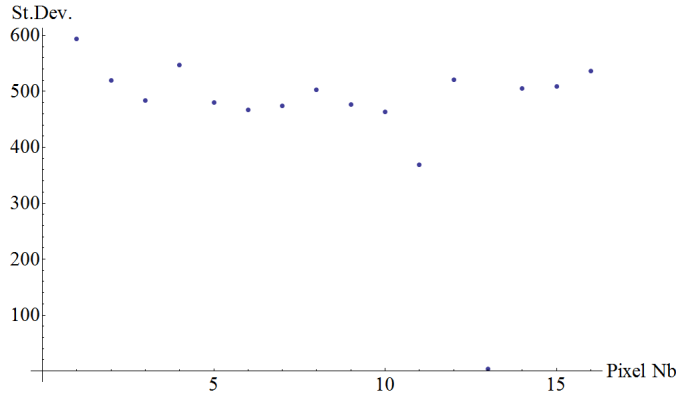
Figure 5.14: *Standard deviation of pixel values over the whole crystal surface of perpendicular beam positions.*

5.3 The PMT based detector with integrated electronics

The third analysed data set is acquired also with a PMT based detector and a perpendicular beam full raster scan. The whole electronics is integrated in a box manufactured by the group from Forschungszentrum Jülich. The experiment is done to test the electronic box for future SiPM based detector application.

5.3.1 The detector and data acquisition description

The detector module consists of a $20 \times 20 \times 10\,\mathrm{mm}^3$ teflon wrapped monolithic LSO crystal, coupled to 64 multi-channel Hamamatsu R7600-00-M64 PMT [Hamamatsu2006a] by the optical grease [DowCorning]. The source is placed on the front of the tube. The read-out electronics scheme is shown in the Fig. 5.15 [Buchacher2010]. The detector box is placed on the source moving XYΩ platform also used in the measurement of the APD based detector (see §.3.2.2). Two computers are used to control the setup, read and save the data. First is responsible for the moving platform. The second PC controls the electronics and does the data registration. The read-out control programs are written in $C++$ in FZJ. It is integrated with the LabView XY control program in order to save incidence beam positions.
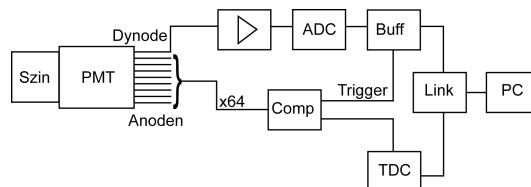
Figure 5.15: *Block diagram of the readout electronics [Buchacher2010].*

5.3.2 Data set analysis

Several measurements are done. For analysis a full raster scan of perpendicular beams is chosen. The resolution for central data (i.e. 3 mm from the edges) is found $\sim 2.2\,\mathrm{mm}$ in x and y direction. The result is acquired with the LNN approach.
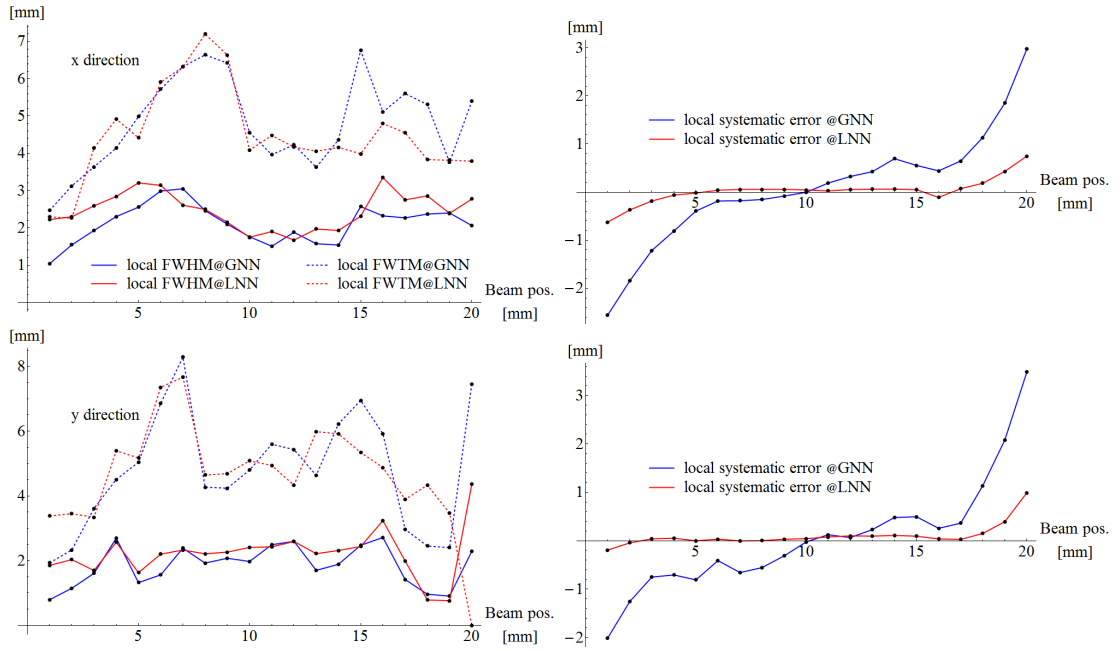
Figure 5.16: *Local FWHM, FWTM and systematic error in horizontal x and vertical y analysis.*

During the measurement, after optimised geometrical setup arrangement, quite large number of $\sim 12 - 14\%$ random fraction is registered. It is mainly caused by relatively big 120 ns coincidence window set in electronic design. However as it is discussed in §4.3.1, ANN should be able to give reasonable results even with such data set.

Fig. 5.17 shows the energy spectrum. It is not satisfying. Obviously there is something wrong with the data set. Therefore resolution obtained with this setup could be much better. The measurement takes around 20 h dependently on the coincidence rate, scanning step and scanning range. In such long scanning the problem with loading initialization parameters (e.g. PMT high voltage) is found. This communication problem causes that most of measurements were not useful for analysis. Because of the problems it is difficult to find good conclusions from presented analysis.
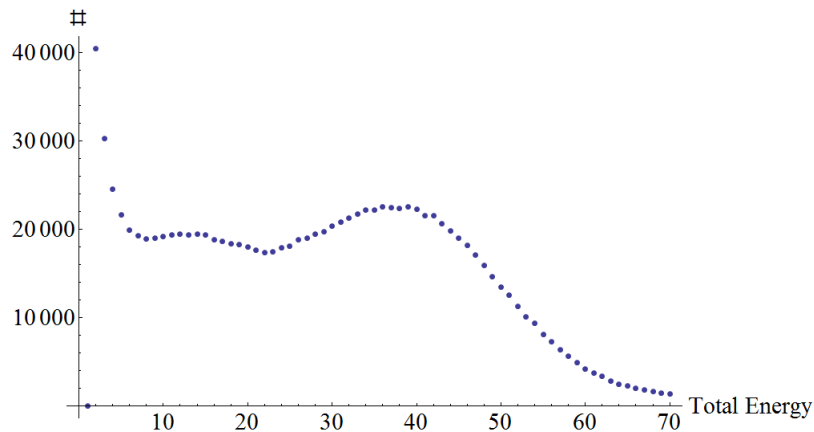
Figure 5.17: *Energy resolution.*

5.4 Conclusions of the comparison of the data acquired in the different experiments

The same ANN algorithm is applied for the data acquired from the monolithic block detectors based on three light sensors: the APD, the PMT and the SiPM. The aim was to try to compare spatial resolutions. The general design of the experiments is similar. The data are acquired from scanning the full crystal surface with a perpendicular 511 keV beam, except for the data of the PMT based detector from UTSC, where a single line scan is employed. In all cases the scintillator was LSO or LYSO, which is very similar to LSO.

However, there also are significant differences, that makes a comparison really difficult. The most important is the crystal surface size. It changes between $25.5 \times 25.5\,\text{mm}^2$ for a first PMT based detector, $20 \times 20\,\text{mm}^2$ for second PMT and APD, until the smallest, $13.2 \times 13.2\,\text{mm}^2$ for SIPM. Since the light sensors are different also the active area and the pixels size are not the same (Table 5.2). The approximated beam size ranges between 0.6 mm and 1.1 mm (Table 5.2) and they are not subtracted from the result resolutions.

Figure 5.18 shows the comparison between the spatial resolutions obtained in x direction analysis. Three results are considered. First, the FWHM from basic GNN and from LNN, evaluated with all beam position data. Both networks are trained also with full data. These resolutions consist the biggest influence of edge effect. Efforts to diminish the deteriorating influence of the crystals border range are summarised in the third columns in Fig. 5.18, the GNNc. The idea is to cut the evaluation data set at 3 mm from the edge and eventually GNN training set at 1-2 mm. In analogy, the same studies are done for y direction at Fig. 5.19. The plot doesn't contain results from UTSC PMT based detector, because the data are collected in horizontal single line scan only. *Fig. 5.18-5.19*

The best results are around 2 mm FWHM, in all cases similar. However, there is some spread if edges are considered. The basic GNN evaluation is improved up to 0.5 mm by employing LNN algorithm. In case of SiPM the spread between LNN result and FWHM evaluated in the center is much bigger than for other analysed detectors.

There can be a few potential answer for such spread in SiPM results. One is *SiPM*

Table 5.2: *Comparison of measurements parameters for different detectors.*

	APD (VUB)	PMT (UTSC)	PMT (VUB/FZJ)	SiPM (UT Delft)
Total active area [mm²]	6.4×12.8* 81.92*	18.1×18.1 327.61	18.1×18.1 327.61	13.4×13.4 179.56
Pixel size [mm²] Array	1.6×1.6 4×8*	2×2 8×8	2×2 8×8	2.85×2.85 4×4
Crystal surface [mm²]	20×20	25.5×25.5	20×20	13.2×13.2
Beam size [mm]	~ 1.09	~ 0.6	~ 1.09	~ 0.64
Scanning step [mm]	0.5	0.25	0.5	0.25

* *considering single APD module*
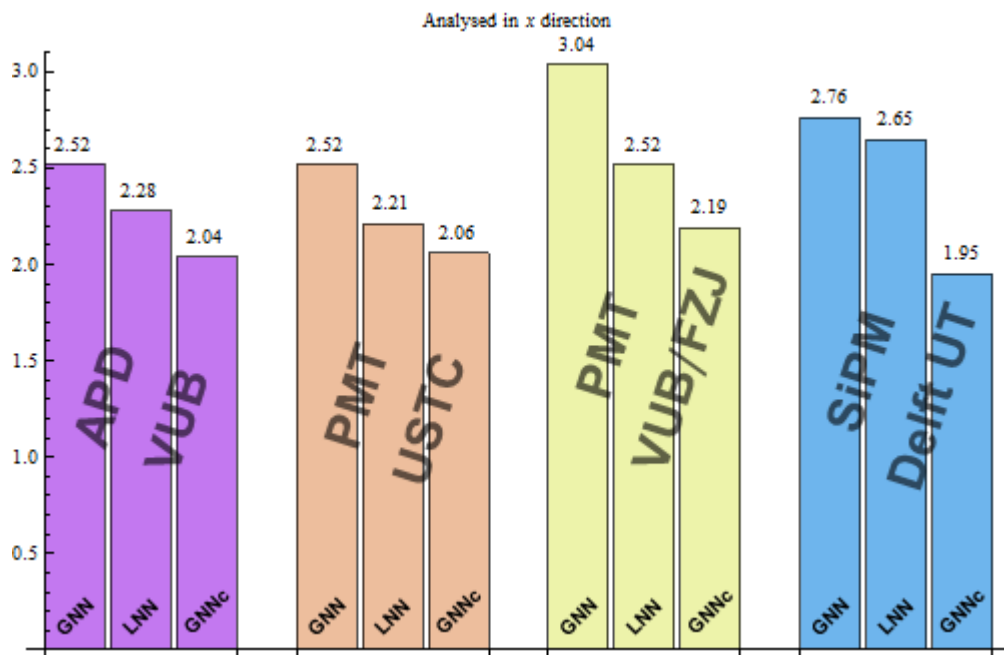
Figure 5.18: *Spatial resolution results comparison in* **x direction** *at perpendicular beam. APD data:full raster, x step 0.5 mm; PMT data USTC: single line scan, x step 0.25 mm; PMT with the electronics box from FZJ: Full raster, x step 0.5 mm; SiPM data: full raster scan, x step 0.25 mm. Results of three approaches are presented: GNN, LNN and the GNNc, that is from the central part of the crystal, minimum 3 mm from the edges.*
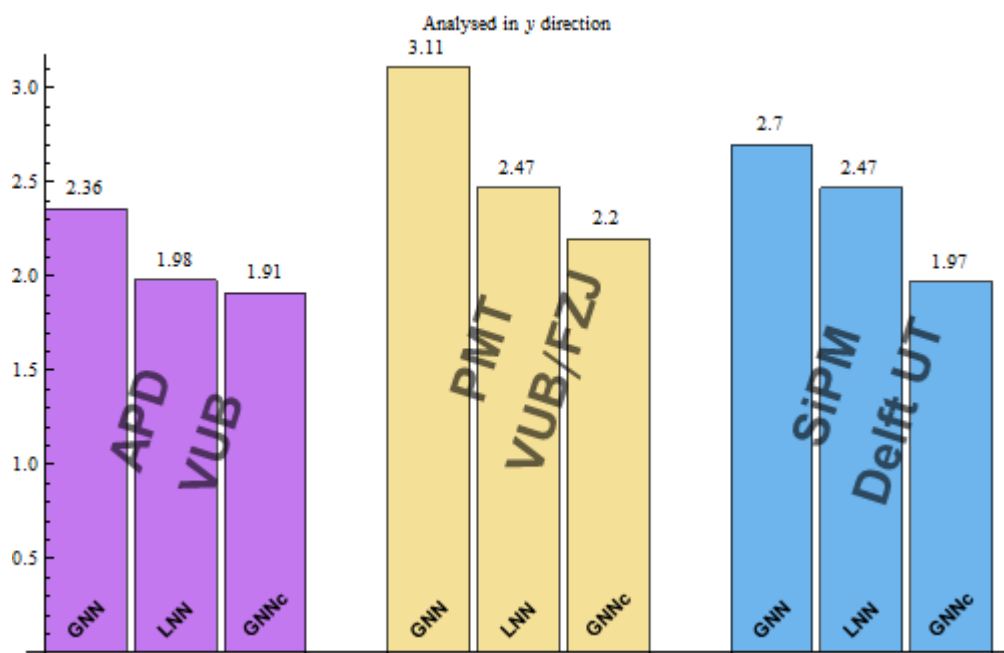
Figure 5.19: *Spatial resolution results comparison in* **y direction** *at perpendicular beam. APD data:full raster, y step 0.5 mm; PMT data USTC: single line, step y 0.25 mm; PMT with the electronics box from FZJ: Full raster, y step 0.5 mm; SiPM data: full raster scan, y step 0.25 mm. The same type of ANN performances as at Fig. 5.18 are presented.*

that the crystal surface is the smallest from all detectors, so the fraction of edge in whole crystal surface is higher then in other investigated detector modules. The pixel size in this case is the biggest, that influence is also unknown.

If compare the APD and the SiPM, the results of the APD are better, because the beam size is not subtracted. For the SiPM it is around 0.6 mm, since for the APD it is around 1.1 mm. It should also be highlighted that the optimal ANN algorithm is not yet found. This work is done to investigated a few possible approaches. Since the APD and SiPM detector have different crystal surface, it is very difficult to prove that this conclusion is fully correct.

Generally, the nearest neighbours algorithm performance is better than the neural networks. But the ANN is faster, that is also important in realistic scanner. The most important conclusion from the SiPM data analysis is that, indeed, the SiPM detector works.

PMT/UTSC

Since the PMT light sensor has better characteristics than APD, so better results were expected. For data acquisition smaller beam size was used. There was a problem during resolution estimation due to some artefacts on the error histograms. It is shown in the local analysis. From this point of view the real resolution of this detector should be better than reported. On the other side PMT suffers on terrible non linearity. In this case, the real result should be worst. A poor resolution of the PMT/UTSC detector could be also explained by big difference between active PMT surface and the crystal size, 18 mm to 25.5 mm. Because of that the comparison between APD and such PMT detector is rather impossible.

PMT VUB/FZJ

The resolution obtained with the PMT detector coupled to the readout electronics from FZJ is also much worse than expected. This detectors could be really compared, because of the use of the same size crystal. However, due to problems with adopting the electronic box to the setup at VUB, the acquired data set is not the best. It can be found for example in strange energy spectrum. Actually the problem is not fully understood. Poor results from this PMT detector doesn't prove that APD detector is better.

In case of all detectors it is shown that LNN algorithm improves the results. This is the same conclusion as in APD detector studies.

Conclusions

The most common existing PET detectors are based on a pixelated design. The evolution in PET goes in a direction of higher spatial resolution and sensitivity, such as in Brain PET, Positron Emission Mammography or small animal PET. The sensitivity can be increased by enlarging the crystal pixel length or diminishing the detector ring. However, this increases the parallax problem and reduces the spatial resolution. It can be solved by applying a solid scintillator block idea. In addition it can reduce dead zones in between the crystals pixels and thus also enhances sensitivity. Moreover, monolithic crystal blocks are less expensive to produce and easier to mount. To diminish the distance between the detector modules, a compact light sensor is required. Therefore the avalanche photo diode (APD) is used. Moreover, this device is not sensitive for magnetic fields, and can thus be easily applied in PET/MRI multi-modality. The depth of interaction (DOI) information is necessary for spatial resolution estimation. However, the reduction of the parallax error and improvement in the resolution can be done by determining the incidence point rather then the DOI. This information is extracted from the light profile registered by the APD using an artificial neural network (ANN) as machine learning algorithm. It is a fast and efficient method.

Nevertheless, to optimise the parameters of the detector and the estimation algorithm, more studies are required. One of the goals of this thesis is to study the intrinsic detector spatial resolution behaviour of a $20 \times 20 \times 10\,\mathrm{mm}^3$ monolithic Lutetium Orthosilicate (LSO) scintillator block detector based on Hamamatsu S8550 APD light sensor with applied ANN to resolution estimation. Conditions of measurements and analysis are guided by the potential conditions fluctuations in realistic scanner. The ANN robustness on the incidence beam angle, random fraction in the data, APD high voltage and temperature fluctuations are investigated. Finally the analysis of alternative light sensors in the monolithic block detector design is done. The data from 64-multichanel photomultiplier (PMT) and 16-channel Silicon Photomultiplier (SiPM) based detectors are studied individually using the same resolution estimation algorithm.

The feedforward Levenberg-Marquardt neural networks positioning algorithm is chosen, because it works very well with very ill-conditioned problems. The neural network estimates resolution relatively fast in comparison with other methods. However it requires to be trained with a data set with known incidence beam coordinates. Therefore a bench setup is build. It provides the data at the different beam angles, i.e. $0°$, $5°$, $10°$, $20°$, $30°$, $45°$. The detector is mounted in a controlled cooling system that allows to collect data at different temperatures. Measurements are done at different gains by changing the APD high voltage or temperature.

Several neural network training approaches are tested. The most straightforward is GNN, but the results estimated with this algorithm are not satisfying.

Using the LNN performance, the spatial resolution is systematically better. Nevertheless, the resolution estimated with LNN is not the best that can be squeezed from the monolithic LSO block detector. This is due to edge effects. The edge effects can be avoided by evaluating the resolution in the center of the crystal. Here, the best result is acquired. The LNN is the approach that pushes the global resolution closer to the result of the central crystal part.

For a perpendicular beam, in x direction analysis of the whole raster scan data, the resolution estimated with the GNN approach is 2.52 mm. The LNN improves the result to 2.28 mm, while 2.04 mm is the FWHM acquired at the crystal center. In y direction the resolutions are respectively 2.36 mm, 1.98 mm and 1.91 mm FWHM. The dimension of the LSO crystal used are $20 \times 20 \times 10$ mm^3. The x resolution reported for a $20 \times 10 \times 10$ mm^3 crystal by [Lemaitre2009] is slightly better, around 1.9 mm FWHM. This resolution difference could be caused by the individual pixel noise, because the x resolution is estimated from eight sums of pixels along the x direction. Since the detector used in this work employs two APD arrays, it sums two times more pixels, and also their noise. It probably influences the resolution estimation process and deteriorates the final resolution.

Generally, the biggest disadvantage of APD is its low internal gain. Therefore, it requires a low noise preamplifier. The result can also be worse if mounting the APD on the LSO crystal is not done carefully. There is a big risk that in the layer of Meltmount, micro-bubbles of air appear. Micro-bubbles scatter the scintillation light, and cause miss position of the incidence point.

To have stable parameters in the setup, it is also important to keep the APD high voltage and the temperature inside the box stable. It is shown that a few V and a few °C fluctuations have no significant influence on the ANN algorithm. It is important for the design of a realistic scanner.

The optimal neural network algorithm consist of two hidden layers, each with five neurons. The each event consisting 64 signals is transformed into 8 neural network inputs to diminish the training time. Dependently on the computer power and expecting training time, 20000-30000 events for training is enough to receive good result. More data usually doesn't give further improvements in training, but seriously increase the learning time time. Similar situation is found with the number of iterations during training. The optimal value ranges between 15-30 in case of used data sets. The scanning step is set at 0.25 mm in single line scan and at 0.5 mm in full raster scan. In earlier studies it is found that the step size 0.5 mm and below is sufficient.

Amplification calculated from relation between the APD high voltage and the photopeak position is around 90x. Hardware energy threshold is around 60 keV, calculated from known distance between the photopeak 511 keV, and high energy peak 1275 keV. Nevertheless, for ANN training only data from the photopeak are taken.

The noise is the biggest limiting factor of the spatial resolution in the applied setup. Fluctuations in the noise lead to the degradation of the energy resolution. If the scattered event is detected in the photopeak energy window it also deteriorates the spatial resolution. For the noise, the most critical noise is probably in the part consisting of the APD and the Cremat pre-amplifier. Any noise/cross-talk will get amplified by the Cremat pre-amplifier and the amplifier. Because the pre-amplifiers are close to the APD and in a box, their pick-up noise should be rather

small. The APD introduces its own dark current and ENF noise, both dependent of the high voltage and temperature. The Cremat amplifier itself will also add noise. The second source of noise is any pickup on the long cable from the box to the amplifier. Unfortunately the setup doesn't utilise differential signals, so this noise can not be cancelled. By avoiding this problems the exaggerated ENC (around $1800 \, e^-$) would be probably significantly lower. The newly developed SiPMs allow a much larger gain without pre-amplifiers and therefore could significantly improve the resolution that can be achieved with such a system.

Finally the data from three alternative detectors are analysed. These are data from a PMT detector from UTSC, SiPM data set from UT Delft, and PMT data acquired in the same bench setup as APD detector, but with an integrating electronics box manufactured in FZ Jülich. The best results acquired from each of the detector are very similar, around 2 mm FWHM in both directions. However that is usually the resolution in the center of the crystal, around 3 mm from the edge. LNN results change to 2.28 for APD, 2.21 for UTSC PMT, 2.65 for SiPM and 2.52 mm FWHM for the second PMT.

Generally, the setups are based on the same idea and detector design. The significant difference, besides the light sensor type, is the crystal surface. It changes between $25.5 \times 25.5 \times$ mm^2 for a first PMT based detector, 13.2×13.2 mm^2 for SiPM and 20×20 mm^2 for a second PMT and APD. Since the crystal size has a major influence on the spatial resolution, it is very difficult to conclude anything from a comparison between detectors.

Considering the light sensor performance, better results from the PMTs were expected, especially from the data set of second PMT based detector, where the same crystal size was used. However, due to problems with adopting the FZJ electronics readout to our setup, the data acquired are not the best. These results are worse than the PMT data from UTSC. But the difference between the crystal size from the UTSC detector and from VUB is significant. Moreover, the UTSC light detector does not fully cover the crystal. So, also the sensitive area is different.

The SiPM has the best resolution in the center of the crystal. It is strange that the overall resolution is so different. The edges of the crystal could be estimated not correctly during the training data set selection. On the other hand, the edge effects cover a bigger fraction of the crystal surface since it is smaller then in other cases. Based on the nearest neighbours analysis done by the group from UT Delft, the resolution is 1.86 mm FWHM for full crystal surface data. The results from ANN seems to be worse. However, this work presents the study of several ANN approaches. More investigation on the ANN can help to find even better ANN performance. The most important conclusion from SiPM studies is that this quite new detector is indeed working very well.

The beam width influence the network training process. Therefore it shouldn't be to big as it was checked in simulations in other works. The beam size used in SiPM and PMT from UTSC data acquisition is set for around 0.6 mm. In rest two data set it is around 1.1 mm. Also the pixel size differs between 1.6×1.6 mm^2 for APD, 2×2 mm^2 for both PMTs and 2.85×2.85 mm^2 for SiPM. The influence of this factors was not studied.

Future outlook

Presented work analyse the monolithic block detectors based on APD light sensor. It is a compact and a magnetic field robust device. This is important in developing PET/MRI dual-modality. This multi-modality technique is usually compared with PET/CT as a competitor. Both methods provide PET information intrinsically aligned to an anatomical information from from CT or MRI, without the use of external markers or internal landmark. The PET/CT is simpler and cheaper due to absence of strong magnetic field. However it requires additive radiation dose in the body. From the other had the PET/MRI works better in soft tissue and brain applications.

Joined efforts of the CIEMAT from Madrid/Spain, the Forschungzentrum Jülich Germany and the VUB team, in the framework of Crystal Clear Collaboration (CCC), the BrainPET project is designed. The scanner is MRI compatible as to be in future utilised in PET/MRI modality. The Monte Carlo simulations and experimental work out the monolithic crystal block APD based detector is introduced in Brain PET project.

The basic detector modules idea consists of a dual layer of trapezoidal LSO blocks to enhance the system sensitivity. As a light sensor Hamamatsu S8550 APD side by side of the detector is used. The complete scanner is build of 4 detector rings of $\varnothing 40\,cm$, each with 52 detector modules. The spatial resolution estimating algorithm is based on extraction of photon interaction site by using ANN as it is developed by the VUB-group. The training data are collected by moving the source close to the detector ring in coincidence with opposite detector that ensure narrow beam. This way whole crystal surface is scanned. Different detector configurations are considered to determine the all potential incidence beam angles. The present detector spatial resolution is 2.4 mm FWHM, acquired with a 0.25 mm diameter point source with 1.0 MBq nominal activity of positron emitter ^{22}Na. The energy resolutions at 511 keV is between 13.1% and 14.1% FWHM [Mendes2009, Mendes2007]. The project is still under development.

Since the SiPM show better characteristics as a light sensor and works well as it is shown also in this work, they can push out the APD soon. In combination with monolithic blocks and ANN algorithm it seems to be very promising PET detector.

Existing commercial whole body PET scanners offers resolution of range 4-9 mm FWHM. Considering this potential application the monolithic crystal block approach looks very promising. More studies on ANN algorithms and the solution for the edge effects can effect in better spatial resolution for the monolithic block detector.

There is also several interesting studies directions on the level of the detector itself. Since summing rows and columns appears to work well, it might be interest-

ing to investigate if detector calibration could be done with a line source instead of a pencil beam, as this might perhaps help to speed up the calibration procedure. Other possibility that could increase the training procedure speed could be found by investigating the symmetry issues in the ring of the detectors.

Very helpful could be diminishing the influence of edge effects. Some studies is already done, but this problem is still not fully understood. Some simulations, as for example mirroring effect of the edges, could give some ideas.

The influence of the pixel size is also not yet understood. It could be interesting, but also cheaper to test it first in simulations. It is quite difficult to make comparison of detectors with different pixel sizes. It is mainly due to different active areas and crystal dimensions.

<div style="text-align: right;">

Appendix

</div>

The issue of "bad" coincidences in the training and evaluation sample

As it is written in chapter 4.1.3, the ^{22}Na source emits in 90% of the decays, two 511 keV photons and in addition a high energy gamma ray of 1275 keV. In 10% of the decays, only the gammas of 1275 keV are emitted. That can cause false coincidence detection or false energy deposit in the detector. It is possible to roughly estimate the influence of false coincidence caused by 3rd gamma.

Lets consider all possible coincidences between the detectors in the setup. The true coincidence L+L is registered, when both annihilation photons are detected and the high energy photon is not (Fig. I). There are two the most probable false coincidences. The first, L+H happens when the LSO detects one of 511 keV and the BGO detects the high energy gamma. The second, LH+L happens when both annihilation photons are detected, but in the LSO also 3rd gamma is registered. Next type of coincidence, H+L considers the situation reversed to L+H. In this case one of the 511 keV misses the LSO detector, but instead 1275 keV is detected. This events can only happen when the source is on the edge. It is because the geometric arrangement of the detector assure a very narrow beam, so in the most of cases the annihilation detected in the BGO is also detected in LSO. Another type of coincidences happens, when beside the both annihilation photons detection, the BGO registers also high energy photon, L+LH. Since the energy deposited in the LSO (not BGO) is the object of interest, this event is considered as a good. Nevertheless the fraction of this events is negligible.

The rate of the coincidences is calculated from the Eq. 1.7 in chapter 1.4.2. The object attenuation is considered as 0 so the element $e^{-\mu_o \cdot l_o} = 1$. The activity of the ^{22}Na is 15 μCi (see §.4.1.3). The geometric efficiency ε_{geom} considers approximation
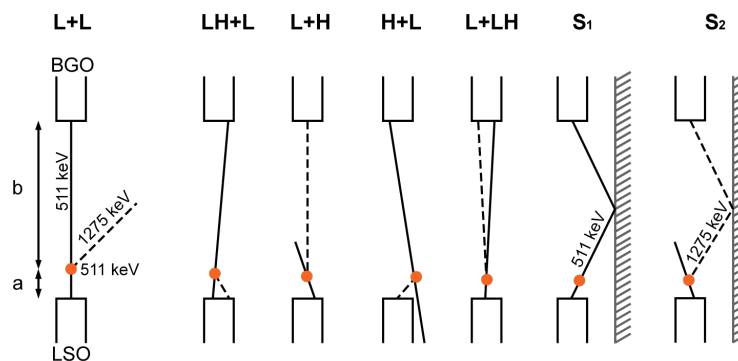
Figure I: *All possible coincidences in the setup.*

of the solid angle. It is calculated as the fraction of the considered detector surface that see the gamma ray.

$$\Omega = \frac{s}{4\Pi r^2} \tag{I}$$

The surface s in both cases, the LSO and the BGO, is $2\,\text{cm}^2$. But the total sphere $4\Pi r^2$ depends on the distances r between detector and the source. For LSO it is $1.4\,\text{cm}$, whereas for PMT it is $110\,\text{cm}$.

The intrinsic detector efficiency in equation 1.7 is considered separately for LSO and BGO. They depend on the crystal type and length. The length l of LSO crystal is $1\,\text{cm}$, and $5\,\text{cm}$ for BGO. The linear attenuation coefficient is taken from database of Physical Measurements Laboratory - National Institute of Standards and Technology [NIST]. The database program finds a total attenuation of the crystal for a given atomic number. Since it gives the result in cm^2/g it needs to be multiplied by the density of the scintillator ρ. The characteristics of the crystals is shown in Table 2.1 in chapter 2.1. Lets denote $e^{-\mu \cdot l \cdot \rho}$ as probability of detection the gamma in a given crystal (e.g. $P_{511,\text{LSO}}$). The probabilities estimated in such way are:

$$
\begin{aligned}
P_{511,\text{LSO}} &= 0.58 \\
P_{1275,\text{LSO}} &= 0.32 \\
P_{511,\text{BGO}} &= 1.00 \\
P_{1275,\text{BGO}} &= 0.86
\end{aligned}
$$

The rates of coincidences types are calculated from:

$$
\begin{aligned}
L + L &= 0.9 \cdot A \cdot \Omega_{BGO} \cdot P_{511,\text{LSO}} \cdot P_{511,\text{BGO}} &= 381 \\
L + H &= 0.9 \cdot A \cdot (\Omega_{LSO} - \Omega_{BGO}) \cdot P_{511,\text{LSO}} \cdot \Omega_{BGO} \cdot P_{1275,\text{BGO}} &= 26 \\
LH + L &= 0.9 \cdot A \cdot \Omega_{BGO} \cdot P_{511,\text{LSO}} \cdot P_{511,\text{BGO}} \cdot \Omega_{LSO} \cdot P_{1275,\text{LSO}} &= 9 \\
H + L &= 0.9 \cdot A \cdot \Omega_{BGO} \cdot P_{511,\text{BGO}} \cdot (1 - P_{511,\text{LSO}}) \cdot \Omega_{LSO} \cdot P_{1275,\text{LSO}} &= 7 \\
L + LH &= 0.9 \cdot A \cdot \Omega_{BGO} \cdot P_{511,\text{LSO}} \cdot P_{511,\text{BGO}} \cdot \Omega_{BGO} \cdot P_{1275,\text{BGO}} &= 0.004
\end{aligned}
$$
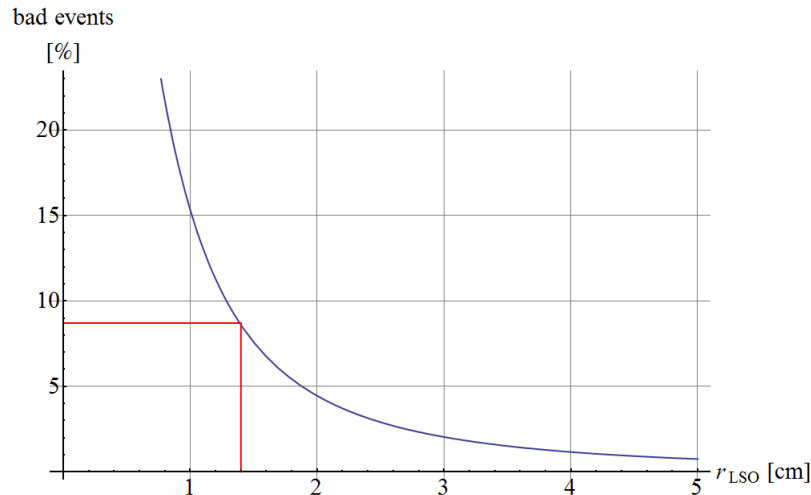
Figure II: *All possible coincidences in the setup.*

The fraction of bad coincidence events for the geometry of our setup is calculated from:

$$\frac{\text{``}L + H\text{''} + \text{``}LH + L\text{''}}{\text{``}L + L\text{''} + \text{``}L + H\text{''} + \text{``}LH + L\text{''}} = 8.6\% \tag{II}$$

This value goes to around 10% if consider events H+L type. The influence of 3rd gamma diminishes with the distance between the source and the LSO. On the other hand, there is another factor that doesn't allow to increase the LSO-source distance to much. It is fraction of coincidence from events scattered from the background (sixth-seventh cases on the Fig. I). They appear when the 511 keV or 1275 keV scatter before reach the BGO detector. It is very difficult to easily calculate their influence, because of numerous parameters. However it can be roughly estimated from the count rate plots. Since the count rate plots edge is outside of the crystal, the offset value is measured. On the Fig. 4.2 it is around 20% of the all events in the center of the crystal. If number of bad coincidences caused by 3rd gamma is around 10%, then the scatters fraction needs to be also around 10%.

Fig. II shows the change of 3rd gamma coincidences with the distance between LSO and the source r_{LSO}. The influence of the scatters from background is not considered on the plot. The r_{LSO} in our setup is around 1.4 cm. It is mainly limited by the size of the beam (see §.3.2.2).

List of Abbreviations

The following abbreviations are used throughout the text:

ANN	Artificial Neural Networks
ADC	Analog to Digital Converter
APD	Avalanche Photodiode
BGO	Bismuth Germanate - $Bi_4Ge_3O_{12}$
CRF	Coincidence Response Function
CT	Computed Tomography
DOI	Depth of Interaction
ENC	Equivalent Noise Charge
ENF	Excess Noise Fraction
FDG	^{18}F-2-fluoro-2-deoxy-D-glucose
FOV	Field of View
FWHM	Full Width at Half Maximum
FWTM	Full Width at Tenth Maximum
GNN	Global Neural Network algorithm
HV	High voltage
LM	Levenberg-Marquardt ANN algorithm
LNN	Local Neural Network algorithm
LOR	Line of Response
LSF	Line Spread Function
LSO	Lutetium Orthosilicate - Lu_2SiO_5
LYSO	$Lu_{1.8}Y_{0.2}SiO_5(Ce)$ or LYSO:Ce$_{3+}$
LY	Light Yield
MLEM	Maximum Likelihood Expectation Maximization
MLP	Multilayer Perceptron Network
MOS	Metal-Oxide-Silicon
MRI	Magnetic Resonance Imaging
NEC	Noise Equivalent Counts
NECR	Noise Equivalent Count Rate
PCB	Printed Circuit Board
PDE	Photon Detection Efficiency
PIN	Silicon *pin* diod
PET	Positron Emission Tomography
PMT	Photomultiplier Tube
PSF	Point Spread Function
QE	Quantum Efficiency

RMS	Root Mean Square
RMSE	Root Mean Square Error
SiPM	Silicon photomultiplier
SNR	Signal-to-Noise Ratio
SPAD	Single Photon Avalanche Diode
SPECT	Single Photon Emission Computed Tomography
TOF	Time of Flight
TDC	Time to Digital Converter
UV	Ultraviolet
VME	VERSA module Eurocard

Institutions and organisations:

CAEN	Costruzioni Apparecchiature Elettroniche Nucleari
CCC	Crystal Clear Collaborration
CIEMAT	Centro de Investigaciones Energéticas Medioambientales y Tecnológicas
FZJ	Forschungszentrum Jülich
IIHE	The Interuniversity Institute for High Energies
NIST	National Institute of Standards and Technology
USTC	The University of Science and Technology of China
UT Delft	University of Technology Delft
VUB	Vrije Universiteit Brussel

List of Symbols

Here the following symbols that are used throughout the text are summarised. Less significant symbols are omitted i.e. these that are used locally, only once in this work. These used in wider context are described.

α	electron ionization rate
α	incidence gamma beam angle
α_i	synaptic weight of the ANN output layer
β	hole ionization rate
β	photon to $e - h$ conversion efficiency
ϵ_{intr}	intrinsic detector spatial resolution
$\varepsilon_{\mathrm{geiger}}$	probability of Geiger initialisation in SiPM
$\varepsilon_{\mathrm{geom}}$	geometric efficiency
$\varepsilon_{\mathrm{intr}}$	intrinsic detector efficiency
η	overall scintillator efficiency
λ	wavelength
μ	linear attenuation coefficient for the photoelectric effect
μ_o	linear material attenuation coefficient
μ_p	the semiconductor absorption coefficient
ν_e	electron neutrino
ρ	scintillator crystal density
σ_{tot}^2	RMSE
σ_{el}^2	electronic noise
ϕ	LOR angle in sinogram
ϕ	transfer or activation function in ANN
Δ_{nonc}	noncolinearity error
ΔE	energy resolution
$\Delta\tau$	coincidence window length
Δt	time resolution
Δx	uncertainty of annihilation point location
Γ	system spatial resolution of a pixelated detector design
Ω	rotation angle of the detector box
a	image reconstruction algorithm factor in Γ
b	parameter of crystal decoding effects in Γ
b_i	the bias of the ith neuron of ANN hidden layer
$\mathbf{b}$	vector of b_i
c	speed of light
e	electron

List of Symbols

e^+	positron
$e - h$	electron - hole pair in pn junction
h	holes carrier in the band structure
$h\nu$	the photon energy
k	ionization coefficient
k_{B}	Boltzmann's constant
l	crystal element length in the detector
l_o	thickness of material travelled by $511\,\mathrm{keV}$ photons
m	rest mass
m_{e^-}	electron rest mass
m_{e^+}	positron rest mass
n	excess of electrons in n-region of p-n junction
n	neutron
p	excess of holes in p-region of p-n junction
p	proton
q_e	electron charge
r_{positr}	effective positron range
s	vector of LOR position in sinogram
t	time-of-flight difference
w	width of the detector element
w_{ij}	synaptic weight in ANN
$\mathbf{v}$	vector of α_i
x	location of the annihilation event between the coincidence detectors
x_j	ANN input
$\mathbf{x}$	vector of x_j
A_o	source emission rate
C	capacitance
D	diameter of the PET scanner detectors ring
D	scanned object diameter
E	energy
E_g	Energy of the gap in the band structure of semiconductors
E_{ph}	photopeak energy
F	excess noise factor
I_{d}	photodiode dark current
I_{db}	photodiode bulk dark current
I_{ds}	photodiode surface dark current
I_{L}	photodiode photocurrent
M	photodiode gain
M	number of neurons in the ANN hidden layer
N	single events rate at the detector
N	number of ANN inputs
N	number of primary $e - h$ created in APD
$\mathcal{N}$	number of event registered by the APD based detector
P_{opt}	the optical power of incident photon in the APD
Q	quantum efficiency of luminous center in scintillator

R	random coincidence events
$R_{scanner}$	coincidence rate registered by the PET scanner
S	scatter coincidence events
S	transfer efficiency of the $e - h$ pair
T	true coincidence events
T	absolute temperature
W	matrix of synaptic weights in ANN
V	voltage
V_{50}	the APD subbarray supplying voltage of that correspond to gain 50
V	voltage
Z_{eff}	Effective atomic number

Bibliography

[APDdata]   Hamamatsu Photonics K.K. *APD S8550 - Final inspection sheets*, 2005-2006.

[Akindinov1997] A.V. Akindinov, A.N. Martemianov, P.A. Polozov, V.M. Golovin, and E.A. Grigoriev. New results on MRS APDs. *Nucl. Instr. and Meth. A*, 387(1-2):231 – 234, 1997.

[Antich1997] P.P. Antich, E.N. Tsyganov, N.A. Malakhov, and Z.Y. Sadygov. Avalanche photo diode with local negative feedback sensitive to UV, blue and green light. *Nucl. Instr. and Meth. A*, 389(3):491 – 498, 1997.

[Arisaka2010] Katsushi Arisaka. Principle of PMT and its Calibration. Technical report, University of California, Los Angeles Department of Physics and Astronomy, 2010.

[Bondarenko2000] G. Bondarenko, P. Buzhan, B. Dolgoshein, V. Golovin, E. Guschin, A. Ilyin, V. Kaplin, A. Karakash, R. Klanner, V. Pokachalov, E. Popova, and K. Smirnov. Limited geiger-mode microcell silicon photodiode: new results. *Nucl. Instr. and Meth. A*, 442(1-3):187 – 192, 2000.

[Britvitch2007] I. Britvitch, I. Johnson, D. Renker, A. Stoykov, and E. Lorenz. Characterisation of geiger-mode avalanche photodiodes for medical imaging applications. *Nucl. Instr. and Meth. A*, 571(1-2):308 – 311, 2007.

[Bruyndonckx2004] P. Bruyndonckx, S. Léonard, S. Tavernier, C. Lemaître, O. Devroede, Yibao Wu, and M. Krieguer. Neural network-based position estimators for PET detectors using monolithic LSO blocks. *IEEE Trans. Nucl. Sci.*, 51(5):2520–2525, 2004.

[Bruyndonckx2006] P. Bruyndonckx, C. Lemaître, D.J. van der Laan, M. Maas, D. Schaart, O. Devroede, M. Krieguer, and S. Tavernier. Comparison of nonlinear position estimators for continuous scintillator detectors in PET. *IEEE NSS Conf. Rec.*, 4:2518–2522, 2006.

[Bruyndonckx2007a] P. Bruyndonckx, C. Lemaître, D. Schaart, M. Maas, D.J. van der Laan, M. Krieguer, O. Devroede, and S. Tavernier. Towards a continuous crystal APD-based PET detector design. *Nucl. Instr. and Meth. A*, 571(1-2):182 – 186, 2007.

[Bryundonckx2003] P. Bryundonckx, S. Leonard, and S. Tavernier. Parallax recovery using neural networks in pet detectors based on continuous scintillators. In *IEEE NSS Conf. Rec.*, volume 3, pages 2174–2178 Vol.3, 2003.

[Buchacher2010] T. Buchacher. Evaluation keramischer Szintillatoren unter Aspekten der PET. Master's thesis, Forschungszentrum Jülich, 2010. in german.

[Buzhan2006] P. Buzhan, B. Dolgoshein, L. Filatov, A. Ilyin, V. Kaplin, A. Karakash, S. Klemin, R. Mirzoyan, A.N. Otte, E. Popova, V. Sosnovtsev, and M. Teshima. Large area silicon photomultipliers: Performance and applications. *Nucl. Instr. and Meth. A*, 567(1):78 – 82, 2006.

[CAENadc] CAEN. *Technical information manual, mod.V785, 32/16 channel peak sensing ADCs, manual rev.12*, 2007. www.caen.it.

[CAENamp] CAEN. *Technical information manual, mod.N568, 16 channel spectroscopy amplifiers, manual rev. 4*, 2007. www.caen.it.

[CAENvme] CAEN. *Technical information manual, mod. V1718, VME bridge, rev. 6*.

[CPhotonics] *Crystal Photonics GmbH.* Berlin, Germany. www.crystal-photonics.com.

[Chen1999] Ruru Chen, A. Fremout, S. Tavernier, P. Bruyndonckx, D. Clément, J. F. Loude, and C. Morel. Readout of scintillator light with avalanche photodiodes for positron emission tomography. *Nucl. Instr. and Meth. A*, 433(3):637 – 645, 1999.

[Cherry2003] S.R. Cherry, J.A. Sorenson, and M.E. Phelps. *Physics in Nuclear Medicine.* Saunders, 3 edition, 2003.

[Clement1998] D. Clement, R. Frei, J.F. Loude, and C. Morel. Development of a 3D position sensitive scintillation detector using neural networks. *IEEE NSS Conf. Rec.*, 3:1448–1452, 1998.

[Conti2009] M. Conti. State of the art and challenges of time-of-flight PET. *Physica Medica*, 25(1):1 – 11, 2009.

[Cremat2006] Cremat. *CR-110 charge sensitive preamplifier: application guide*, 2006. www.cremat.com.

[Defrise2008] M. Defrise and C. De Mol. An overview of some mathematical methods for medical imaging. In *Molecular Imaging: Computer Reconstruction and Practice*, NATO Science for Peace and Security Series B: Physics and Biophysics, pages 93–129. Springer Netherlands, 2008.

[Delorme1996] S. Delorme, R. Frei, C. Joseph, J.F. Loude, and C. Morel. Use of a neural network to exploit light division in a triangular scintillating crystal. *Nucl. Instr. and Meth. A*, 373(1):111–118, 1996.

[Derenzo1979] S. E. Derenzo. Precision measurement of annihilation point distributions for medically important positron emitters. In *Positron annihilation*, pages 819–823, 1979.

[Derenzo2010] S. Derenzo, M. Boswell, M. Weber, and K. Brennan. Scintillation properties. http://scintillator.lbl.gov/, 2010.

[Dolgoshein2006] B. Dolgoshein, V. Balagura, P. Buzhan, M. Danilov, L. Filatov, E. Garutti, M. Groll, A. Ilyin, V. Kantserov, V. Kaplin, A. Karakash, F. Kayumov, S. Klemin, V. Korbel, H. Meyer, R. Mizuk, V. Morgunov, E. Novikov, P. Pakhlov, E. Popova, V. Rusinov, F. Sefkow, E. Tarkovsky, and I. Tikhomirov. Status report on silicon photomultiplier development and its applications. *Nucl. Instr. and Meth. A*, 563(2):368 – 376, 2006.

[DowCorning] Dow Corning Corporation, Midland, MICH, USA. *Dow Corning 200 ® fluid, a dimethylopolysiloxane.* www.dowcorning.com.

[DowCorning1] Dow Corning. *Sylgard ®527 silicone dielectric gel.* http://www.dowcorning.com.

[Evans1955] R.D. Evans. *The atomic nucleus.* Tata McGraw Hill Book Publishing Company Ltd., 1955.

[Fedorov2005] A. Fedorov, M. Korzhik, A. Lobko, O. Missevitch, and A. Annenkov. Light yield temperature dependence of lutetium-based scintillation crystals. *Nucl. Instr. and Meth. A*, 537(1-2):276 – 278, 2005.

[Fluke] *Fluke multimeter.* http://www.fluke.com.

[Fremout2002] A. Fremout. *Design study for a PET scanner based on the use of APD and new scintillators.* PhD thesis, Vrije Universiteit Brussel, 2002.

[Fremout2002a] A.A.R. Fremout, Ruru Chen, P. Bruyndonckx, and S.P.K. Tavernier. Spatial resolution and depth-of-interaction studies with a pet detector module composed of lso and an apd array. *IEEE Trans. Nucl. Sci.*, 49(1):131–138, 2002 2002.

[GE] *PET essentials.* http://gecommunity.gehealthcare.com.

[Gasanov1990] A.G. Gasanov, V.M. Golovin, Z.Y. Sadygov, and N.Y. Yusipov. *Lett. J. Techn. Phys.*, 16:14, 1990. (in Russian).

[Golovin1989] V. Golovin. 1989. Russian Patent No. 1644708.

[Golovin1989a] V. Golovin, A.G. Gasanov, Z.Y. Sadygov, and N.Y. Yusipov. 1989. Russian Patent No. 1702831.

[Guschin2006] E. Guschin, M. Khabibullin, Y. Kudenko, A. Kuznetsov, O. Mineev, Y. Musienko, S. Reucroft, J. Swain, N. Yershov, and M. Vlasov. Multi-pixel geiger-mode avalanche photodiodes with high quantum efficiency and low excess noise factor. *Nucl. Instr. and Meth. A*, 567(1):250 – 254, 2006.

[Hamamatsu2004] Hamamatsu Photonics K.K. *Technical information - Characteristics and use of SiAPD (Avalanche Photodiode)*, 2004. Cat. No. KAPD9001E03, http://www.hamamatsu.com.

[Hamamatsu2006] Hamamatsu Photonics K.K. *Si APD S8550 - device specification*, 2006. Cat. No. KAPD1009E02, http://www.hamamatsu.com.

[Hamamatsu2006a] Hamamatsu Photonics K.K. *Photomultiplier tubes and related products*. 2006. Cat. No. TPMO0005E03, http://www.hamamatsu.com.

[Hamamatsu2007] Hamamatsu Photonics K.K. *Photomultiplier tubes - basis and applications*. 2007. Cat. No. TOTH9001E03a, http://www.hamamatsu.com.

[Hamamatsu2007a] Hamamatsu Photonics K.K. *Hamamatsu multianode photomultiplier tube assembly H7546B*, 2007. Cat. No. TPMH1240E12, http://www.hamamatsu.com.

[Harpen2004] M.D. Harpen. Positronium: Review of symmetry, conserved quantities and decay for the radiological physicist. *Medical Physics*, 31(1):57–61, 2004.

[Haykin1999] S. Haykin. *Neural Networks: A comprehensive foundation*. Pearson Education Inc., 2nd edition, 1999.

[Herbert2007] D.J. Herbert, S. Moehrs, N. D'Ascenzo, N. Belcari, A. Del Guerra, F. Morsani, and V. Saveliev. The silicon photomultiplier for application to high-resolution positron emission tomography. *Nucl. Instr. and Meth. A*, 573(1-2):84 – 87, 2007.

[Hofstadter1948] R. Hofstadter. Alkali halide scintillation counters. *Phys. Rev.*, 74(1):100–101, 1948.

[Huber] P. Huber and D. Huber. *Huber hochgenau temperieren - Inteligent Chiller IC012 - Operating Instructions*. Peter Huber Kältemaschinenbau GMBH.

[Humm2003] J.L. Humm, A. Rosenfeld, and A. Del Guerra. From PET detectors to PET scanners. *Eur. J. Nucl. Med. Mol. Imaging.*, 30(11):1574 –1597, 2003.

[Hutchins2008] G.D. Hutchins, M.A. Miller, V.C. Soon, and T. Receveur. Small animal PET imaging. *ILAR journal / National Research Council, Institute of Laboratory Animal Resources*, 9(1):54–65, 2008.

[Kapusta2003] M. Kapusta, P. Crespo, D. Wolski, M. Moszynski, and W. Enghardt. Hamamatsu S8550 APD arrays for high-resolution scintillator matrices readout. *Nucl. Instr. and Meth. A*, 504(1-3):139 – 142, 2003.

[Karp2008] J.S. Karp, S. Surti, M.E. Daube-Witherspoon, and G. Muehllehner. Benefit of time-of-flight in PET: Experimental and clinical results. *J. Nucl. Med.*, 49(3):462–470, 2008.

[Kataoka2005] J. Kataoka, T. Saito, Y. Kuramoto, T. Ikagawa, Y. Yatsu, J. Kotoku, M. Arimoto, N. Kawai, Y. Ishikawa, and N. Kawabata. Recent progress of avalanche photodiodes in high-resolution X-rays and [gamma]-rays detection. *Nucl. Instr. and Meth. A*, 541(1-2):398 – 404, 2005.

[Kimble2002] T. Kimble, M. Chou, and B.H.T. Chai. Scintillation properties of lyso crystals. In *IEEE NSS Conf. Rec.*, volume 3, pages 1434–1437, 2002.

[Knoll2000] G.F. Knoll. *Radiation Detection and Measurement*. John Wiley & Sons, Inc., 3 edition, 2000.

[Laan2009] D.J. van der Laan. *Modelling monolithic scintillator detectors for positron emission tomography*. PhD thesis, University of Technology Delft, 2009.

[LabView] Ni labview$^\circledR$ 8.6. www.ni.com.

[LeCun1993] Yann Le Cun. *Efficient learning and second-order methods*, 1993. presented at the NIPS 93, Denver, CO.

[Lecomte2007b] R. Lecomte. Medical Imaging: Scintigraphy, SPECT and PET. *TRIUMF Summer Institute 2007, Radiation detectors: Applications in nuclear and particle physics, and medical imaging*, 2007. Vancouver, July 9-20, http://www.triumf.info/hosted/TSI/TSI07/index.html.

[Lemaitre2009] C. Lemaître. *Use of machine learning algorithms for gamma detection in positron emission tomography*. PhD thesis, Vrije Universiteit Brussel, 2009.

[Lempicki1995] A. Lempicki. The physics of inorganic scintillators. *Journal of Applied Spectroscopy*, 62(4):787–802, 1995.

[Lempicki1997] A. Lempicki, A.J. Wojtowicz, and C. Brecher. Inorganic scintillators. In S.R. Rotman, editor, *Wide-gap luminescent materials: theory and applications*, chapter 5. Kluwer Academic Publisher, 1997.

[Leo1992] W.R. Leo. *Techniques for Nuclear and Particle Physics Experiments: A How-to Approach*. Springer New York, 1992.

Bibliography

[Leonard2005] S. Leonard. *Spatial Resolution study of PET detector modules based on LSO crystals and avalanche photodiode arrays*. PhD thesis, Vrije Universiteit Brussel, 2005.

[Lerche2009] Ch.W. Lerche, M. Düring, A. Ros, V. Herrero, R. Gadea, R.J. Aliaga, R. Colom, F. Mateo, J.M. Monzó, N. Ferrando, J.F. Toledo, J.D. Martǐnez, A. Sebastiá, F. Sanchez, and J.M. Benlloch. Depth of interaction detection for γ-ray imaging. *Nucl. Instr. and Meth. A*, 600(3):624 – 634, 2009.

[Levin1999] C.S. Levin and E.J. Hoffman. Calculation of positron range and its effect on the fundamental limit of positron emission tomography system spatial resolution. *Phys. Med. Biol.*, 44(3):781–799, 1999.

[Levin2007] C.S. Levin and H. Zaidi. Current trends in preclinical PET system design. *PET Clinics*, 2(2):125 – 160, 2007.

[Lewellen2008] T.K. Lewellen. Recent developments in PET detector technology. *Phys. Med. Biol.*, 53(17):R287–R317, 2008.

[LiZhi2011] Li Zhi. *Study of 3D interaction position determination in a monolithic scintillator blocks for PET*. PhD thesis, Vrije Universiteit Brussel, 2011. under preparation.

[Lucignani2007] G. Lucignani. Imaging biomarkers: from research to patient care - a shift in view. *Eur. J. Nucl. Med. Mol. Imaging.*, 34(10):1693–1697, 2007.

[Maas2008] M.C. Maas. *Monolithic Scintillator Detectors for High-Resolution Positron Emission Tomography*. PhD thesis, University of Technology Delft, 2008.

[Maas2008a] M.C. Maas, D.R. Schaart, D.J. van der Laan, H.T. van Dam, J. Huizenga, J.C. Brouwer, P. Bruyndonckx, C. Lemaitre, and C.W.E. van Eijk. Signal to Noise Ratio of APD-Based Monolithic Scintillator Detectors for High Resolution PET. *IEEE Trans. Nucl. Sci.*, 55(3):842 –852, 2008.

[Maas2009] M.C. Maas, D.R. Schaart, D.J. van der Laan, P. Bruyndonckx, C. Lemaitre, F.J Beekman, and C.W.E. van Eijk. Monolithic scintillator pet detectors with intrinsic depth-of-interaction correction. *Phys. Med. Biol.*, 54(7):1893–1908, 2009.

[McElroy2007] D.P. McElroy, V. Saveliev, A. Reznik, and J.A. Rowlands. Evaluation of silicon photomultipliers: A promising new detector for mr compatible pet. *Nucl. Instr. and Meth. A*, 571(1-2):106 – 109, 2007.

[McIntyre1972] R.J. McIntyre. The distribution of gains in uniformly multiplying avalanche photodiodes: Theory. *IEEE Trans. El. Dev.*, 19(6):703–713, 1972.

[McIntyre1996] R.J. McIntyre, P.P. Webb, and H. Dautet. A short-wavelength selective reach-through avalanche photodiode. *IEEE Trans. Nucl. Sci.*, 43(3):1341–1346, 1996.

[Melcher1990] C.L. Melcher. Lutetium orthosilicate single crystal scintillator detector. 1990. USA Patent No. 4958080.

[Melcher2000] C.L. Melcher. Scintillation crystals for PET. *J. Nucl. Med.*, 41(6):1051–1055, 2000.

[Meltmount] Cargille Laboratories, Inc., Cedar Grove, NJ, USA. *Cargille Meltmount*$^{\text{TM}}$ *1.582*. Code 5870, Cat.24150. www.cargille.com.

[Mendes2007] P.R. Mendes, P. Bruyndonckx, J. Navarrete, J.M. Perez, and Zhi Li. Evaluation of monolithic detector blocks for high- sensitivity PET imaging of the human brain. In *IEEE NSS Conf. Rec.*, number 4, 2007.

[Mendes2009] Pedro Rato Mendes. Continuous scintillator detector blocks for simultaneous PET-MR imaging of the human brain. In Como 5-9 October Villa Olmo, editor, 11th *International Conference on Advanced Technology and Particle Physics*, 2009.

[Moses1993] W.W. Moses and S.E. Derenzo. Empirical observation of resolution degradation in positron emission tomographs utilizing block detectors. *J. Nucl. Med.*, 34:101P, 1993.

[Moses1997] W.W. Moses, P.R.G. Virador, S.E. Derenzo, R.H. Huesman, and T.F. Budinger. Design of a high-resolution, high-sensitivity PET camera for human brains and small animals. *IEEE Trans. Nucl. Sci.*, 44(4):1487–1491, 1997.

[Moses2003] W.W. Moses. Time of flight in PET revisited. *IEEE Trans. Nucl. Sci.*, 50(5):1325–1330, 2003.

[Moses2007] W.W. Moses. Recent advances and future advances in time-of-flight PET. *Nucl. Instr. and Meth. A*, 580(2):919 – 924, 2007.

[Muehllehner2006] G. Muehllehner and J.S. Karp. Positron emission tomography. *Phys. Med. Biol.*, 51(13):R117–R137, 2006.

[Musienko2007] Y. Musienko, E. Auffray, P. Lecoq, S. Reucroft, J. Swain, and J. Trummer. Study of multi-pixel Geiger-mode avalanche photodiodes as a read-out for PET. *Nucl. Instr. and Meth. A*, 571(1-2):362 – 365, 2007.

[NIST] *Database of Physical Measurements Laboratory - National Institute of Standards and Technology*. http://physics.nist.gov/PhysRefData/Xcom/html/xcom1.html.

[Photonis] Photonis. *Photomultiplier XP2020 - characteristics*, 2007. http://www.photonis.com/.

[Pichler2001] B.J. Pichler, F. Bernecker, G. Boning, M. Rafecas, W. Pimpl, M. Schwaiger, E. Lorenz, and S.I. Ziegler. A 4×8 APD array, consisting of two monolithic silicon wafers, coupled to a 32-channel LSO matrix for high-resolution PET. *IEEE Trans. Nucl. Sci.*, 48(4):1391–1396, 2001.

[Platform] Micro Contrôle, 5 rue Paul Bert 94400 Vitry sur Seine (France). *Utilisation Fonctionnement - IT6DCA2*.

[Qi2006] Jinyi Qi and R.M. Leahy. Iterative reconstruction techniques in emission computed tomography. *Physics in Medicine and Biology*, 51(15):R541–R578, 2006.

[Reader2007] A.J. Reader and H. Zaidi. Advances in PET Image Reconstruction. *PET Clinics*, 2(2):173 – 190, 2007.

[Renker2002] D. Renker. Properties of avalanche photodiodes for applications in high energy physics, astrophysics and medical imaging. *Nucl. Instr. and Meth. A*, 486(1-2):164 – 169, 2002.

[Renker2007] D. Renker. New trends on photodetectors. *Nucl. Instr. and Meth. A*, 571(1-2):1 – 6, 2007.

[Rey2007] Martin Rey. *Étude du tomographe de haute résolution pour petits animaux ClearPET par la méthode de Monte Carlo*. PhD thesis, EPFL Lausanne, 2007.

[Sadygov2006] Z. Sadygov, A. Olshevski, I. Chirikov, I. Zheleznykh, and A. Novikov. Three advanced designs of micro-pixel avalanche photodiodes: Their present status, maximum possibilities and limitations. *Nucl. Instr. and Meth. A*, 567(1):70 – 73, 2006.

[Saveliev2000] V. Saveliev and V. Golovin. Silicon avalanche photodiodes on the base of metal-resistor-semiconductor (MRS) structures. *Nucl. Instr. and Meth. A*, 442(1-3):223 – 229, 2000.

[Schaart2009] D.R. Schaart, H.T. van Dam, S. Seifert, R. Vinke, P. Dendooven, H. Lohner, and F.J. Beekman. A novel, SiPM-array-based, monolithic scintillator detector for PET. *Phys. Med. Biol.*, 54:3501–3512, 2009.

[Schaart2010] D.R. Schaart, S. Seifert, R. Vinke, H.T. van Dam, P. Dendooven, H. Lãűhner, and F.J. Beekman. Labr 3 :ce and sipms for time-of-flight pet: achieving 100 ps coincidence resolving time. *Phys. Med. Biol.*, 55(7):N179–N189, 2010.

[Seifert2008] S. Seifert, D.R. Schaart, H.T. van Dam, J. Huizenga, R. Vinke, P. Dendooven, H. Lohner, and F.J. Beekman. A high bandwidth preamplifier for SiPM-based TOF PET scintillation detectors. In *IEEE NSS Conf. Rec.*, pages 1616 –1619, 2008.

[SensL] *SensL SiPM Array 3035G16*. www.sensl.com.

[Spectralon]   http://en.wikipedia.org/wiki/Spectralon.

[Strother1990] S.C. Strother, M.E. Casey, and E.J. Hoffman. Measuring pet scanner sensitivity: relating countrates to image signal-to-noise ratios using noise equivalents counts. *IEEE Trans. Nucl. Sci.*, 37(2):783–788, 1990.

[Swain2005]   J. Swain, S. Reucroft, and Y. Musienko. Recent developments in pixellated avalanche photodiodes. In *IEEE NSS Conf. Rec.*, volume 5, pages 2944 –2948, 2005.

[Tavernier2005] S. Tavernier, P. Bruyndonckx, S. Leonard, and O. Devroede. A high-resolution PET detector based on continuous scintillators. *Nucl. Instr. and Meth. A*, 537(1-2):321 – 325, 2005.

[Tavernier2010] S. Tavernier. *Experimental Techniques in Nuclear and Particle Physics.* Springer, 2010.

[Teflon]   E.I. du Pont de Nemours & Co., Inc. *Teflon*® *sealing tape.* www.sigma-aldrich.com.

[Weber1973]   M. J. Weber and R. R. Monchamp. Luminescence of $Bi_4Ge_3O_{12}$: Spectral and decay properties. *J. Appl. Phys.*, 44(12), 1973.

[Weber2003]   S. Weber, D. Christ, M. Kurzeja, R. Engels, G. Kemmerling, and H. Halling. Comparison of LuYAP, LSO, and BGO as Scintillators for High Resolution PET Detectors. *IEEE Trans. Nucl. Sci.*, 50(5):1370–1372, 2003.

[Wester2007]   H.J. Wester. Nuclear imaging probes: from bench to bedside. *Clinical Cancer Research*, 13(12):3470–3481, 2007.

[Wolfram]   www.wolfram.com.

[Wolfram2005]   WolframResearch. *Mathematica-Neural Networks: Train and analyze neural networks to fit your data.* 2005. www.wolfram.com.

[Xie2006]   Qingguo Xie, Chien-Min Kao, K. Byrum, G. Drake, A. Vaniachine, R.G. Wagner, V. Rykalin, and Chin-Tu Chen. Characterization of silicon photomultipliers for pet imaging. In *IEEE NSS Conf. Rec.*, volume 2, pages 1199–1203, 2006.

[Yonggang2010] Wang Yonggang, Du Junwei, Zhou Zhonghui, Yang Yang, Zhang Lijun, and P. Bruyndonckx. FPGA Based Electronics for PET Detector Modules with Neural Network Position Estimators. *To be published.*

[Ziemons2009]   K. Ziemons. A monolithic block detector design for a hybrid MR-PET scanner. *AstroMed09, Sydney*, 2009.

[vanEijk2002]   C.W.E van Eijk. Inorganic scintillators in medical imaging. *Phys. Med. Biol.*, 47(8):R85–R106, 2002.

Acknowledgements

I would like to thank everybody who supported me in research and who helped me to overcome every day problems in a new country such as Belgium was for me several years ago.

First of all I want to thank Stefaan Tavernier for the opportunity to study abroad in such good scientific environment as IIHE. Many thanks for Peter Bruyndonckx for his patience and detailed explanations of any problem I've found during my studies. Without Marleen Goeman I wouldn't be able to find myself in all of these new rules at the university or general in Belgium. Her support is really difficult to quantify, so thank You. I must to mention my first office-mate Olivier Devroede, who introduced me PET details and many linux tricks. That were very interesting discussions. In my everyday laboratory work very helpful were Jan De Bruyne, Christian Wastiels and Léon Etienne, thank You. I want to thank all of colleagues from IIHE but essentially: Jun Dang, Li Zhi and Cedric Lemaître from PET group, the badminton master Alfio Rizzo from Ice Cube, four very top quarks Ilaria Villella, Petra Van Mulders, Joris Maes and Grégory Hammad, Danny Vijverman from computing support. With You I've never bored. I want to thank scientific groups from UT Delft and UTSC for data sets, from FZJ and CIEMAT for the electronic components.

Finally I thank Marzena for supporting and figures preparation, and Emil that he inherit calmness from his mother. Dziękuje bardzo moim dwóm robalkom. I would like to thank my Brussels friends Fabien, Munesh, Mateusz, Wioleta and Wojtek.

Thank You again!